Aus dem Max-Planck-Institut für Kolloid- und Grenzflächenforschung

Design and Characterization of Multicompartment Micelles in Aqueous Solution

Dissertation

Zur Erlangung des akademischen Grades
Doktor der Naturwissenschaften
(Dr. rer. nat.)
in der Wissenschaftsdisziplin
Physik kondensierter Materie

eingereicht an der Mathematisch-Naturwissenschaftlichen Fakultät
der Universität Potsdam

von
Stephan Kubowicz
aus Berlin

Potsdam, im April 2005

Die vorliegende Arbeit entstand in der Zeit von Mai 2002 bis April 2005 in einem Kooperationsprojekt zwischen dem Max-Planck-Institut für Kolloid- und Grenzflächenforschung, Potsdam, und dem Fraunhofer-Institut für Angewandte Polymerforschung, Potsdam.

Die Neigung der Menschen,
kleine Dinge für wichtig
zu erachten, hat schon
vieles Großes erbracht.

G. Ch. Lichtenberg (1742-1799)

Contents

Chapter 1

Introduction

Self-assembly of polymeric building blocks is a powerful tool for the design of novel materials and structures that combine different properties and may respond to external stimuli. In the past decades, most studies were focused on the self-assembly of amphiphilic diblock copolymers in solution. The dissolution of these block copolymers in a solvent selective for one block results mostly in the formation of micelles. The micellar structure of diblock copolymers is inherently limited to a homogeneous core surrounded by a corona, which keeps the micelle in solution. Thus, for drug-delivery applications, such structures only offer a single domain (the hydrophobic inner core) for drug entrapment. In Nature, some biological systems such as human serum albumin (HSA) are able to selectively uptake and release different substances at the same time.[1, 2] The concept of a "multicompartment micelle" is inspired by this singular behavior of HSA. Thus, multicompartment micelles composed of a water-soluble shell and a segregated hydrophobic core are novel, interesting morphologies for applications in a variety of fields including medicine, pharmacy and biotechnology. For example, in drug delivery applications, the separated incompatible compartments of the hydrophobic core could enable the selective entrapment and release of various hydrophobic drugs while the hydrophilic shell would permit the stabilization of these nanostructures in physiological media. Therefore, the concept of multicompartment systems is an intriguing example for the use of bottom-up strategies in nanotechnology. However, so far, the preparation and control of stable multicompartment micellar systems are in the first stages and the number of morphological studies concerning such micelles is rather low. Thus considerably little is known about their exact inner structures.

In the present work, we concentrate on four different approaches for the preparation of multicompartment micelles by self-assembly in aqueous media. A similarity of all approaches is, that hydrocarbon and fluorocarbon blocks were selected for all employed copolymers since such segments tend to be strongly incompatible, and thus favor the segregation into distinct domains. The investigation is divided into four parts: (*i*) A new type of linear ABC triblock copolymer poly(4-vinylbenzyl *N*-methylmorpholinium chloride)-*b*-polystyrene-*b*-poly(4-vinylbenzyl pentafluorophenol ether) (PVBM-b-PS-b-PVBFP) will be studied. One aspect will be the influence of the preparation technique on the micellar structure. (*ii*) The synthesis and characterization of a novel ABCBA pentablock copolymer is described. The copolymer is composed of poly(ethylene oxide) as hydrophilic A blocks and two hydrophobic poly(γ-benzyl-L-glutamate) blocks (B) as well as a fluorinated ether as fluorocarbon C block. The poly(ethylene oxide) was chosen as the water soluble block since it is known to be biocompatible, which makes it attractive for potential applications in the medical field. Additionally, the peptide block bears a stimuli responsive character, which can be interesting for future investigations, which are beyond the scope of this work. (*iii*) A polymeric surfactant consisting of a telechelic poly(2-methyl-2-oxazoline) end-capped with a hydrophobic fluorocarbon and a hydrocarbon block is described. The investigations focus on the influence of the block length of the water soluble poly(2-methyl-2-oxazoline) block on the micellar structure. Moreover with the idea of using these polymeric aggregates as a transport vehicle in mind we will study their ability to solubilize a fluorophilic low molecular weight substance as a model compound for fluorinated drugs. (*iv*) The preparation and investigation of a polymer-surfactant complex was undertaken. The idea is to use ionic interactions instead of covalent bonds as an alternative way for the preparation of multicompartment aggregates. This technique could be very versatile and bears the possibility of tuning a multicompartment system by combining the features of different surfactants. Towards this goal, an ABA triblock poly(ethylene oxide)-*b*-poly(diallyl dimethyl ammonium chloride)-*b*-poly(ethylene oxide) (PEO-*b*-PDADMAC-*b*-PEO) copolymer with a cationic middle block will be complexed with low molecular weight carboxylic and perfluorocarboxylic acids of different chain length. Due to the two water-soluble PEO blocks, the aggregates should be stabilized even at (1:1) stoichiometry.

Chapter 2

Fundamentals

2.1 Block copolymers

Block copolymers are macromolecules consisting of two or more different blocks of varying monomers linked together by a covalent bond. Thus, block copolymers allow the physicochemical properties of different polymers to be combined in a single molecule. Depending on the nature of the monomers, the number and lengths of the block segments, as well as the chain architecture (linear, branched, graft, star etc.), block copolymers may exhibit a wide range of interesting properties. Industrially, they are widely used in the solid state as well as in solution for applications such as thermoplastic elastomers, foams, oil additives, colloidal stabilization, medical implantation and microelectronic fabrication. Recent advances in synthetic chemistry have exposed fresh opportunities for using judicious combinations of multiple blocks in novel molecular architectures to produce a seemingly unlimited number of exquisitely structured materials endowed with tailored mechanical, optical, electrical, ionic, barrier and other physical properties.[3]

During the last decade, considerable progress in the development of "living" and controlled polymerization techniques have been made and new monomers have become accessible, which may give rise to new classes of functional polymers. These polymerizations can be of the controlled radical type like atom transfer radical polymerization (ATRP), nitroxide mediated polymerization (NMP) or reversible addition-fragmentation chain-transfer polymerization (RAFT), as well as living controlled anionic or cationic polymerization. Living polymerization techniques have made it possible to prepare polymers with exact predetermined degrees of polymerization and low polydispersities. The degree of polymerization, N, of the polymer depends on the molar ratio of initiator to monomer in

the reaction medium. The polydispersities are mostly in the range $M_w/M_n < 1.1$.[4] The synthesis of block copolymers can be done either by sequential polymerization of different monomers or by connecting two homopolymer blocks covalently by a suitable coupling reaction. In the first way, α or α, ω active sites are generated on a polymer chain, *polymer A*, which then initiate the polymerization of a second *monomer B* (macroinitiators). The second method, which is usually called condensation or coupling, is a reaction between chemical functional groups present at the end terminus of different polymers. A more detailed overview on polymerization techniques can be found in the literature.[5, 6, 7, 8, 9, 10]

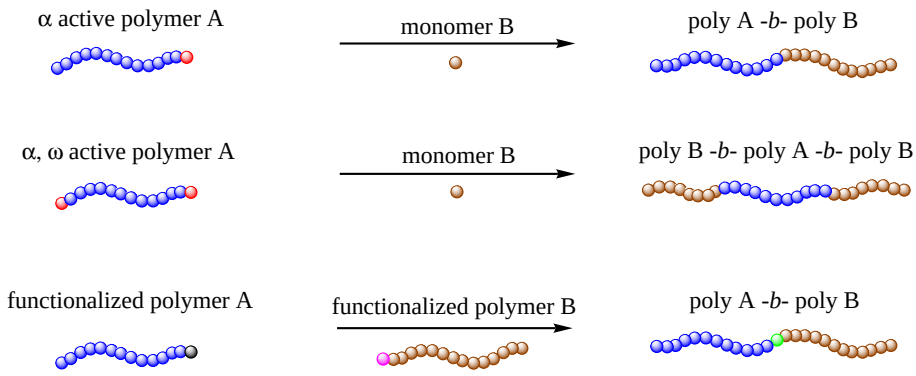

Figure 2.1: General reaction scheme for synthesis of linear block copolymers.

The growing interest in block copolymers arises mainly from their unique solution and associative properties. The mixing of two different types of polymer chains usually results in macroscopic phase separation. Even minor chemical or structural differences between the two polymers are sufficient for this phase separation, which can be explained in terms of the reduced combined mixing entropy. In block copolymers the two or more incompatible polymer chains are connected covalently with each other, which leads to a microphase separation where each block resides in its own phase. Such a formation of ordered domains is a consequence of short range attractive (e.g. covalent bonding, electrostatic interactions, or dipole-dipole interactions) and long range repulsive forces (e.g. Coulombic repulsion, hydrophilic/hydrophobic incompatibility, or excluded volume) existing at the same time. These microdomains usually have sizes of 5-100 nm, depending on the chain length. Their self-associative characteristics are directly related to their molecular structure and segmental incompatibility, as well as concentration, temperature and interfacial energy. Hence, a wide variety of structures and morphologies either in bulk phase or in solution can be obtained. Figure (2.2) shows an overview of the most common

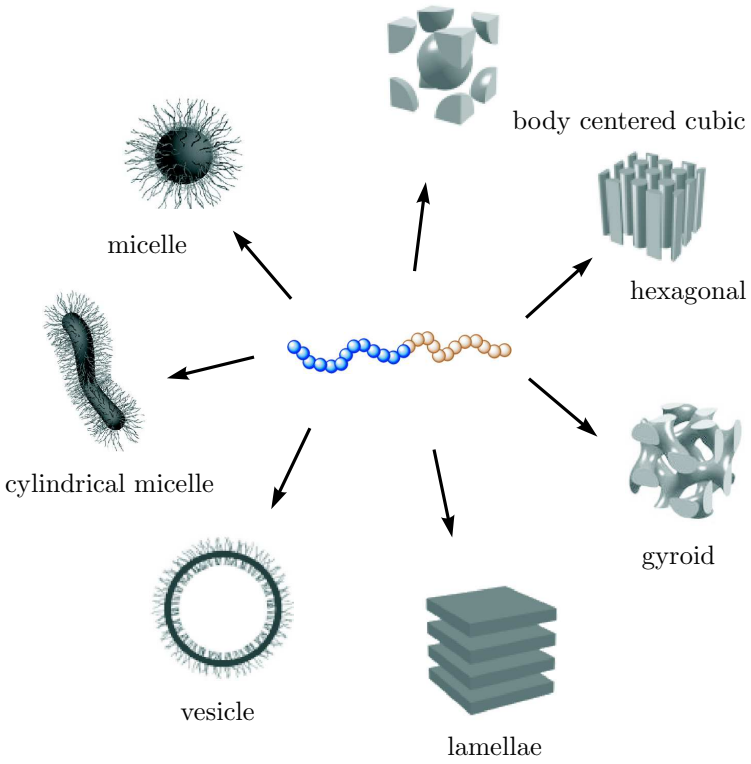

Figure 2.2: Schematic representation of the most common self-organization structures in bulk phase and in solution.[4]

structures formed by diblock copolymers.

Microphase separation of the copolymer blocks is generally driven by the enthalpy of demixing, which is proportional to the Flory-Huggins interaction parameter, χ. A positive χ value indicates a repulsion between the two species A and B, whereas a negative value indicates a tendency towards mixing.[3] The Flory-Huggins interaction parameter itself is inversely proportional to the temperature and can be parameterized as

$$\chi \approx \frac{a}{T} + b \tag{2.1}$$

where $a(> 0)$ and b are constants, different for each polymeric system.[11]

The block copolymer phase behavior in bulk can be described by the product χN, which expresses the balance between enthalpic and entropic contributions to the free energy and also indicates the degree of incompatibility. $N = N_A + N_B$ is the degree of polymerization. Matsen, Schick and Bates calculated a phase diagram for AB diblock copolymers with the volume fraction of one component, $f_A = N_A/N$, as independent composition variable.[12, 13, 14] For a symmetric diblock copolymer ($f_A = 0.5$) the order-

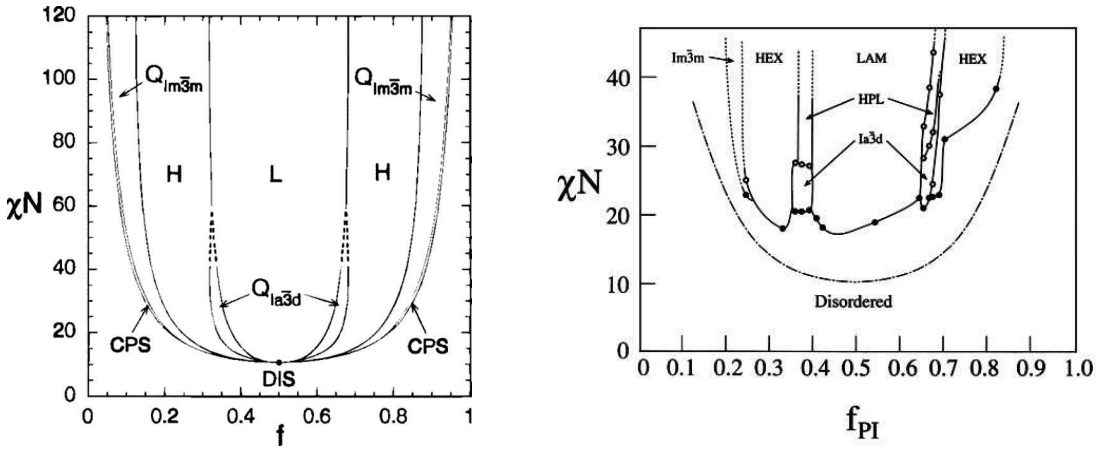

Figure 2.3: Left: Theoretical phase diagram of diblock copolymers. Five ordered microphase structures are predicted (close-packed spheres (CPS), body centered cubic packed spheres ($Q_{lm\bar{3}m}$), hexagonally ordered cylinders (H), gyroid ($Q_{la\bar{3}d}$) and lamellae (L)).[14] Right: Experimentally observed phase diagram for PS-*b*-PI diblock copolymers in the weak segregation limit.[15]

disorder transition (ODT) is predicted as $\chi N = 10.5$; i.e. for smaller values ($\chi N < 10.5$) there will be no microphase separation, whereas for $\chi N > 10.5$ the system will separate into a lamellar phase. At larger values of χN, above the ODT curve, depending on the volume fraction, f_A, five ordered microphase structures are predicted (close-packed spheres (CPS), body centered cubic packed spheres (BCC), hexagonally ordered cylinders, gyroid and lamellae).[3] Depending on the degree of incompatibility, χN, several regimes have been identified: the weak segregation limit (WSL) corresponds to χN close to the ODT curve. The intermediate segregation regime ranges up to about $\chi N \approx$100, and the strong segregation limit (SSL) extends to higher incompatibilities.[11] Furthermore, a new regime called super strong segregation limit (SSSL) has been reported.[16] Khandpur and coworkers determined a phase diagram experimentally for a series of polystyrene-*b*-polyisoprene (PS-*b*-PI) diblock copolymers near the order-disorder transition, which confirm the theoretical predictions mentioned above.[15]

2.2 Self-assembly of block copolymers in solution

The first who tried to interpret the phenomenon of solution self-assembly of copolymers was Merrett[17]. He proposed that the addition of a selective precipitant to a solution of polyisoprene-*graft*-poly(methyl methacrylate) leads to a microseparation of the insoluble

and soluble segments. His hypothesis of compact micelles was supported by low values of intrinsic viscosity, $[\eta]$. Numerous authors[18, 19, 20] also reported a noticeable decrease in intrinsic viscosity together with an increase in the Huggins coefficient, k_H (ref. Sect. 3.5) for various polymer systems when passing from a good to a selective solvent. Thus, dissolution of block copolymers in a selective solvent, which is a thermodynamically good solvent for one block and a nonsolvent for the other, leads to a reversible closed association in form of micellar or vesicular aggregates. Below a certain concentration termed the critical micelle concentration or association concentration (cmc and cac respectively), the copolymer is dissolved molecularly as unimers. Above the cmc, the unimers associate to polymolecular aggregates, which are in dynamic equilibrium with the molecularly dissolved unimers. The main conclusions from the experiments are that block and graft copolymers in selective solvents generally form spherical micelles with a core shell structure and, the higher the molar mass of the micelles, the more compact the formed structure. However, the viscosity of the solution is not the only parameter that changes during micellization; other physical properties also may change such as surface tension, γ, osmotic pressure, Π, or turbidity, τ. Such parameters can, therefore, also be used to determine the cmc. This behavior is very similar to classical low molecular weight soaps and surfactants.

The size and shape (spherical, cylindrical etc.) of the micelles depend mainly on the length of each block (N_A, N_B), the overall degree of polymerization ($N = N_A + N_B$) as well as on the Flory-Huggins parameter, χ, of the interaction between both polymer blocks (χ_{AB}) and between the polymer blocks and solvent (χ_{AS}, χ_{BS}). Various models and mathematical approaches have been developed to derive relations between these parameters and basic characteristics of the micelles (cmc, aggregation number, Z, core radius, R_c, and shell radius, R_s) and they can be divided into two principle treatments. The first approach is to derive explicit terms for the total Gibbs energy of the micelle and then minimize the energy with respect to the polymer parameters.[21, 22, 23, 24] This leads to numerical values for the micellar parameters. The second method is to derive so-called scaling laws from experimental data to predict how a given micellar parameter (e.g. core radius) will change with respect to a given copolymer parameter (e.g. block length).[25, 26, 27]

Assuming that a micellar solution is formed by a diblock copolymer (A-*block*-B) in a selective solvent for block A, where N_A and N_B denote the number of monomer units in block A and B respectively, the structure of the micelles depends crucially on the relative

block length. The two extreme cases are the large core limit ($N_A \ll N_B$) where the radius of the micelle, R, is practically equal to the core radius, R_c, and the micellar parameters depend only on N_B. The scaling relations[27] for this case are $R \sim N_B^{2/3}$ and $Z \sim N_B$. These micelles are so-called "crew cut micelles". The second case is the small core limit ($N_A \gg N_B$) where each A block can occupy a large area of the core-shell interface, which decreases the influence of N_A on the micellar parameters. The scaling relations[27] for these so-called "hairy micelles" are $R \sim N_B^{3/5}$ and $Z \sim N_B^{4/5}$. Between these two boundary

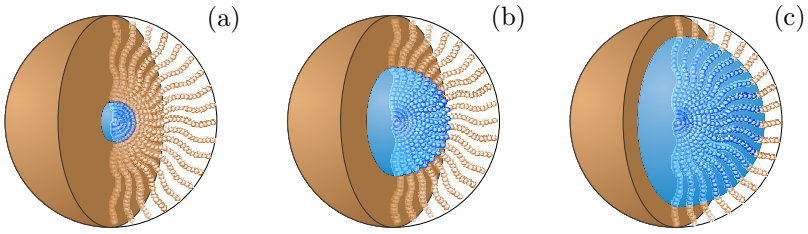

Figure 2.4: Schematic representation of: (a) hairy micelle, (b) intermediate stage micelle, (c) crew cut micelle.

cases the micellization is also significantly affected by the soluble block A. In some cases, the block lengths and the interaction with the solvent can have an influence on the shape of the micelles, which leads to elliptical, cylindrical or worm-like micelles.[28, 29]

A special group of block copolymers are those containing a block with a significant number of ionic moieties. Interesting in ionic block copolymers (block ionomers or block polyelectrolytes) is the extreme incompatibility between the ionic and hydrophobic block, which results in a much stronger driving force for microphase separation. This results in ionic block copolymers having a very low critical micelle concentration (cmc) compared to nonionic block copolymers. Also, the aggregates show a high time and temperature stability. Due to this strong segregation, ionic block copolymers can form a wide range of aggregate sizes and shapes simply by varying the relative lengths of the ionic and nonionic blocks within a single block copolymer system.[30]

2.2.1 Solubilization in micelles

One of the most interesting properties of micellar aggregates in aqueous media is the ability to solubilize hydrophobic substances in their core. This phenomenon of enhanced solubility has been studied mostly in solutions of soaps and surfactants.[31, 32] In fact there

are only a few studies of the solubilization tendency of block copolymer micelles. Experimental results show that block copolymer micelles bear a larger capacity and selectivity in solubilization compared to low molecular weight surfactants. Nagarajan et al.[33] studied the solubilization of aliphatic and aromatic hydrocarbons in a system of poly(ethylene oxide)-*b*-poly(propylene oxide) (PEO-*b*-PPO) and poly(*N*-vinylpyrrolidone)-*b*-polystyrene (PVP-*b*-PS) as micelle forming copolymers. The results reveal an unusual selectivity in the solubilization in, which aromatic molecules were preferred compared to aliphatic hydrocarbons. A theoretical approach[34] based on the thermodynamic of micellization confirms that the Flory-Huggins parameter, χ, which characterizes the interaction between the solubilized compound and the core-forming polymer block, is mainly responsible for the solubilization ability. Other authors[35, 36, 37] investigated the solubilization of an insoluble homopolymer into block or graft copolymer micelles, which is sometimes an undesirable effect while precipitation fractionation of copolymers. The results confirm that a homopolymer can only be solubilized when its molar mass is lower, than that of the core-forming block of the copolymer. When the molar mass exceeds a critical amount, macrophase separation results.

Thus, block copolymer micellar systems hold great potential for the development of applications as chemical extractants in separation processes, as industrial cleaning agents or as tissue-specific drug delivery systems. For the latter application, block copolymers containing poly(ethylene oxide) (PEO) as the water-soluble block have been studied rather extensively, as they are commercially available and their biocompatibility makes them very attractive for biomedical applications.[38]

2.2.2 ABC triblock copolymer micelles

Triblock copolymers with a linear or branched ABC structure offer an increased potential of tailored properties and show a large variety of microphase structures in the solid state.[39, 40] These arise mainly from the three different interaction parameters χ_{AB}, χ_{AC} and χ_{BC} compared to only one (χ_{AB}) in diblock copolymers and two independent composition variables f_A and f_B. Additionally the block sequence (ABC, BCA or CAB) has an important influence on the morphological structure. As Patrickios *et al.*[41] showed, the size of the micelles of a symmetric ABC triblock copolymer depends strongly on the block sequence. Thus, the main difference is whether the soluble block is in the middle or at one end of the copolymer chain.

However, the colloidal properties of triblock copolymers in selective solvents have not yet been studied in detail. An example for micelles of a linear ABC triblock copolymer of polystyrene-*b*-poly(2-vinyl pyridine)-*b*-poly(ethylene oxide) (PS-*b*-P2VP-*b*-PEO) in water has been reported by Jérôme and co-workers.[42] These spherical micelles with a so-called "onion type" core-shell-corona morphology are pH responsive due to the P2VP block and the authors were able to selectively load the shell with $AuCl_4^-$ ions. A potential application of triblock copolymer micelles is the controlled release of solubilized compounds. In this case, a layered micellar morphology (onion type) would be desirable where a core with a high solubilization capacity is surrounded by a shell, which acts as a barrier for the diffusion of the solubilized compound from the core to the outside. Kříž *et al.*[43] prepared a poly(2-ethylhexyl acrylate)-*b*-poly(methyl methacrylate)-*b*-poly(acrylic acid) (PEHA-*b*-PMMA-*b*-PAAc) triblock system and investigated its micellization behavior in water. The authors observed the formation of spherical micelles with the PEHA blocks in the inner core surrounded by a layer of PMMA blocks. The solubilization of cyclohexane was slower than that of PMMA-*b*-PAAc diblock micelles but the uptake capacity was markedly larger. This demonstrates the possibility of tailoring a desired combination of solubilization capacity and uptake/release rate for a specific solubilizate.

Multicompartment micelles possessing coexisting segregated inner-regions could be capable of trapping several drugs of different types and delivering them simultaneously within the human body. Such structures can be prepared via the self-assembly of predesigned amphiphilic polymer architectures in aqueous media. The polymer architectures can be either linear ABC triblock copolymers or branched terpolymers. Thereby, it is important to specify the definition of multicompartment micelles by emphasizing the expected properties of the hydrophobic multicompartment core, in particular the feature that the various sub-domains of the micellar core must be substantially different so as to behave as separated compartments. In fact, for applications such as selective entrapment of incompatible compounds within the compartments, it is expected that there is no exchange between the various sub-domains composing the core. Thus, an observed phase separation in a hydrophobic core is not sufficient for ranking a micellar assembly as a multicompartment system. For example, two thermodynamically incompatible polymers such as polystyrene and polybutadiene can potentially phase segregate into various domains in a micellar core, but most likely they will not permit a selective confinement of low molecular weight hydrophobic molecules. Such a selective confinement requires sub-domains in the core of

the micelle, which are substantially different from each other. Notably systems composed of both hydrocarbon and fluorocarbon hydrophobic domains are very good candidates for fulfilling this requirement since hydrocarbon and fluorocarbon are strongly incompatible and exhibit clearly different properties. Thus, to date, in all the reported studies on multicompartment micelles, the hydrocarbon-fluorocarbon strategy was adopted although other systems might be usable.[44] Several approaches to form multicompartment

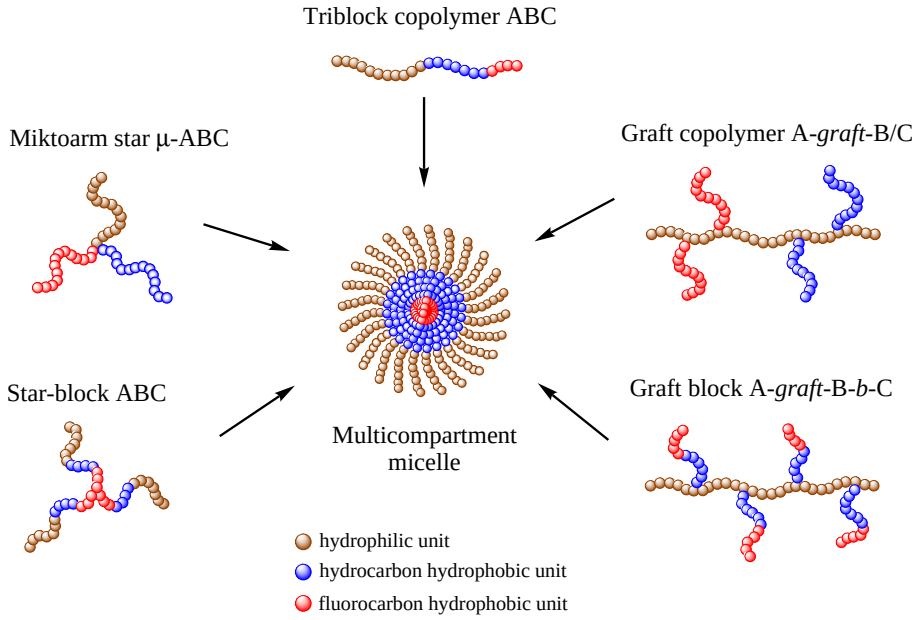

Figure 2.5: Strategies for building multicompartment micelles via self-assembly of various segmented amphiphilic copolymers in aqueous media.[44]

micelles on the basis of ABC triblock copolymer macrosurfactants and polysoaps bearing fluorocarbon chains have been reviewed recently.[45] The article illustrates that the preparation and characterization of multicompartment micelles are rather problematic tasks. Most recently, Lodge and co-workers [46] described the preparation of multicompartment micelles in aqueous medium via self-assembly of ABC miktoarm star block terpolymers of poly(ethylene oxide), poly(ethyl ethylene), and poly(perfluoropropylene). The authors succeeded to visually prove the formation of segregated compartments in a micellar core by means of cryo-transmission electron microscopy (cryo-TEM). The obtained micellar morphologies depend on the relative block lengths and can be altered from discrete multicompartment micelles to extended worm-like structures with segmented cores.

2.3 Preparation of micellar solutions

There are two main procedures for the preparation of a micellar solution from block copolymers. The first is, to dissolve the block copolymer in a common solvent in which all blocks are soluble and then to alter conditions such as temperature or composition of the solvent so that only one block stays soluble and the micellization starts. Often the dialysis technique is recommended for changing the composition of the solvent gradually from the common solvent to the selective solvent. The second method of preparation is to dissolve a solid sample of the block copolymer directly in a selective solvent and then to anneal it by leaving to stand or by thermal treatment. However, as mentioned by Munk[47], this technique is not recommended as the micellar structure will depend on the morphology of the bulk sample as well as on the interactive properties of the selective solvent. To reach an equilibrium it would be necessary for the selective solvent to swell the insoluble block extensively since if the solvent does not swell the insoluble block, the sample will not dissolve at all.

From literature[47] it appears that with both techniques it is not necessary that the micellar system reaches a thermodynamic equilibrium, especially when the non-soluble block has a high glass transition temperature, T_g. In this case so-called frozen micelles are formed where the micellar properties depend strongly on the way of preparation and also no unimer-micelle equilibrium is attainable. Thus, due to the low diffusion coefficient of the block copolymers a real equilibrium situation is rare or will be reached only after a long time period, opposed to the case for low molecular weight surfactants.

Chapter 3

Characterization methods

3.1 Scattering techniques

3.1.1 Static light scattering (SLS)

The phenomenon light scattering was first systematically investigated by John Tyndall in the second half of the 19th century.[48] He discovered that the intensity of the scattered light depends on the wavelength of the used light as well as on the angle of detection and that the scattered light is also partially polarized. The first theoretical description of scattering was developed by Lord Rayleigh and is based on Maxwell's theory of electromagnetic waves.[49] The fundamental idea is that the electrons of the outer shell of an atom or molecule interact with the incident electromagnetic wave and start to oscillate with the same frequency. These electrons act as an oscillating dipole and therefore emit light in all directions. The scattered light of a sample is the sum of all these single waves, which can interfere with each other and cause, for bigger particles, a characteristic angle dependence of the scattered intensity. In general, the scattered intensity depends on the polarizability, α, of the molecules. In SLS, the scattered intensity is averaged over a sufficient long time interval ($t > 0.1$ s), which is longer than the time scale of the molecular motion and, therefore, represents the system in thermodynamic equilibrium. The first term of a series expansion of $\alpha(t)$, which contributes to the scattering is $\langle \Delta\alpha^2 \rangle$, i.e. the scattered intensity is proportional to the mean change in polarizability squared. These changes can arise from local fluctuations in the density or concentration whereas in macromolecular and colloidal systems the influence of the first can be neglected. Debye[50, 51] showed that for a liquid two-component system

$$\left\langle \Delta\alpha^2 \right\rangle \propto n_0^2 RTc \left(\frac{\partial n}{\partial c}\right)^2 \left(\frac{\partial c}{\partial \Pi}\right)_T \tag{3.1}$$

where n_0 is the refractive index of the solvent, R is the gas constant, T is the absolute temperature, c is the concentration. n is the refractive index of the sample and Π is the osmotic pressure.

The so called Rayleigh ratio $R(\theta)$ can be expressed as

$$R(\theta) = \frac{I(\theta) r^2}{I_0} = \frac{4\pi^2}{\lambda_0^4 N_A} \cdot n_0^2 RTc \left(\frac{\partial n}{\partial c}\right)^2 \left(\frac{\partial c}{\partial \Pi}\right)_T \tag{3.2}$$

where I_0 is the incident intensity, $I(\theta)$ is the scattered intensity at angle θ, r is the distance between sample and detector, λ_0 is the wavelength of the light in vacuum and N_A is Avogadro's number.

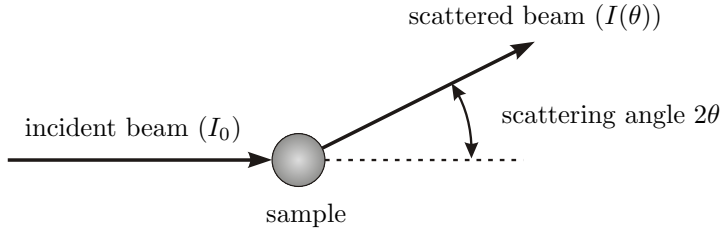

Figure 3.1: General scheme of the scattering process (elastic scattering).

For polymer and colloidal solutions it is useful to subtract the scattering of the solvent from the whole scattering intensity and it is assumed to be done for all following considerations. According to Debye[51] it is favorable to write eq.(3.2) in reciprocal form, which gives

$$\frac{Kc}{R(\theta)} = \frac{1}{RT} \cdot \left(\frac{\partial \Pi}{\partial c}\right)_T \tag{3.3}$$

with

$$K = \frac{4\pi^2}{\lambda_0^4 N_A} \cdot n_0^2 \left(\frac{\partial n}{\partial c}\right)^2 \tag{3.4}$$

The term $(\partial\Pi/\partial c)_T$ is called the osmotic module and can be expanded into a power series by that the right hand side of eq.(3.3) can be written as

$$\frac{1}{RT} \cdot \left(\frac{\partial \Pi}{\partial c}\right)_T = \frac{1}{M_w} + 2A_2 c + 3A_3 c^2 + \ldots \tag{3.5}$$

where M_w is the weight-average molecular weight of the solute and A_2, A_3, etc. are virial coefficients, which describe interactions between the macromolecules. Combining eq.(3.3) and eq.(3.5) and neglecting higher order terms of c yields

$$\frac{Kc}{R(\theta)} = \frac{1}{M_w} + 2A_2c \tag{3.6}$$

The latter expression is valid for particles with a diameter smaller than $\lambda/20$. According to the Mie theory[52], for bigger particles one has to introduce a particle scattering or form factor as the scattering becomes sensitive to the shape of the scattering object. For the single contact approximation i.e. when the macromolecules or particles interact just at one point, Zimm[53] could show that, without restriction on the particle shape, eq.(3.6) can be written as

$$\frac{Kc}{R(\theta)} = \frac{1}{M_w P(q)} + 2A_2c \tag{3.7}$$

where $P(q)$ is the form factor at high dilution and q is the absolute value of the scattering vector, defined as

$$q = \frac{4\pi n_0}{\lambda_0} \cdot \sin(\theta) \tag{3.8}$$

For particles with $qR_g < 1$, the form factor is identical regardless of the particle shape and can be approximated by

$$P(q) = 1 - \frac{1}{3}\left\langle s^2 \right\rangle q^2 + \ldots \tag{3.9}$$

where $\langle s^2 \rangle$ is the mean square radius of gyration $\left(R_g = \sqrt{\langle s^2 \rangle}\right)$. Thus, introducing eq.(3.9) into eq.(3.7) yields

$$\frac{Kc}{R(\theta)} = \frac{1}{M_w} + \frac{1}{3}\,\frac{R_g^2}{M_w}\,q^2 + 2A_2c \tag{3.10}$$

The latter equation is typically used for the so-called Zimm plot where $\frac{Kc}{R(\theta)}$ is plotted *versus* $(q^2 + kc)$ with k being a constant (see Fig.(3.2 a)). From this plot, one can calculate the weight-average molecular weight of the solute, M_w, the second virial coefficient, A_2,

and the radius of gyration, R_g.

For particles with $qR_g > 1$, the shape has a significant influence on the angle dependence of the scattered light. Very characteristic for each shape is the behavior at high qR_g values, which can be used in the so-called Kratky plot[54] ($q^2R(\theta)$ *versus* q) to distinguish them (see Fig.(3.2 b)).

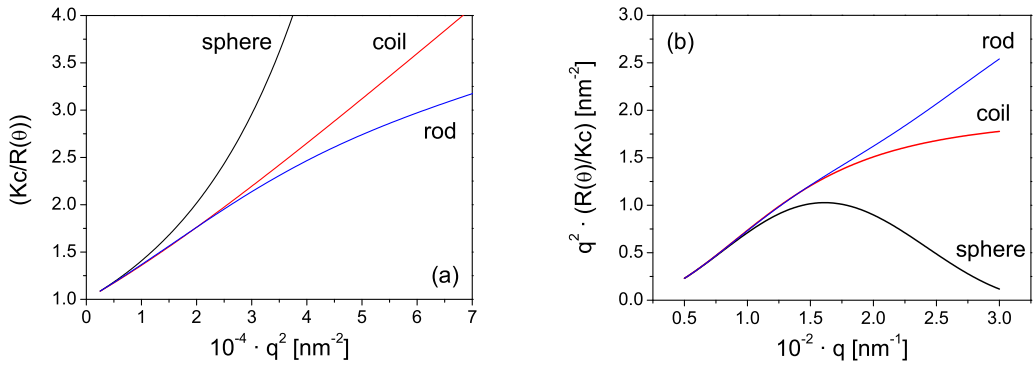

Figure 3.2: Zimm plot (a) and Kratky plot (b) of a sphere, a coil and a rod. (R_g = 100 nm)

3.1.2 Dynamic light scattering (DLS)

Contrary to static light scattering, in dynamic light scattering the scattered intensity is not averaged over a certain time period but correlated. The movement of the molecules in the solution causes a Doppler broadening, $S(\omega)$, of the frequency spectrum of the scattered light. As the motion is rather slow, the broadening of the spectrum is very small and cannot be resolved in the experiment. Therefore, the experimentally better accessible intensity-time correlation function $g_2(t)$ is measured instead, which is given by

$$g_2(t) = \frac{\langle I(t)I(t+\tau)\rangle}{\langle I(t)\rangle^2} \tag{3.11}$$

The correlation function of the electric field $g_1(t)$ can be derived by using the Siegert relation[55]:

$$g_1(t) = \sqrt{\frac{g_2(t) - b}{b}} \tag{3.12}$$

where b is the experimentally determined baseline. The relation between $g_1(t)$ and the Doppler broadening, $S(\omega)$, is given according to the Wiener-Khintchine theorem[56, 57] as a Fourier transformation[58]:

$$g_1(t) \propto \int_0^\infty S(\omega) \exp(-iq\omega t) d\omega \tag{3.13}$$

For a monodisperse and highly diluted polymer system ($qR_g \ll 1$), $g_1(t)$ decays as a single-exponential function

$$g_1(t) = B \cdot \exp(-q^2 Dt) \tag{3.14}$$

where B is the signal-to-noise ratio and D is the translational diffusion coefficient. For polydisperse systems and large particles, $g_1(t)$ has a multi-exponential decay. One way to analyse the data is to apply a cumulants fit to the logarithmic correlation function

$$\ln(g_1(t)) = -\Gamma t + \frac{k}{2} \Gamma^2 t^2 - \frac{k'}{6} \Gamma^3 t^3 + \ldots \tag{3.15}$$

with

$$\Gamma = D_{app}(q)\ q^2 \tag{3.16}$$

and in the limit of small q one obtains

$$\lim_{q \to 0} D_{app}(q) = D_z \tag{3.17}$$

where D_z is the z-averaged diffusion coefficient. The higher cumulants k and k' are a measure of the polydispersity of the system.
With the assumption of hard spherical particles, one can calculate the hydrodynamic radius, R_h, of the scattering objects via the Stokes-Einstein equation

$$R_h = \frac{k_B T}{6\pi\eta_0 D} \tag{3.18}$$

where k_B is the Boltzmann constant, T is the absolute temperature and η_0 is the viscosity of the solvent.

3.1.3 Small angle X-ray scattering (SAXS)

Small angle X-ray scattering is a well-established technique for the characterization of structures in the range of 1 - 100 nm. From the scattering curve, one can determine the size and the shape of the scattering object. Since the wavelength of X-rays is much shorter compared to light (10^{-4} nm - 10 nm), the scattering arises from the interaction of the radiation with the electron shell of the atoms. The most common used X-ray is the copper K_α radiation with a wavelength of 0.1542 nm.

The scattering amplitude of the whole sample is a linear superposition of all scattering waves from each scattering center at position $\vec{r}_n$ (Fraunhofer approximation) and can be described by

$$A(\vec{q}) = \sum_{n=1}^{N} \rho_n \exp(i\vec{q}\,\vec{r}_n) \tag{3.19}$$

$$\text{with} \quad \vec{q} = \vec{k}_1 - \vec{k}_0 \quad \text{and} \quad |\vec{q}| = q = \frac{4\pi}{\lambda}\sin(\theta)$$

where $\vec{k}_0$ and $\vec{k}_1$ are the wave vectors of the incident and scattered beam, respectively and ρ_n is the scattering power (Fig.(3.3)). For real systems with an electron density distribu-

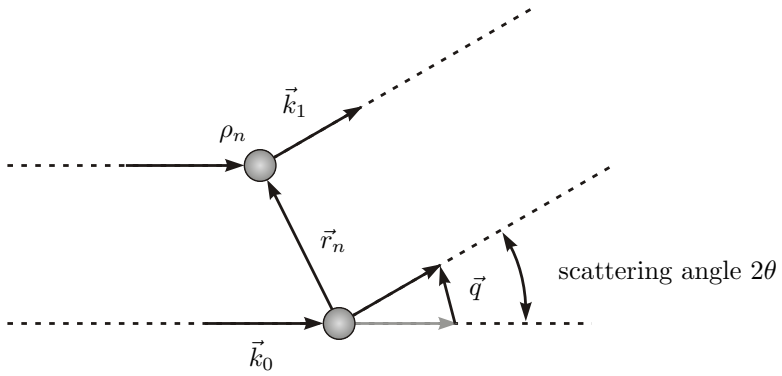

Figure 3.3: Scheme of the scattering on two scattering centers.

tion, $\rho(\vec{r})$, the complex scattering amplitude can be written as the Fourier transformed of $\rho(\vec{r})$

$$A(\vec{q}) = \mathscr{F}\left(\rho(\vec{r})\right) = \int_V \rho(\vec{r}) \exp(i\vec{q}\,\vec{r})\; dV \tag{3.20}$$

Thus, by knowing the electron density distribution one can calculate the scattering amplitude as the Fourier transformation is one-to-one. However, experimentally, only the

scattering intensity, $I(\vec{q})$, is accessible, which is the squared absolute value of the complex scattering amplitude:

$$I(\vec{q}) = |A(\vec{q})|^2 = A^*(\vec{q})A(\vec{q}) = \int_V P(\vec{r}) \exp(i\vec{q}\vec{r})\ dV \tag{3.21}$$

where $P(\vec{r})$ is a autocorrelation function or so-called Patterson function. Thus, the scattering intensity is a Fourier transform of the Patterson function ($I(\vec{q}) = \mathscr{F}(P(\vec{r}))$). During the measurement, the phase information is lost and, therefore, the electron density distribution is not unambiguously determinable from the scattering intensity. The relations between the parameters in real and reciprocal space are shown in Figure (3.4).

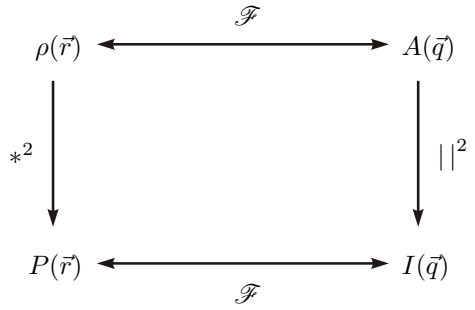

Figure 3.4: Scheme of the relations between the parameters in real and reciprocal space.

The scattering on macromolecules in dilute solution shows no interparticular scattering, which is the interference of scattered waves from different particles, and gives information about the shape and size of the single particle. The particle scattering curve can be written as a sum of all scattering intensities of the single particles averaged over all spacial positions caused by the Brownian motion[59]

$$I(\vec{q}) = N_p \left| \int_{V_p} (\rho(\vec{r}) - \rho_s) \exp(i\vec{q}\vec{r})\ d\vec{r} \right|^2 = N_p K^2 \left|F(q)\right|^2 = N_p K^2 P(q) \tag{3.22}$$

where N_p is the number of particles, V_p is the volume of the particle, ρ_s is the electron density of the solvent, K is a contrast factor, which is for particles with a homogeneous electron density ($\rho(\vec{r}) = \rho$) $K = V_p(\rho - \rho_s)$, $F(q)$ is the scattering amplitude of the particle with

$$F(q) = \frac{1}{V_p} \int_{V_p} \exp(i\vec{q}\vec{r})\ d\vec{r} \tag{3.23}$$

According to Rayleigh[60], for monodisperse spheres, the average over all particle orientations relative to $\vec{q}$ yields

$$\langle \exp(i\vec{q}\,\vec{r}) \rangle = \frac{\sin qr}{qr} \tag{3.24}$$

Thus, from eq.(3.23), the scattering amplitude of a sphere with radius R is[61]:

$$F(q) = \frac{3\left[\sin(qR) - qR\cos(qR)\right]}{(qR)^3} \tag{3.25}$$

Figure(3.5) shows the form factor $P(q) = |F(q)|^2$ for monodisperse homogene spheres with radius, R, which is proportional to the scattering intensity (ref. eq.(3.22)). Very charac-

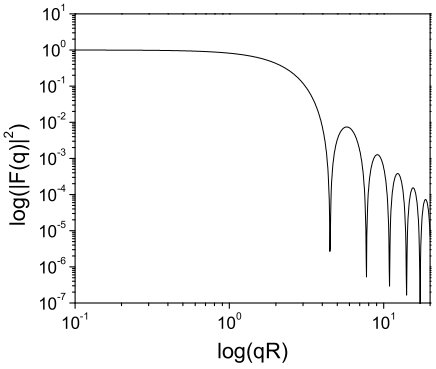

Figure 3.5: Form factor $P(q) = |F(q)|^2$ for monodisperse homogene spheres with radius R

teristic are the minima and maxima starting with the first minima at about $qR = 4.49$. With increasing polydispersity of the radius, the sharp minima fade out and eventually disappear. For many particle shapes the form factor is known[62] and one can try to find the best fit to the measured data. Another characteristic feature of SAXS curves is the behavior for $q \to \infty$. Independent of the particle shape, the scattered intensity will decrease with q^{-4}. This asymptotic behavior can be described by the Porod approximation[63] for $q > 1/R_g$

$$P(q) = |F(q)|^2 = \frac{2\pi S_p}{V_p^2}\, q^{-4} \tag{3.26}$$

where S_p is the surface of the particle.

In the region of small q values ($qR_g < 1$) and for particles with statistic orientation, the exponential function in eq.(3.22) can be approximated by (Guinier approximation)

$$I(q) \approx N_p K^2 \exp(-\frac{R_g^2}{3} q^2) \approx N_p K^2 (1 - \frac{R_g^2}{3} q^2) \tag{3.27}$$

whereas the radius of gyration R_g is defined as

$$R_g^2 = \frac{1}{K} \int_{V_p} [\rho(\vec{r}) - \rho_s] \, r^2 \, d\vec{r} \tag{3.28}$$

which, for spherical particles with radius R, yields $R_g^2 = 3R^2/5$. From the so-called Guinier-plot where $\ln(I(q))$ is plotted *versus* q^2, one can determine the radius of gyration from the slope of the curve in the small q region.
For SAXS curves of measurements where the absolute scattered intensity and the contrast is known, the extrapolation $q \rightarrow 0$ yields the volume of the particle V_p . Thus, from eq.(3.22) follows as $P(q) = 1$

$$I(q) = N_p K^2 = N_p (\rho - \rho_s)^2 V_p^2 \tag{3.29}$$

Nowadays, sophisticated computer programs are available for the analysis of SAXS curves where information from other techniques is used to create a model, which can be then fitted to the experimental data.

3.2 Analytical ultracentrifugation (AUC)

The analytical ultracentrifuge was developed by Thé Svedberg[64] in the 1920's and is a very powerful and versatile method for the determination of the molecular weight and the hydrodynamic and thermodynamic properties of macromolecules and colloids. The data obtained from an AUC experiment is a record of the concentration distribution in the sample cell at a given time. This can be done by absorption or interference measurements since both the absorbance and refractive index of the sample are proportional to the sample concentration.

3.2.1 Sedimentation velocity

The effective force on a particle in a solvent, which is subjected to a gravitational field is composed of three forces. The downward force is the centrifugal force, F_c, in AUC, which is proportional to the square of the angular velocity.

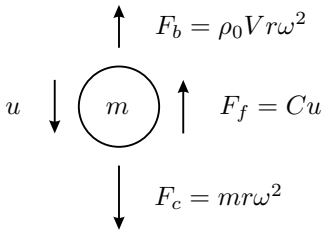

Figure 3.6: Forces on a particle in a solvent when subjected to a gravitational field. u is the sedimentation velocity.

The two upward forces are the buoyancy force, F_b, equal to the weight of the displaced fluid, and the frictional force, F_f, proportional to the velocity of the particle.
The effective force exerted on the particle can be expressed by

$$F_{eff} = m\frac{du}{dt} = F_c + F_b + F_f = mr\omega^2 - \rho_0 V r\omega^2 - Cu \tag{3.30}$$

where u is the velocity of the particle, r is the distance of the sample from the center of rotation, ω is the angular velocity, ρ_0 is the density of the solvent, m is the mass of the particle, V is the volume of the particle and C is the frictional coefficient of the particle. After a short time of spinning, the net force on the particle becomes zero and the particle moves with a velocity u_s, called, the sedimentation velocity. Thus, from eq.(3.30) follows

$$m(1 - \bar{v}\rho_0)r\omega^2 = Cu_s \tag{3.31}$$

where $\bar{v}$ is the partial specific volume of the particle. In the first approximation, the particle is a hard sphere, so that the frictional coefficient, C, is given by Stokes' law, which, on substitution into eq.(3.31), gives the apparent molar mass of the particle

$$M_{app} = 9\pi\sqrt{2\bar{v}}N_A\left[\frac{\eta u_s}{(1 - \bar{v}\rho_0)r\omega^2}\right]^{3/2} \tag{3.32}$$

where η is the viscosity of the solvent and N_A is Avogadro's number.
Since the centrifugal force increases with r, the sedimentation velocity will also increase gradually and must be expressed as a differential

$$s \equiv \frac{u_s}{r\omega^2} = \frac{dr_b}{r\omega^2 dt} \tag{3.33}$$

where s is the sedimentation coefficient, and r_b is the radial position of the sedimenting boundary. Integration of eq.(3.33) leads to a linear expression, which can be used for a simple determination of s from experimental data

$$\ln\left(r_b/r_m\right) = s\omega^2 t \tag{3.34}$$

where r_m is the radial position of the meniscus.

Introducing eq.(3.33) into eq.(3.32) leads to an expression for the apparent molecular weight, which contains only measurable values

$$M_{app} = 9\pi\sqrt{2\bar{v}}N_A\left[\frac{\eta s_0}{(1-\bar{v}\rho_0)}\right]^{3/2} \tag{3.35}$$

where s_0 is the sedimentation coefficient that has been extrapolated to zero concentration, because it is found that the experimental value of s depends significantly on the concentration of the solution. Therefore eq.(3.35) is strictly valid only in the limit of infinite dilution where intermolecular interactions can be neglected.

Non associating particles show a decrease in the sedimentation coefficient with increasing concentration, which arises from the increased viscosity of the solution. For a limited range of concentrations one can describe this dependency by

$$s = \frac{s_0}{(1+k_s c)} \tag{3.36}$$

where k_s is the concentration-dependent coefficient.[65] This coefficient is a very useful property for the determination of the shape of the particles. Together with the intrinsic viscosity, $[\eta]$, one can calculate the so-called Wales/van Holde ratio, $R = k_s/[\eta]$.[66] Theoretically and empirically it has been shown that for neutral random-coil polymers and also for compact spherical particles this ratio is about 1.6 and for elliptical and rod-like particles it tends towards zero.[67]

From the shape of the sedimenting boundary, one can determine the distribution of the sedimentation coefficient, which is a measure for the polydispersity of the particles and, with this, the molar mass distribution. The experimental data of the concentration gradient can be transformed directly into the distribution of the sedimentation coefficient by a method of Signer and Gross[68]

$$g(s) = \frac{1}{c_0}\frac{dc_0}{ds} = \frac{1}{c_0}\frac{dc}{dr}\left(\frac{r}{r_m}\right)^2\left(r\omega^2 t\right) \tag{3.37}$$

This method is a simplification of a rather complex problem and exclusively applicable when the spreading of the boundary is only due to heterogeneity of the sample allowing diffusion and self-sharpening effects to be neglected. A more detailed discussion of this topic is given in the book of Howard Schachman.[65]

3.2.2 Sedimentation equilibrium

In a sedimentation equilibrium experiment, the angular velocity of the sample cell is lower than that required for the measurement of the sedimentation velocity. When the solute starts to sediment, this process is opposed by the diffusion. After some time, these two processes reach an equilibrium and the concentration increases exponentially towards the bottom of the cell. It can be shown that, for an ideal, non associating particle:[69]

$$M_{w,app} = \frac{2RT}{(1-\bar{v}\rho_0)\omega^2}\cdot\frac{d(\ln\, c(r))}{dr^2} \tag{3.38}$$

where $M_{w,app}$ is the apparent weight-average molecular weight, R is the gas constant and T is the absolute temperature. The molecular weight is named "apparent" because it is related to a certain initial concentration. From the relative concentration distribution, $c_{rel}(r)$, one can calculate the absolute concentration distribution, $c(r)$, by

$$c(r) = c_m + c_{rel}(r) \tag{3.39}$$

The concentration at the meniscus, c_m, can be determined by the concentration balance in the cell, which yields

$$c_m = c_0 - \frac{1}{r_b - r_m}\cdot\int_{r_m}^{r_b} c_{rel}(r)dr \tag{3.40}$$

in which c_0 is the initial concentration. According to eq.(3.38), the molecular weight can be extracted from the linear slope of a plot of $\ln c(r)$ *versus* r^2. However, this method is not always suitable because polydispersity gives a pronounced curvature. A more versatile method is the fit of the experimental data. Combination of eq.(3.38), (3.39) and (3.40) leads to

$$M_{w,app} = \frac{2RT}{(1-\bar{v}\rho_0)(r_b^2 - r_m^2)\omega^2} \cdot \frac{c_b - c_m}{c_0} \tag{3.41}$$

The experimental concentration distribution can be approximated by a sum of positive exponential functions

$$c(x) = \sum_{i=1}^{n} k_i \cdot \exp(a_i x) \qquad (a_i, k_i > 0) \tag{3.42}$$

where x is a dimensionless rotor coordinate with

$$x = \frac{r^2 - r_m^2}{r_b^2 - r_m^2} \tag{3.43}$$

Substitution into eq.(3.41) yields

$$M_{w,app} = \frac{2RT}{(1-\bar{v}\rho_0)(r_b^2 - r_m^2)\omega^2} \cdot \frac{\sum k_i \cdot \exp(a_i - 1)}{c_0} \tag{3.44}$$

To obtain the weight-average molecular weight, one has to determine the apparent molecular weight at different concentrations and then extrapolate to zero concentration.

3.3 Microscopy

3.3.1 Atomic force microscopy (AFM)

The atomic force microscope was invented in 1986 by Binning, Quate and Gerber[70] and is today one of the most widely used imaging techniques for providing information on the molecular and atomic scale. It is considered to be a very versatile and non-destructive tool used to probe the local physical and chemical properties of surfaces. The measuring method is rather simple: A sharp tip (radius 5 - 50 nm), which is mounted on a flexible cantilever is scanned over the sample surface by a piezoelectric crystal. The tip can either be pressed with a constant force onto the sample or held at a constant height above the sample. The up and down movement of the tip is measured by a laser beam, which is reflected from the top side of the cantilever and detected with a position-sensitive photo diode. In contrast to optical microscopy, the lateral resolution of an AFM is determined by the size of the tip. The three most used measuring modes are the contact, non-contact and tapping modes. In the contact mode, the tip is pressed onto the surface

with a constant force. While scanning over the sample, the cantilever bends according to the topography. These changes are compensated by the piezo crystal, which moves the sample vertically to maintain a constant force between the tip and sample. Thus, the movements of the piezo give a direct image of the height profile of the sample. On the contrary, in the non-contact mode, the tip is held close to the surface and the bending of the cantilever caused by attractive or repulsive forces between surface and tip, which can be electrostatic or magnetic forces is measured. In the tapping mode, the cantilever vibrates near its resonance frequency (100 - 400 kHz) and with an amplitude between 10 - 150 nm. When the tip nears the sample surface, the van der Waals interaction between the sample and the tip will dampen the oscillation. This change is used as a measure of height as the force is strongly dependent on the distance. The advantage of the tapping mode is that the tip is touching the surface only for a short time, reducing shear forces and thus the risk of changes or damages to the sample. Thus, the tapping mode is the mode mostly used for fragile, soft matter surfaces such as polymers and biological tissues.

3.3.2 Electron microscopy (EM)

The basis of the electron microscope was developed in 1924 when Louis de Broglie[71] proposed that particles like electrons and neutrons could exhibit wave characteristics under certain circumstances. Three years later, the wave nature of the electron was experimentally confirmed by C.J. Davisson et al.[72] and G.P. Thomson[73]. De Broglie's theory of electron matter waves gives the correlation between the impulse, p, of the electron and its wavelength, λ:

$$\lambda = \frac{h}{p} = \frac{h}{m_e v} \tag{3.45}$$

where h is the Planck constant, m_e is the relativistic mass of the electron and v is the velocity of the electron.

With this precondition, an electron beam can be used in the same way as light for microscopic imaging and due to its small wavelength (0.02 - 0.05 nm), the resolution is in the sub-nanometer range. The setup of an electron microscope is similar to a normal light microscope. The electrons are generated in a hot cathode and accelerated by application of a high voltage (60 - 200 kV). Electromagnetic lenses focus the beam on the sample and also make it possible to scan over the sample. The whole setup is placed in a high vacuum chamber to avoid collisions of the electrons with air molecules. Depending on the sample

nature, one can use two different techniques, transmission electron microscopy (TEM) or scanning electron microscopy (SEM). For TEM measurements, the sample is placed on a carbon-coated copper grid where the thickness of the layer should be smaller than 100 nm. The contrast of the image arises through the absorption and scattering of the electrons by the sample material: sample parts with high electron density or larger thickness are dark. Therefore, to highlight special regions one can stain the sample selectively with heavy metal-containing substances (e.g. osmium tetraoxide, ruthenium tetraoxide).
A special preparation technique, which is very powerful for the investigation of polymer structures in aqueous solution is the so-called cryo-TEM. Here, a liquid sample is shock-frozen e.g. in liquid nitrogen or liquid pentane to prevent the formation of ice crystals and then cut in very thin slices. The measurement is done at low temperatures to avoid melting of the sample.
SEM images of bulk samples can be done by first covering the sample surface with a conductive layer e.g. gold or carbon to avoid a charging of the sample. When the electron beam hits the surface, secondary electrons are generated and detected above the sample. Thereby, the intensity of the secondary electrons is dependent on the topography of the surface, which gives the contrast of the image. The speciality of SEM is its high depth resolution, which gives good 3D image impressions.

3.4 Isothermal titration calorimetry (ITC)

Isothermal titration calorimetry is an important method for the understanding of chemical reactions and molecular interactions since a change in composition or organization is associated with release or uptake of heat. The calorimeter contains a reference cell and a measuring cell of precise volume, which are mounted in an adiabatic jacket. Both cells are filled with the same solution and kept at a constant temperature. The sample solution is injected with a microsyringe stepwise in small aliquots (5 - 20 μl) while the syringe itself rotates constantly and acts as a stirrer. The heat required to keep the reference and measuring cells at the same temperature is measured as a function of time. For exothermic reactions, one gets negative peak signals as the instrument stops heating the measuring cell to compensate for the released heat. Consequently, endothermic reactions give positive peak signals. Thus, each injection can be characterized by the heat, q, and the injected amount of substance, δn.

3.5 Density, viscosity and surface tension

Density. The density of a solution can be easily determined by the measurement of the resonance frequency of a U-shaped quartz pipe, which is filled with the sample solution. Since the geometry of the quartz pipe is fixed, the resonance frequency only depends on the weight of the solution and therefore, since the volume is constant, on the density. This means, after calibration of the instrument with solvents of known density one can correlate the measured frequency directly with the density. A plot of the density of the solution *versus* the concentration yields a straight line with the slope $(1 - \bar{v}\rho_0)$ where $\bar{v}$ is the partial specific volume of the solute and ρ_0 is the density of the solvent. The partial specific volume is a property of the solution and is not the same as the reciprocal of the density of the solid polymer. The value $(1 - \bar{v}\rho_0)$ represents the buoyancy, which is important for the data analysis of the analytical ultracentrifugation measurements. For $(1 - \bar{v}\rho_0) > 0$, the solute sediments and for negative values of $(1 - \bar{v}\rho_0)$ the solute floats.

Viscometry. Viscometry is an experimentally relative simple method, which provides information on the hydrodynamic properties of micellar solutions. The viscosity measurements in this work were done with an Ubbelohde capillary viscometer.[74] With this method, one compares the flow times of solutions at different concentrations with the flow time of the solvent. Since the flow velocity in the capillary is inversely proportional to the viscosity of the fluid (Hagen-Poiseuille), the relative viscosity can be written as

$$\eta_r = \frac{\eta}{\eta_0} = \frac{t}{t_0} \tag{3.46}$$

where t and t_0 are the flow time of solution and solvent, respectively. This value is always greater than unity as the presence of the solute increases the viscosity. This fractional increase is called the specific viscosity and is given by

$$\eta_{sp} = \frac{\eta - \eta_0}{\eta_0} = \eta_r - 1 \tag{3.47}$$

The specific viscosity is strongly dependent on the concentration, c, of the solution and for noninteracting solutes this can be expressed by

$$\frac{\eta_{sp}}{c} = [\eta] + k_{SB}\,[\eta] \cdot \eta_{sp} \tag{3.48}$$

where η_{sp}/c is the reduced viscosity, $[\eta]$ is the intrinsic viscosity and k_{SB} is a constant, which is termed the Schulz-Blaschke coefficient.[75] For small concentrations, this relationship is equivalent to

$$\frac{\eta_{sp}}{c} = [\eta] + k_H [\eta]^2 \cdot c \tag{3.49}$$

where k_H is the so-called Huggins coefficient.[76] Thus, the intrinsic viscosity can be determined simply by extrapolating the experimental data to zero specific viscosity or concentration.

Surface tension. In this study, the surface tension of a solution was determined by the pendant drop method, which has a big versatility of application for numerous liquid-vapor and liquid-liquid interfaces and was mainly developed by E. A. Hauser and coworkers.[77] The main advantage of this static method is that the surface is untouched after the drop has formed. Thereby, the kinetics of the surface formation can be studied, which is important for many colloidal systems.

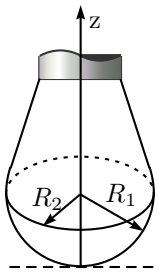

Figure 3.7: Scheme of the hanging drop. R_1 and R_2 are the two main radii of curvature.

During the measurement, a camera records a picture of the hanging drop in equal time intervals. For the determination of the surface tension, one uses a theoretical curve to fit the experimental drop shape whereas the surface tension itself is used as fit parameter. The relation between the shape of the hanging drop and the interfacial tension, γ, can be described by the Laplace equation[78]

$$\gamma \cdot \left(\frac{1}{R_1} + \frac{1}{R_2} \right) = \Delta P_0 + \Delta\rho \cdot g \cdot z \tag{3.50}$$

where R_1 and R_2 are the two principal radii of curvature, ΔP_0 is the pressure difference at a reference plane, $\Delta\rho$ is the density difference between the drop and the medium, g is the gravitational acceleration and z is the vertical height of the drop measured from the reference plane.

Chapter 4

Results and discussion

Multicompartment micelles composed of a water-soluble shell and a segregated hydrophobic core have very interesting morphologies for nanotechnology, in particular for nanobiotechnology.[45] Thus, several strategies for preparing multicompartment micelles have been proposed in the past[79, 80, 81] and were recently reviewed.[45] However, up to now, the number of morphological studies concerning such micelles is rather low and therefore their exact inside structures are still quite unknown. One of the simplest pathways for preparing multicompartment micelles is the direct aqueous self-assembly of synthetic polymeric amphiphiles possessing one hydrophilic segment and two incompatible hydrophobic segments. Copolymers made of different segments covalently bonded together such as block, graft, star-block or miktoarm star copolymers can often spontaneously self-assemble into various organized superstructures.[4] Such self-assembly processes are driven by diverse repulsion forces between the segments. In a bulk material, the thermodynamic incompatibility between various segments attached together results in ordered segregated microphases.[82] In liquid media, the differences in affinity of the various segments for the solvent lead to dispersed organized objects. Either in bulk or in solution, the morphology of the self-assembled structures depends on the molecular architecture of the polymeric building blocks (number of segments, segment length, block sequence, architecture and composition).[4] Naturally, the more complex the starting copolymers, the more complicated is the analysis of the formed superstructures, particularly in solution due the dynamic behavior of most self-assemblies. For copolymers composed of only two different segments (AB), the factors governing self-assembly in solution are now well-understood and the formed morphologies include spherical micelles,[83] worm-like micelles[84] and vesicles.[85] However, for more complex macromolecules such as copolymers made of three distinct

segments (ABC), the possibilities of self-assembly in solution remain rather unexplored, although some morphologies have been characterized in both aqueous and organic media. The simplest case is when two of the three ABC segments are soluble in the solvent. In this case, spherical micelles possessing an insoluble inner-core and a mixed-arm soluble shell are obtained.[86, 87, 88] On the other hand, when two of the three ABC segments are insoluble in the solvent, the exact morphology of the resulting self-assemblies are generally more difficult to describe. The general shape of the superstructure is easy to characterize: spherical micelles[42, 43, 89] and vesicles[89, 90] have been prepared from ABC copolymers possessing two insoluble segments, however; the morphology of the inner core is usually hard to elucidate. Most likely, if the two blocks composing the core are large enough and thermodynamically incompatible, they should segregate into different phases, forming two or more separated compartments in the micellar core. Nevertheless, depending on the molecular structure of the segments, diverse morphologies can be expected for the formed compartments, e.g. "spheres in spheres" (core shell, onion like) or "spheres on spheres" (raspberry like). Up to now, the core structures have often been simply guessed (in most cases, core-shell was proposed) but have not been characterized or microscopically observed. Most recently, Lodge et al. reported the first convincing visualization by cryo-transmission electron micrographs (cryo-TEM) of multicompartment micelles prepared in aqueous media via self-assembly of miktoarm star copolymers.[46] Undeniably, their work indicates the coexistence of segregated regions in the hydrophobic core of the formed nanostructures. However, the precise morphology of this inner core has not been assessed.

4.1 Linear ABC triblock copolymer

4.1.1 Chemical characteristics

The solution properties of linear ABC triblock copolymers with two hydrophobic blocks in selective solvents have not yet been studied in detail. Eisenberg *et al.*[89] prepared an ABC triblock copolymer, polystyrene-*b*-poly(methyl methacrylate)-*b*-poly(acrylic acid) (PS-*b*-PMMA-*b*-PAA), and studied the morphologies it formed in organic solvents with different water content. Depending on the solvents and preparation conditions, various morphologies such as spherical, rod-like and vesicular structures could be observed. In our study, we investigate the aqueous self-assembly of a linear ABC triblock copolymer, poly(4-vinylbenzyl *N*-methylmorpholinium chloride)-*b*-polystyrene-*b*-poly(4-vinylbenzyl penta-

fluorophenol ether) (PVBM-*b*-PS-*b*-PVBFP) and the influence of the preparation method on the micellar morphology. The copolymer building-blocks were composed of a long

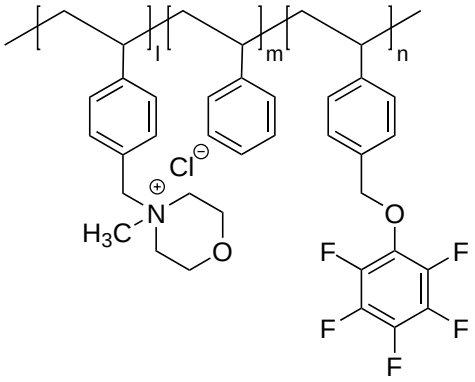

Figure 4.1: Chemical structure of poly(4-vinylbenzyl *N*-methylmorpholinium chloride)-*b*-polystyrene-*b*-poly(4-vinylbenzyl pentafluorophenol ether), (PVBM-*b*-PS-*b*-PVBFP).

cationic hydrophilic block, PVBM, and two short consecutive hydrophobic blocks: a hydrocarbon one (PS) and a hydrocarbon/fluorocarbon one (PVBFP). The copolymer PVBM-*b*-PS-*b*-PVBFP was obtained via quaternization of a poly(vinylbenzyl chloride)-*b*-PS-*b*-PVBFP precursor with *N*-methylmorpholine according to a previously reported procedure.[91] The triblock precursor was initially prepared via a three-step reversible addition-fragmentation transfer (RAFT) polymerization process using benzyl dithiobenzoate as a chain transfer agent. After each step, the block lengths were determined by size

Table 4.1: Polymer characteristics of PVBM-*b*-PS-*b*-PVBFP.

sample-ID	l*	m*	n*	M_n [g/mol]*	M_w/M_n^*
TB1	71	47	10	19000[a]	1.70

* determined by SEC, [a] before quaternization

exclusion chromatography (SEC). The obtained values are shown in Table (4.1). The estimation of the block lengths by ^{1}H NMR spectroscopy reveal 56 units for the polystyrene block and 16 units for the PVBFP block. These are higher values than those calculated by SEC but they are within the experimental error.

4.1.2 Self-assembly in aqueous media

The micellar solutions were prepared in two different ways in order to investigate the influence of the preparation method on the particle morphology. The first method of preparation was dissolution of the triblock copolymer PVBM-*b*-PS-*b*-PVBFP in a solvent mixture water/dioxane (1:1), which was subsequently dialyzed stepwise against water-dioxane mixtures with increasing concentration of water. The water content of the dialysis solutions were 70%, 76%, 83%, 92% and finally pure water. The alternative way of preparation was dissolution of the copolymer in a solvent mixture water/tetrahydrofuran (THF) (1:1) followed by the evaporation of THF at 50 °C in an ultrasonic bath. Both methods lead to a clear slightly yellowish micellar solution.

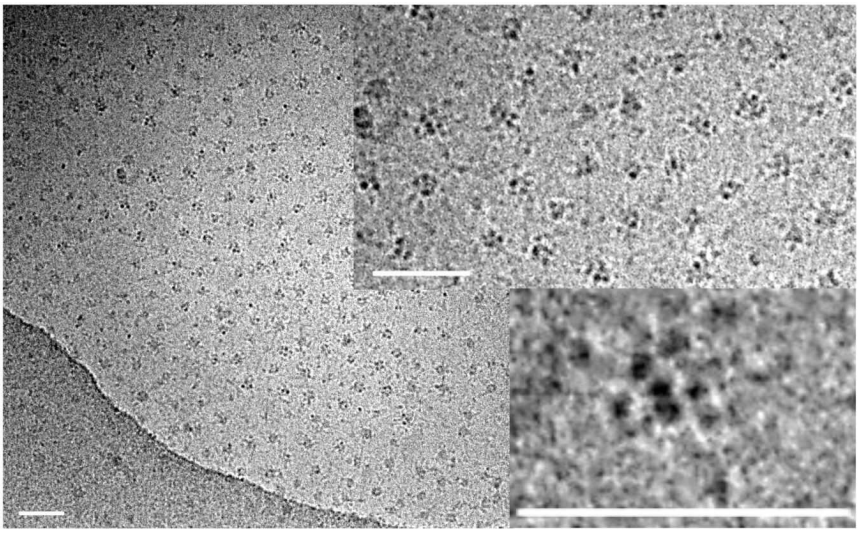

Figure 4.2: Cryo-TEM micrographs of PVBM-*b*-PS-*b*-PVBFP in aqueous media prepared by dialysis from dioxane. Scale bar = 50 nm

Cryo-transmission electron microscopy was used to determine the morphology of the micelles. Figure (4.2) shows typical cryo-TEM micrographs of the obtained aqueous solution prepared by dialysis from dioxane. The images reveal uniformly dispersed spherical objects possessing an average diameter of 12-15 nm. These objects correspond to the hydrophobic core of the formed micelles, which is composed of segregated domains: inside the sphere of the micellar core, dark spheres with an average diameter of about 3.4 ± 0.2 nm can be distinguished. Their considerable contrast can be attributed to the presence of electron-rich fluorine atoms.[46] On average, 4-10 segregated dark domains are observed for each micellar core. The water-soluble PVBM corona of the micelles is not directly

observable but can be estimated to be around 20-30 nm in diameter from the objects interdistance.

The observed core-morphology resembles a raspberry like morphology, as first described by Stadler *et al.* for the bulk self-assembly of polystyrene-*b*-polybutadiene-*b*-poly(methyl methacrylate) (SBM) triblock copolymers.[92] Pascault *et al.* demonstrated that the raspberry like morphology can also be observed in a micellar structure.[93, 94] In their study, micelles of SBM were initially dispersed in a reactive epoxy-amine solvent, which was subsequently polymerized. Their work indicated that the initial micelle morphology was fixed in the polymer matrix by polymerization and therefore could be precisely studied by TEM images.

The present work shows a first example of raspberry like morphology for micelles prepared in aqueous media. However, from the cryo-TEM images, it is not possible to determine whether the dark fluorocarbon domains cover the surface of a central hydrocarbon core (spheres on spheres situation, as described by Stadler *et al.*[92]) or whether the dark domains are embedded in the hydrocarbon core (spheres in spheres situation). Nevertheless, in the observed morphology, the segregated dark domains can contain either only the fluorocarbon moieties of PVBFP or the complete PVBFP blocks. To distinguish between these two scenarios the theoretical diameters of the micelle, core and fluorinated region were calculated and compared with the values estimated from cryo-TEM.

The molecular volumes of each segment of the copolymer PVBM-*b*-PS-*b*-PVBFP were calculated using theoretical models.[95] First, the molar van der Waals volume, V_w, for each repeating unit (i.e. VBM, S and VBFP) was calculated using group increments of van der Waals volume reported in the literature.[95] As requested for glassy and rubbery amorphous polymers,[95] V_w was multiplied by a correction factor of 1.6 in order to estimate the real molar volume of each repeating unit, V_r. The molecular volume, V_u, of each repeating unit was calculated via equation (4.1), where N_A is Avogadro's number.

$$V_u = V_r/N_A \tag{4.1}$$

The molecular volume, V, of each segment in the copolymer (i.e. PVBM, PS and PVBFP) was calculated according to equation (4.2), where N is the average degree of polymerization of each segment.

$$V = V_u \cdot N \tag{4.2}$$

Table (4.2) shows the volumes calculated for each segment in the copolymer.

Table 4.2: Calculated volumes for each segment in the PVBM-*b*-PS-*b*-PVBFP copolymer.

Repeating unit	V_w [cm^3/mol]	V_r [cm^3/mol]	V_u [nm^3]	Segment	N	V [nm^3]
VBM	137.53	220.05	0.365	PVBM	71	25.9
S	62.88	100.61	0.167	PS	47	7.85
VBFP	137.36	219.78	0.365	PVBFP	10	3.65

For the PVBFP segment , the molecular volume $V = 3.65$ nm^3 can be divided into a hydrocarbon molecular volume (backbone + benzyloxy group) $V_H = 1.94$ nm^3 and a fluorocarbon molecular volume (fluorinated ring) $V_F = 1.71$ nm^3.
The theoretical dimensions of the micelle were calculated considering two different scenarios already mentioned above. In the first, it was assumed that the spherical dark domains observed by cryo-TEM were only due to the fluorocarbon part of PVBFP (i.e. the fluorinated ring). In the second scenario, it was considered that the dark domains were containing complete PVBFP segments (i.e. both hydrocarbon and fluorocarbon moieties of PVBFP). In both cases, the calculations were made assuming a raspberry like morphology as shown in Figure (4.4) for the multicompartment micelle.

In the calculations, the experimental value of the diameter of the segregated dark domains of the core D_d was used, since this dimension could be measured precisely in the cryo-TEM images. The comparison of D_d with the molecular volumes, V, determined for the copolymer, allowed an estimation of the aggregation number of the micelle, Z, the diameter of the complete hydrophobic core, D_c, and the diameter of the complete micelle, D_m. The obtained latter value is expected to be slightly lower than the real value since the calculations do not take the aqueous swelling of the hydrophilic corona into account.

Scenario 1: Dark domains are only due to the fluorocarbon part of PVBFP. The dark domains have a diameter, D_d, of 3.4 nm. Thus, each of the domains has a volume, V_d, which can be calculated via equation (4.3).

$$V_d = \frac{4\pi}{3}\left(\frac{D_d}{2}\right)^3 \tag{4.3}$$

The number of copolymer chains per dark domain, n, can be calculated from V_d and from the molecular volume of the fluorocarbon part of PVBFP (for one chain), V_F, by

$$n = V_d/V_F \tag{4.4}$$

Thus, the aggregation number of the whole micelle, Z, can be determined via equation (4.5), where d is the average number of dark domains per micelle.

$$Z = d \cdot n \tag{4.5}$$

The volume of the hydrophobic core, V_c, can therefore be calculated via equation (4.6), where V_{PS} is the molecular volume of one PS segment and V_{PVBFP} is the molecular volume of one PVBFP segment (Table (4.2)).

$$V_c = Z \cdot (V_{PS} + V_{PVBFP}) \tag{4.6}$$

Then, D_c can be obtained through

$$D_c = 2 \cdot \left(V_c \cdot \frac{3}{4\pi} \right)^{1/3} \tag{4.7}$$

Similarly, the volume of the whole micelle, V_m, can be calculated by equation (4.8), where V_{PVBM} is the molecular volume of one PVBM segment (Table (4.2)), and D_m can be calculated via equation (4.9).

$$V_m = Z \cdot (V_{PVBM} + V_{PS} + V_{PVBFP}) \tag{4.8}$$

$$D_m = 2 \cdot \left(V_m \cdot \frac{3}{4\pi} \right)^{1/3} \tag{4.9}$$

Table (4.3)) shows the calculated values for this first scenario.

Table 4.3: Calculated micellar characteristics for the scenario where the spherical dark domains contain only fluorinated part of PVBFP segments.

V_d [nm^3]	n	d	Z	V_c [nm^3]	V_m [nm^3]	D_c [nm]	D_m [nm]
20.6	12	10	120	1380	4488	13.8	20.5

Scenario 2: Dark domains are due to both fluorocarbon and hydrocarbon parts of PVBFP. In this second scenario, the dark domains were considered to contain the complete PVBFP segments. Thus, the number of copolymer chains per dark domain, n, can be calculated from V_d and from the molecular volume of one PVBFP segment, V_{PVBFP}.

$$n = V_d/V_{PVBFP} \tag{4.10}$$

All the other values were calculated using equations (4.5)-(4.9). Table (4.4) gives the calculated values for this second scenario.

Table 4.4: Calculated micellar characteristics for the scenario where the spherical dark domains are due to both fluorocarbon and hydrocarbon parts of the block copolymer.

V_d [nm^3]	n	d	Z	V_c [nm^3]	V_m [nm^3]	D_c [nm]	D_m [nm]
20.6	6	10	60	690	2244	10.9	16.2

Only the first scenario permits a rigorous correlation between the micellar size measured by cryo-TEM and the molecular volumes of the copolymer blocks. For this scenario, the calculations result in a global theoretical diameter of 20.5 nm for the global micelle and a diameter of 13.8 nm for the whole hydrophobic core, which are in good agreement with the values derived from the cryo-TEM images. Swelling of the corona with water molecules and stretching of the PVBM chains due to the charges are not taken into account thus the calculated diameter of the whole micelle is a lower limit of the micellar size. In contrast, in the second scenario where it was assumed that the dark regions are due to the whole PVBFP blocks (hydrocarbon and fluorocarbon parts), the calculated diameters for the global micelle and for the hydrophobic core are too small. Therefore, we conclude

that the dark spheres constitute the fluorocarbon moieties of PVBFP only, whereas the dark gray region contains both the hydrocarbon domains of PS and PVBFP.

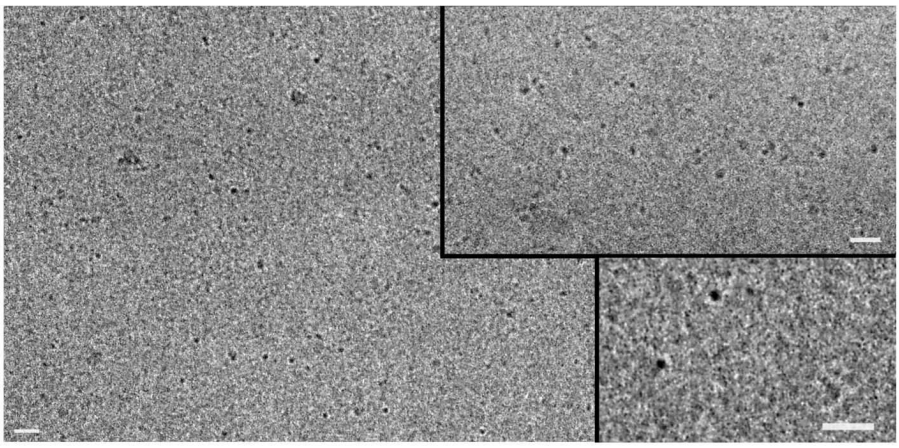

Figure 4.3: Cryo-TEM micrographs of PVBM-*b*-PS-*b*-PVBFP in aqueous media prepared by evaporation of THF, Scale bar = 25 nm.

Figure (4.3) shows cryo-TEM micrographs of the obtained aqueous solution prepared by evaporation of THF. The images clearly reveal uniformly dispersed spherical objects possessing an average diameter of 7.0 ± 0.5 nm. As previously mentioned, the contrast is due to the presence of electron-rich fluoro atoms. The water-soluble PVBM corona of the micelles as well as the hydrophobic hydrocarbon moieties could not be observed due to the low electron density contrast. A comparison of these micrographs with the ones obtained from the solution prepared from a solvent mixture water/dioxane (1:1) shows clear differences. In figure (4.2), one can see uniformly dispersed spherical objects composed of 4-10 segregated dark domains, which are attributed to a raspberry like morphology. However in the latter micrographs (figure (4.3)) only single dark domains are visible, indicating a layered core-shell-corona morphology. For the calculation of the theoretical dimensions it was assumed that the spherical dark domains in the micrograph were only due to the fluorocarbon part of PVBFP. The experimental diameter of the fluorocarbon dark spheres of the micelles (D_d = 7.0 nm) allows, through equation (4.3), calculation of a volume of 179.6 nm^3. The aggregation number of the micelle, Z, the diameter of the complete hydrophobic core, D_c, and the diameter of the complete micelle, D_m, were calculated by using equations (4.4)-(4.9) where d is 1 as there is just a single fluoro domain in the micellar core. (Table (4.5))

In conclusion, different final morphologies of the triblock copolymer micelles were ob-

Table 4.5: Calculated micellar characteristics for the core-shell-corona morphology.

V_d [nm^3]	n	d	Z	V_c [nm^3]	V_m [nm^3]	D_c [nm]	D_m [nm]
179.6	105	1	105	1208	3327	13.2	19.6

served depending on the micellar medium as well as method of preparation. Of interest to note is that the micelles prepared from the water/THF mixture are generally slightly smaller and less polydisperse than the ones prepared from the water/dioxane mixture. It is known that by changing the solvent or by using mixed solvents, different morphologies can be obtained from a single block copolymer.[89] This solvent-induced manipulation of the morphology arises from the different interaction parameters, χ, of the polymer blocks and the solvent.

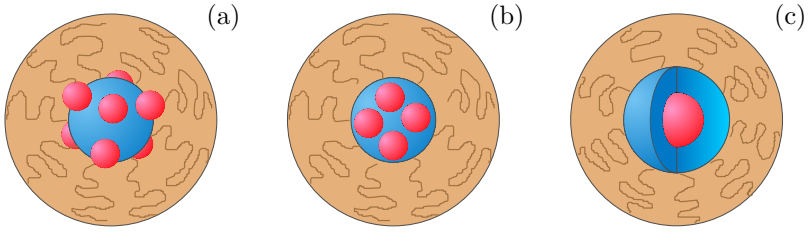

Figure 4.4: Schematic representation of: (a) the raspberry like (b) the sphere-in-sphere and (c) the core-shell-corona micellar morphology.

To confirm the dimensions of the micellar aggregates, the salt free aqueous solutions were analysed by static light scattering (SLS) and small angle X-ray scattering (SAXS). For the SLS measurements, toluene was used for calibration to determine the scattering volume-corrected Rayleigh ratio. Figure (4.5) shows the so-called Guinier plots where the logarithm of the inverse Rayleigh ratio is plotted as a function of the squared of the scattering vector. For small particles with $qR_g < 1$, the radius of gyration, R_g, can be determined by a linear fit of the Guinier plot according to equation (4.11)[96]

$$\ln(R(q)) \approx -\frac{1}{3}R_g^2 q^2 \tag{4.11}$$

The strong non-linearity of the Guinier plots can be explained by a high polydispersity of the micellar radius as was seen in the cryo-TEM micrographs as well as by the scattering

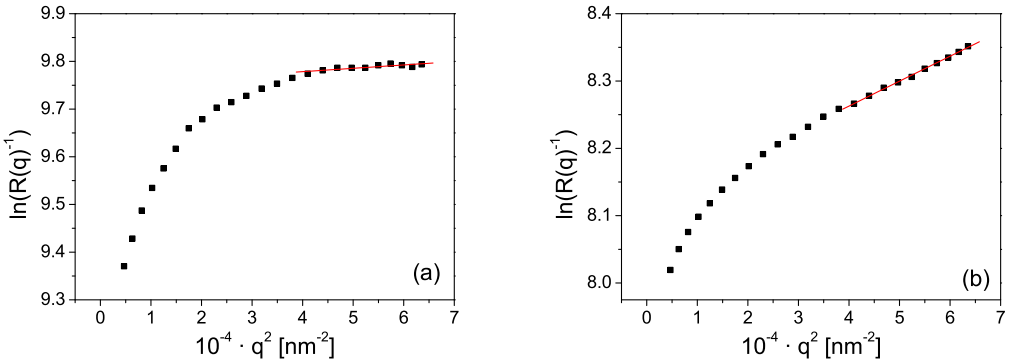

Figure 4.5: Guinier plots of PVBM-*b*-PS-*b*-PVBFP in salt free aqueous media prepared a) by dialysis from water/dioxane mixture and b) by evaporation of THF. The lines represent the linear fits, which were used for the calculation of the radius of gyration.

of a second species with a larger radius. The latter is considered to be agglomerates of micelles. As the scattered intensity is proportional to the radius to the power of six even small amounts of large particles in the solution cause a dramatic increase in the scattering intensity. Therefore, the curve was fitted only at higher q values, where the influence of the large particles is less pronounced. Thus the calculated radius of gyration was found to be 14.5 ± 1.6 nm for the solution prepared by dialysis from water/dioxane mixture and 33.3 ± 0.3 nm for the solution prepared by evaporation of THF. The values for the overall micellar size are slightly larger than the calculated values from the cryo-TEM micrographs. This is most probably due to the swelling of the corona by the solvent as well as additional stretching of the charged PVBM chains caused by coulombic repulsion, which was not taken considered in the theoretical calculations.

Figure (4.6) presents the SAXS curves obtained for the copolymer PVBM-b-PS-b-PVBFP in aqueous solution. The experimental SAXS data were fitted by a scattering curve for a system of polydisperse homogeneous spherical particles. The scattered intensity, $I(q)$, of an isotropic solution with a low particle density can be written as (according to eq.(3.22))

$$I(q) = N_p K^2 P(q) \tag{4.12}$$

where N_p is the number of particles, K is a contrast factor and $P(q)$ is the average form factor over the distribution, $f(R)$, of micellar radius, R:

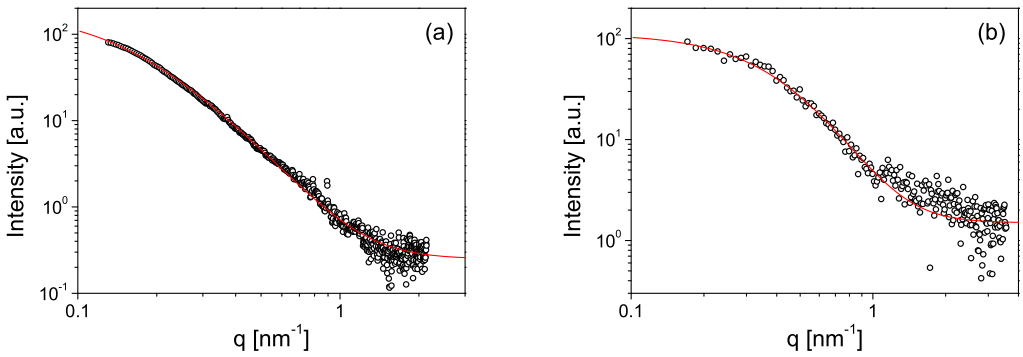

Figure 4.6: Small-angle X-ray scattering curves obtained for aqueous solution of PVBM-*b*-PS-*b*-PVBFP (c = 25 g/L) prepared a) by dialysis from water/dioxane mixture and b) by evaporation of THF. The solid lines represent the fits to the experimental data using a polydisperse sphere model.

$$P(q) = \int_{\infty}^{0} F(q,R)^2 f(R)\, dR \tag{4.13}$$

As a simple approximation of a spherical micelle, we used the well-known scattering amplitude, $F(q,R)$, of a uniform sphere (equation (3.25)). The polydispersity of the micellar radius was modeled by a Schulz-Zimm distribution

$$f(R) = \left(\frac{Z+1}{\bar{R}}\right)^{Z+1} \frac{R^Z}{\Gamma(Z+1)} \exp\left\{-\frac{(Z+1)R}{\bar{R}}\right\} \tag{4.14}$$

where $\bar{R}$ is the mean of the distribution, Z is a width parameter and $\Gamma(x)$ is the Gamma function. The root mean square deviation[59] from the mean radius is given by

$$\sigma_R = \frac{\bar{R}}{\sqrt{(Z+1)}} \tag{4.15}$$

The solid curves in Figure (4.6) show the best fit to the data using equation (4.12). The SAXS curve of the micellar solution, which was prepared by dialysis (Fig. (4.6a)) differs significantly from the results of the solution prepared via evaporation of THF (Fig. (4.6b)). This indicates that the scattering contrast depends dramatically on the micellar morphology. From the fit for the dialyzed solution with a raspberry like morphology we obtain a mean micellar radius of 16 ± 8 nm. However, the size distribution of the micelles

is relatively broad as expected from the polydispersity of domains seen in the cryo-TEM micrographs (see Fig.(4.2)). Most likely, the scattering corresponds to the global size of the multicompartment micelle as the fluorinated domains are too dispersed within the micellar core. Thus, only an average over the whole hydrophobic core containing the PS and PVBFP blocks contribute to the scattering contrast. This result is also in good agreement with the cryo-TEM micrographs and with the size obtained by static light scattering. In contrast, for the solution prepared by evaporation of THF where we assumed a core-shell-corona morphology, the fit of the SAXS curve yields a mean radius of 6.0 ± 2.4 nm. This is obviously smaller than the overall radius of the micelle and corresponds most likely to the size of the fluorinated core. This radius and also the moderate size distribution of the radius corresponds to the spherical domains observed in the cryo-TEM micrographs (see Fig.(4.3)).

4.1.3 Conclusion

Combining the results from cryo-TEM, SLS and SAXS measurements, we can conclude that (*i*) the amphiphilic triblock copolymer PVBM-*b*-PS-*b*-PVBFP forms multicompartment micelles possessing a diameter of about 30 nm via self-assembly in aqueous medium and (*ii*) the micellar morphology depends greatly on the preparation method and the used solvents. As evidenced by cryo-TEM, the micelles prepared by dialysis from a water/dioxane mixture have a core, which exhibits a nano-segregated morphology consisting of many small fluorocarbon rich domains coexisting with a continuous hydrocarbon rich region. Micelles prepared by evaporation of THF from a water/THF mixture also have a multicompartment character but the structures exhibit a layered core-shell-corona morphology.

4.2 Linear ABCBA pentablock copolymer

4.2.1 Chemical characteristics

A novel linear ABCBA pentablock copolymer consisting of two hydrophilic poly(ethylene oxide) blocks (block A), two hydrophobic poly(γ-benzyl-L-glutamate) blocks (block B) and a hydrophobic perfluoropolyether block (block C) (PEO-*b*-P(BLG)-*b*-PFPE-*b*-P(BLG)-*b*-PEO) was prepared by a two-step reaction. First, the diblock copolymer poly(ethylene oxide)-*b*-poly(γ-benzyl-L-glutamate) was synthesized in *N,N*-dimethylformamide (DMF) by a ring-opening polymerization of the *N*-carboxy anhydride (NCA) of γ-benzyl-L-glutamate in the presence of an ammonium chloride-functionalized poly(ethylene oxide) macroinitiator ($\bar{M}_n = 5000$ g/mol; $\overline{DP} \sim 115$).[97] The molecular weight of the diblock copolymer PEO-*b*-P(BLG), $\bar{M}_n$, was found to be 6500 g/mol and the weight distribution was as narrow as the one of the macroinitiator ($\bar{M}_w/\bar{M}_n < 1.05$). The average degree of polymerization, $\overline{DP}$, of the P(BLG) block was calculated to be 8.[98] After the polymerization of γ-benzyl-L-glutamate the diblock copolymer should bear a NH_2 endgroup, which is essential for the second step of the pentablock preparation. However it is known that a P(BLG) primary amine end group can react with the last γ-benzyl-L-glutamate unit of the chain to form a stable five-membered lactam ring, making the chain inactive to the second step of the reaction.[99] In order to confirm its ω-amino chain-end functionality, PEO-*b*-P(BLG) was reacted with trinitrobenzene sulfonic acid (TNBSA) as an UV active endgroup label and subsequently analysed by size exclusion chromatography (SEC) - UV spectroscopy.[100] The results of this study indicated that 75% of the polymer chains possessed an ω-amino chain-end. In the second step the PEO-*b*-P(BLG) diblock was coupled with a perfluoropolyether (PFPE) ($\bar{M}_n \sim 3800$ g/mol measured by vapor presure osmometry) bearing a carboxylic acid group on both ends. The carboxyl-amine coupling reaction in DMF was mediated by *N,N'*-dicyclohexylcarbodiimide (DCC) and assisted by *N*-hydroxysuccinimide (NHS) to form covalent conjugates via amide bonds. The main problem of this coupling reaction involved finding a common solvent for dissolution of both the PEO-*b*-P(BLG) copolymer and the perfluoropolyether. This difficulty arise since PFPE is typically only soluble in fluorinated solvents, in which PEO-*b*-P(BLG) precipitates. However, due to their polar end-groups $\alpha-\omega$-dicarboxyl perfluoropolyethers behave as a surfactant in water or in polar aprotic solvents.[101] Thus, in polar solvents, an interfacial coupling reaction of PEO-*b*-P(BLG) and PFPE could be done at the surface of the preformed micelles of

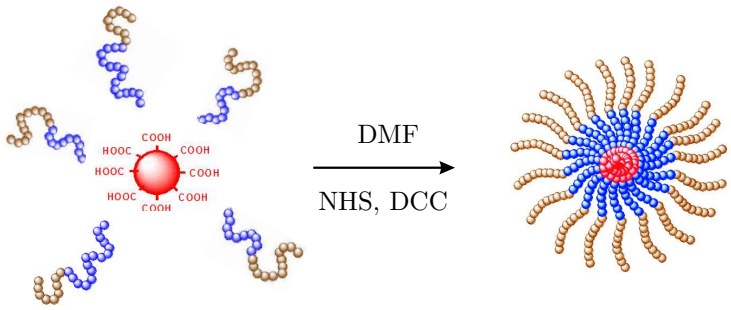

Figure 4.7: Schematic representation of the coupling reaction between PEO-*b*-P(BLG) and PFPE.

PFPE. Figure(4.7) shows a simplified sketch of this coupling reaction. In DMF, PFPE was found to form micelles spontaneously (studied polymer concentration was around 7 g/L) possessing an average diameter of approximately 15 nm, as evidenced by dynamic light scattering measurements. Therefore, these dilution conditions were used for the coupling reaction. The theoretical chemical structure of the synthesized pentablock copolymer PEO-*b*-P(BLG)-*b*-PFPE-*b*-P(BLG)-*b*-PEO is shown in Figure (4.8).

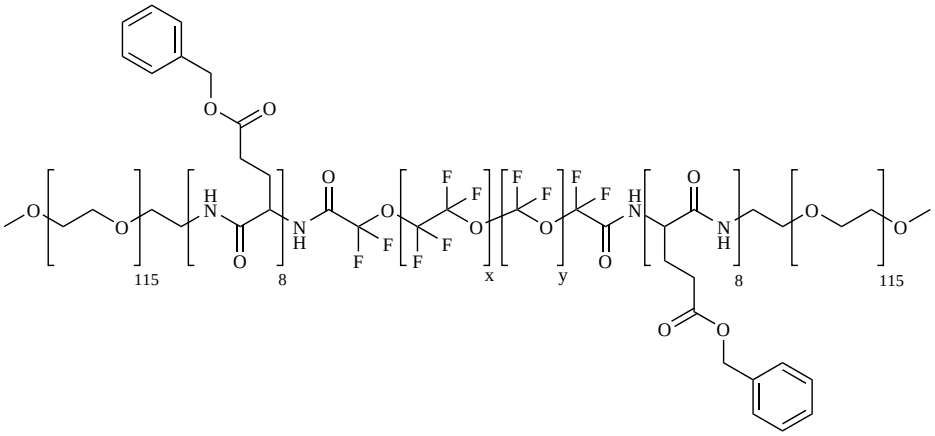

Figure 4.8: Theoretical chemical structure of the pentablock PEO-*b*-P(BLG)-*b*-PFPE-*b*-P(BLG)-*b*-PEO. (with x≫y)

Subsequently, the endproduct was transfered from DMF to water by stepwise dialysis against water-DMF mixtures with increasing volume of water. The water content of the dialysis solutions were 30%, 50%, 75% and finaly pure water. This leads to a clear aqueous solution, which was then freeze-dried. The molecular weight was calculated as a sum of two PEO-*b*-P(BLG) segments and one PFPE block to be 16800 g/mol. The pentablock could not be reliably studied by solvent-dependent analytical techniques such as solution

NMR or size exclusion chromatography because no universal solvent was found for dissolution of the three segments composing the resulting copolymer. The formed polymer is a surfactant in most solvents and therefore always self-assembles into nanostructures. Therefore, the final product was only characterized using solid-state analytic techniques such as elemental analysis and FT-IR spectroscopy. Elemental analysis yielded 51.9% carbon, 7.0% hydrogen, 8.2% fluoro, 2.1% nitrogen and 30.8% oxygen, which is in agreement with the theoretical values of 49.8% carbon, 6.6% hydrogen, 13.5% fluoro, 1.5% nitrogen and 28.6% oxygen. This proves that the diblock and the perflourinated block are in a ratio of 2:1 and that there is no loss during dialysis to water. The solid pentablock copoly-

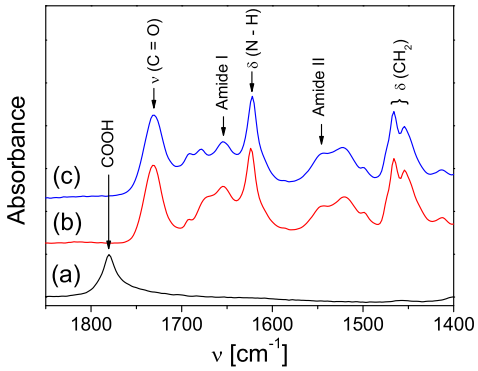

Figure 4.9: IR spectrum of PFPE (a), the diblock PEO-*b*-P(BLG) (b) and the pentablock PEO-*b*-P(BLG)-*b*-PFPE-*b*-P(BLG)-*b*-PEO (c).

mer was investigated by FT-IR spectroscopy in order to validate the bonding between the diblock, PEO-*b*-P(BLG), and the perfluorinated block, PFPE. Figure (4.9) shows the IR spectra of PEO-*b*-P(BLG), PFPE and the pentablock. In the spectrum of PFPE an intense carboxylic acid vibration band is present at 1780 cm^{-1}, while it is absent in the spectrum of the pentablock. From this we conclude, that, within experimental error, all the carboxylic acid functions of PFPE form a bond with the amino functions of the P(BLG) block. Usually, the carboxylic acid vibration band is at around 1710 cm^{-1} but, due to the CF_2 group in the vicinity of the carboxylic acid function, the vibration band is shifted to higher wavenumbers. The newly formed amide bond is only visible by small changes of the bands between 1700 - 1650 cm^{-1} because the vibration bands of the amide bond between PFPE and P(BLG) are almost identical to the peptide bonds of the P(BLG) block. The other vibration bands of the polymer chain are practically unchanged. Thus,

FT-IR and elemental analysis suggest that the coupling reaction between PEO-*b*-PBLG and PFPE proceeded smoothly. However, it is difficult to further characterize the resulting copolymers. For instance, it is not possible to affirm that the formed material is only composed of pentablock copolymers. Triblock copolymer PEO-*b*-PBLG-*b*-PFPE and possibly unreacted chains of PEO-*b*-PBLG may also be present in the final sample.

4.2.2 Association behavior in aqueous media

Prior to the transfer to aqueous media, the aggregation behavior in DMF was investigated by means of static and dynamic light scattering. Figure (4.10a) shows the Guinier-plot for the pentablock copolymer in DMF. The solid line represents a linear fit, which was used

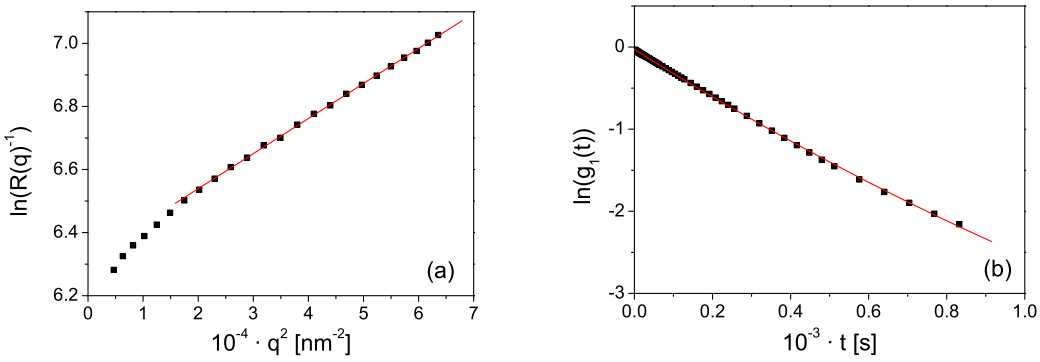

Figure 4.10: (a) Guinier-plot for the pentablock copolymer in DMF. (b) Field-correlation function, $g_1(t)$, for the pentablock in DMF. The solid lines represent a best fit to the data.

for the calculation of the radius of gyration. Thus, applying equation (4.11), the radius of gyration was calculated to be 58 ± 1 nm. The field-correlation function, $g_1(t)$, measured by DLS (Figure (4.10b)) was analysed by use of a cumulant expansion (eq.(3.15)). The apparent translational diffusion coefficient, D_{app}, was calculated from the first cumulant via equation (3.15) to be (3.7 ± 0.3) $\cdot 10^{-12}$ m^2/s. Applying the Stokes-Einstein equation (eq.(3.18)), this diffusion coefficient can be transformed into a hydrodynamic radius, R_h, of a corresponding sphere with the viscosity of DMF being $\eta = 0.82$ mPa·s at a temperature of 298 K. This yields a hydrodynamic radius of 72 ± 6 nm. The R_g/R_h ratio of 0.8 indicates the presence of spherical aggregates as a value of $\sqrt{3/5} \approx 0.775$, characteristic of a sphere.

Subsequently, the pentablock solution was transferred to water by step-wise dialysis,

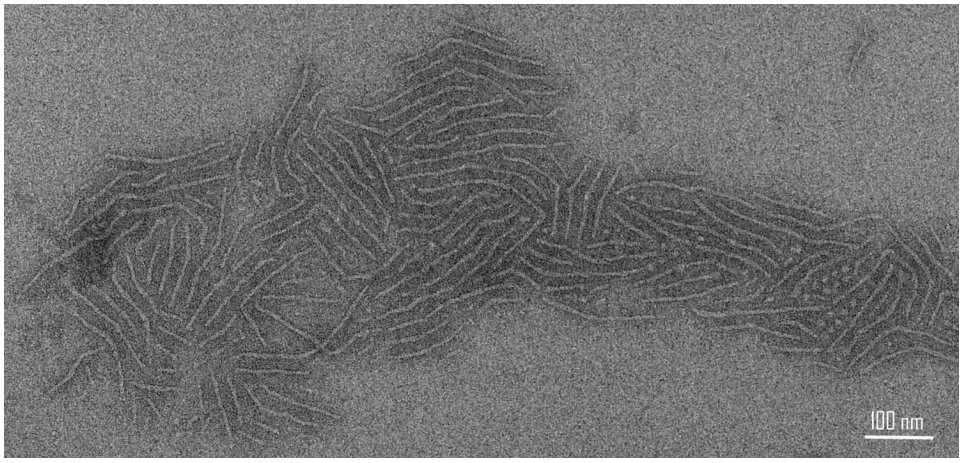

Figure 4.11: TEM micrograph of the pentablock copolymer in aqueous solution, negative stained with uranyl acetate.

as previously described. This may lead to a change of the nanostructure of the pentablock micelles. To determine the morphology of the micelles, we used electron microscopy. The TEM micrograph in Figure (4.11) is obtained for the aqueous micellar solution of the pentablock copolymer, negative stained with uranyl acetate. The image reveal the existence of worm-like micelles with length of about 100 to 200 nm and a core diameter of about 6 nm. Clearly visible also the dark gray region around the bright core, which can be attributed to the corona of the micelles. This contrast is due to a higher local concentration of the staining agent, which is probably due to a favored adsorption of the uranyl-ions on the corona of the micelles. Cryo-transmission electron microscopy of the aqueous micellar

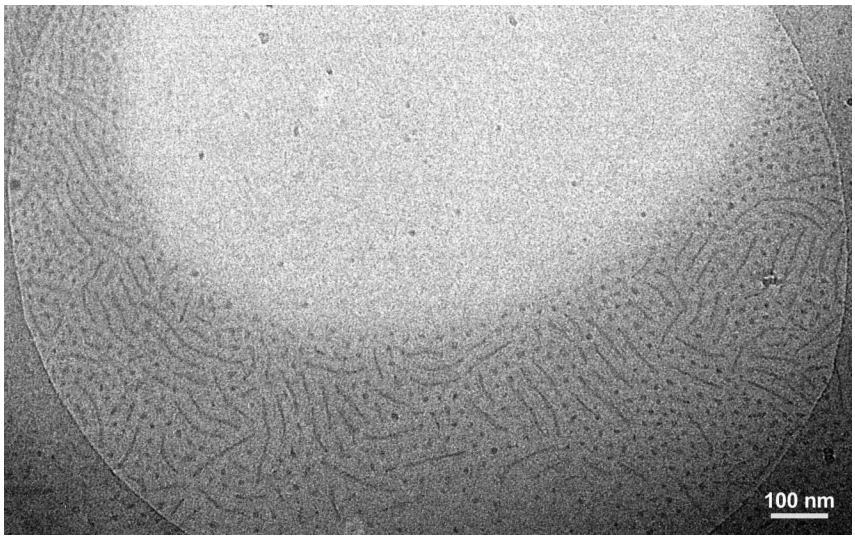

Figure 4.12: Cryo-TEM micrograph of the pentablock copolymer in aqueous solution.

solutions was then performed resulting in a typical micrograph shown in Figure (4.12). The image reveals uniformly dispersed circular and worm-like objects. The circular objects have a relatively narrow size distribution with an average diameter of 6-8 nm, whereas the worm-like objects possess a length of about 40-150 nm and a uniform thickness of 5-6 nm. The contrast of the micelles can be attributed to the presence of electron-rich fluorine atoms in the core. The water-soluble PEO corona and the hydrophobic peptide block of the micelles are not directly observable.

The overall diameter of the worm-like micelles and also of the circular objects can be estimated from the objects interdistance to be around 22-27 nm. From the micrograph we assume an onion-like core-shell-corona morphology. However, one cannot clearly distinguish whether there is a coexistence of spherical and worm-like micelles in the solution or whether the circular objects are the projection of worm-like micelles, which stand perpendicular to the image plane. To clarify this, sedimentation velocity measurements with a rotor speed of 20000 rpm were performed. The obtained distribution of the sedimentation

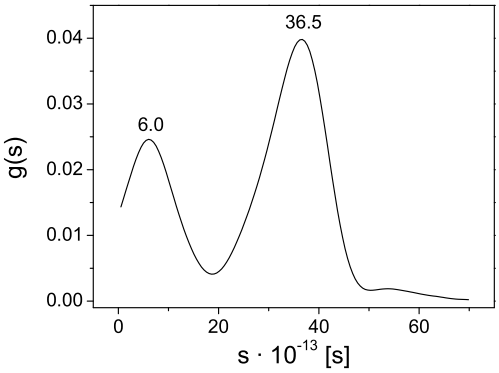

Figure 4.13: Distribution of the sedimentation coefficient of the pentablock copolymer in aqueous solution.

coefficient is presented in Figure (4.13). From the graph, it can be seen that there are two species in the solution, where one sediments much faster than the other. From this finding we conclude, that there is a coexistence of spherical and worm-like micelles in the aqueous solution of the pentablock copolymer. From the area under the peaks the mass ratio of spherical to worm-like micelles can be estimated to be about 1:2. This means that the number of spherical micelles in the solution is significantly higher than the number of worm-like micelles, as also seen on the cryo-TEM micrograph. The sedimentation co-

efficients are $6.0 \cdot 10^{-13}$ s for the spherical micelles and $36.5 \cdot 10^{-13}$ s for the worm-like micelles. The large distribution in the length of the worm-like micelles in the cryo-TEM micrograph is most likely due to projections where the objects are not parallelly aligned to the image plane.

A dynamic light scattering measurement was performed to determine the hydrodynamic radius of the aggregates. Figure (4.14) shows the measured field-correlation function. As there are two species in the solution, the cumulant fit method cannot be applica-

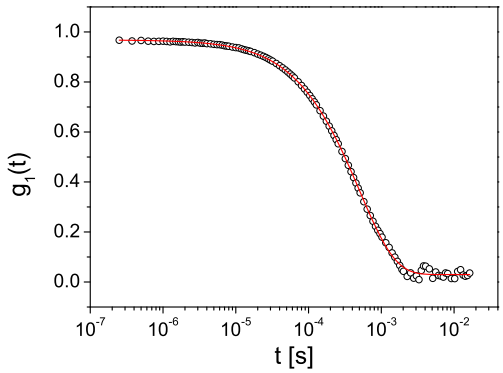

Figure 4.14: Field-correlation function $g_1(t)$ for the pentablock in aqueous solution. The solid line represents the best fit to the data.

ble. Therefore, the field-correlation function was fitted by a sum of a stretched exponential and an exponential function.

$$g_1(t) = c_0 + c_1 \cdot \exp(-(q^2 D_1 t)^x) + c_2 \cdot \exp(-(q^2 D_2 t)) \tag{4.16}$$

where c_0 is the base line, c_1, c_2 are the intensity fractions of the two species, and D_1, D_2 are the apparent translational diffusion coefficients of the two species.[102] The fit of the experimental data yield: $D_1 = (2.8 \pm 0.2) \cdot 10^{-12}$ m^2/s and $D_2 = (2.1 \pm 0.2) \cdot 10^{-11}$ m^2/s. As a result D_1 (slower diffusion) can be assigned to the diffusion of the worm-like micelles and D_2 (faster diffusion) to the diffusion of the spherical micelles. Further, the hydrodynamic radii, obtained via the Stokes-Einstein relation (eq.(3.18)), are found to be $R_1 = 88 \pm 6$ nm for the worm-like micelles and $R_2 = 12 \pm 1$ nm for the spherical micelles. These hydrodynamic radii are in good agreement with the micellar sizes estimated from the cryo-TEM micrograph.

The peptide block P(BLG) tends to form a secondary structure, which is stabilized by intra- or intermolecular hydrogen bridges. This can be an α-helix, a β-sheet or a random coil structure. The α-helix bears intramolecular hydrogen bridges between every fourth monomer unit of the peptide where ca. 3.6 monomer units are needed for one turn of the helix. Characteristic for the β-sheet, are the intermolecular hydrogen bridges between neighboring chains. The chains can have either a parallel or antiparallel arrangement. In contrast, the random coil structure has no stabilizing hydrogen bridges. For the development of stimuli responsive applications, an interesting feature of peptides is that the secondary structure can be switched by formation or dissociation of the hydrogen bridges for example by changes in pH. Thus, the secondary structure can be potential reversibly switched between an ordered and disordered state.

In order to determine the secondary structure of the P(BLG) blocks in the pentablock aggregates, a circular dichroism (CD) measurement was performed. Chiral molecules such as peptides show a different extinction coefficient for left and right circularly polarized light. Thus, after passing through the sample, the light is elliptically polarized and the ratio between the short to the long ellipse axis is called the ellipticity, Θ. This wavelength-dependent phenomenon has characteristic minima and maxima from which the secondary structure is distinguishable. The measured CD-spectrum of the pentablock solution (Figure (4.15)) displays the typical characteristics of an α-L-glutamic acid oligomer showing β-sheet conformation.[103] Interestingly the maximum ($\pi - \pi^*$ transition) and minimum ($n - \pi^*$ transition) of the CD-spectrum are slightly shifted to higher wavelength. We assume that this is due to intramolecular interactions of the benzyl side chains at the P(BLG)

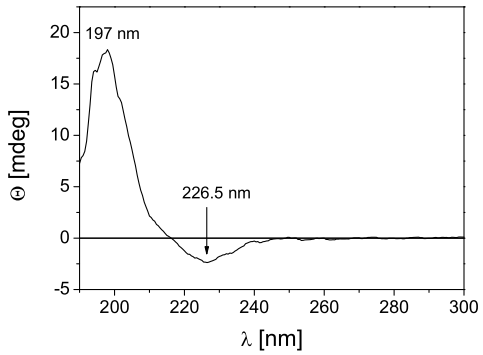

Figure 4.15: CD-spectrum of the pentablock copolymer in aqueous solution.

block. The CD-spectrum indicates that the P(BLG) block forms most likely a β-sheet inside the micellar shell. It is reported, that the thermodynamically stable conformation of poly(γ-benzyl-L-glutamate) homopolymer is an α-helix for a degree of polymerization (DP) > 10 and β-sheet for DP < 10 and DP > 4.[104, 105] Thus, since the P(BLG) block has a DP of 8, the conclusion of β-sheets as dominant conformation is in agreement with the recent literature.

From the size of the fluorinated core, estimated from the cryo-TEM micrograph, the average aggregation number of the spherical micelles was calculated. The molecular volume of the PFPE block was calculated as described in section (4.1.2) and is shown in Table (4.6).

Table 4.6: Calculated volumes for the PFPE segment in the copolymer (V_r = molar volume of the repeating unit, V_u = molecular volume of the repeating unit, N = average degree of polymerization, V = molecular volume of the segment in the copolymer).

Segment	V_r [cm^3/mol]	V_u [nm^3]	N	V [nm^3]
PFPE	55.36	0.092	30	2.76

The volume of the fluorinated core of the spherical micelles was calculated by

$$V_{c,s} = \frac{4\pi}{3}\left(\frac{D_c}{2}\right)^3 \tag{4.17}$$

using an average diameter $D_c = 7$ nm. The aggregation number, Z, can be determined by dividing the core volume, $V_{c,s}$, by the volume of one PFPE block, V_{PFPE}, which yields about 65 PFPE chains. For the worm-like micelles, the aggregation number was calculated exemplarily for a micellar length of 100 nm. The volume of the cylindrical core was calculated by

$$V_{c,c} = \frac{\pi}{4}(D_c)^2 \cdot L \tag{4.18}$$

with an average core diameter, D_c, of 6 nm. This calculation yields an aggregation number of about 1024. The thickness of the hydrophobic shell formed by the peptide block can be estimated from the length of the P(BLG) block. One γ-benzyl-L-glutamate unit has a length of about 0.24 nm, thus, the P(BLG) segment has a length of about 1.9 nm.

As the P(BLG) is in the β-sheet formation, the chain is almost completely stretched and, therefore, the thickness of the shell can be assumed to be equal to the calculated block length. Hence, by considering a hydrodynamic radius of 12 nm, the thickness of the outer PEO corona is calculated to be around 7 nm. Assuming a monomer segment length of 0.24 nm, this value corresponds to about 25% of the fully stretched PEO block, which is reasonable for a coiled conformation. Figure (4.16) shows a simplified sketch of the micellar morphology of the pentablock in aqueous solution. The assumed core-shell-corona structure is composed of a soft liquid-like core formed by the perfluoropolyether block. In contrast to the soft core, the surrounding shell is stiff and almost crystalline, as the P(BLG) block is in the β-sheet conformation. Finaly, the outer corona is coiled and swollen by water molecules.

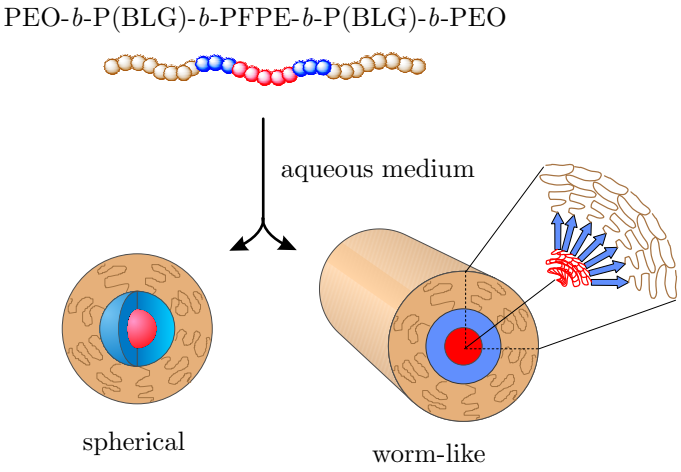

Figure 4.16: Schematic representation of the micellar morphology of the pentablock copolymer in aqueous solution. The core is formed by the perfluoropolyether (red) surrounded by the P(BLG) in β-sheet conformation (blue). The PEO in the corona (light brown) is coiled and swollen by water molecules.

4.2.3 Conclusion

Through the carboxyl-amine coupling reaction we were able to successfully synthesize a pentablock copolymer by combination of a perfluorinated homopolymer with two diblock copolymers. From our analytical results we can conclude that the pentablock forms spherical aggregates in DMF. When the copolymer solution is transfered to aqueous media, a mixture of coexisting spherical and worm-like micelles, probably having a core-shell-corona morphology are formed.

4.3 Self-assembly of an ABC triblock polymeric surfactant

4.3.1 Chemical characteristics

As previously mentioned in section (2.2.2), the basic requirement of a multicompartment micelle is the existence of two non-compatible hydrophobic segments bound to a hydrophilic segment. Preferably, fluorocarbon and hydrocarbon chains are used as the two immiscible hydrophobic blocks. In this study we focused on an ABC analogous polymer structure of a polymeric surfactant having a hydrophilic block end-tagged with a hydrocarbon and a fluorocarbon moiety of defined lengths. The synthesis of the am-

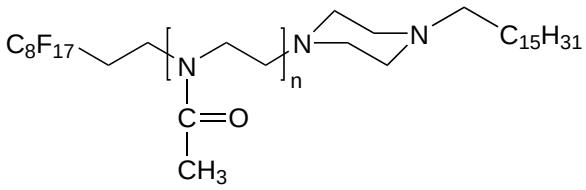

Figure 4.17: Chemical structure of poly(2-methyl-2-oxazoline) end-capped with a fluorocarbon and a hydrocarbon chain.

phiphilic telechelic poly(2-methyl-2-oxazoline) having hydrocarbon and fluorocarbon endblocks was performed by living cationic polymerization. As initiator for the polymerization of 2-methyl-2-oxazoline, trifluoromethanesulfonic acid-1-ethylperfluorocetyl ester was used, which also introduced the fluorinated segment ($C_8F_{17}CH_2CH_2$). The polymerization was then terminated by the addition of *N*-hexadecylpiperazine, which introduced the hydrocarbon endblock. A detailed description of the synthetic approach adopted by Weberskirch and co-workers is cited in literature.[79] Table (4.7), presents the degrees of

Table 4.7: Polymer characteristics of the samples investigated in the present study

sample-ID	n*	M_n [g/mol]*	M_w/M_n**
PS1	35	3700	1.20
PS2	57	5600	1.10
PS3	72	6900	1.40

* determined by ^{1}H NMR; ** determined by SEC

polymerization, molecular weights and polydispersities corresponding to the three investigated ABC triblock polymeric surfactants.

4.3.2 Physical properties of the micellar solution

Direct dissolution of the polymers in water, a selective solvent for the middle block, results in a colorless (slightly yellowish at high concentrations), clear micellar solution. An alternative way is to dissolve the polymers molecularly in a solvent mixture of water/acetone (1:1) and subsequently evaporate the acetone at 50 °C. An experimental comparison shows that both preparation methods leads to the same micellar solution and therefore for practical reasons the direct dissolution was preferred. The dynamic surface tension was determined at room temperature by means of the pendant drop method. Figure (4.18 a) shows exemplarily the curve of the dynamic surface tension for PS2 with a concentration of $5 \cdot 10^{-3}$ mmol/L. As one can see, the surface tension deceases and reaches an equilibrium after about 10^4 s.

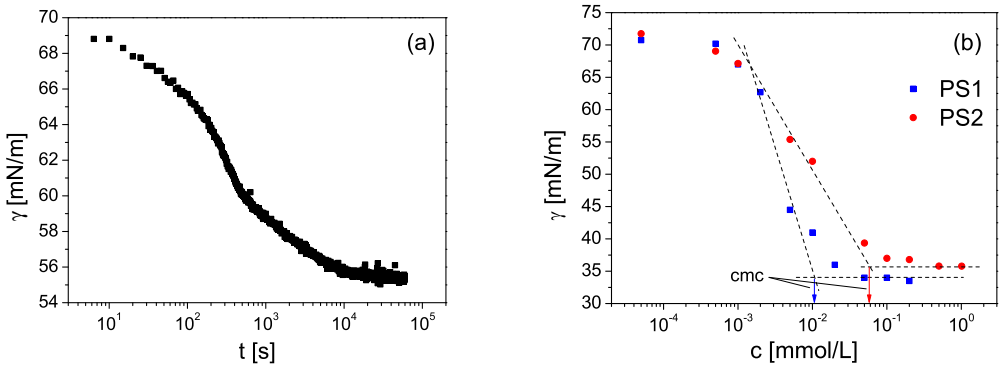

Figure 4.18: a) Dynamic surface tension of PS2 ($c = 5 \cdot 10^{-3}$ mmol/L); b) Equilibrium surface tension isotherms.

The change in surface tension is due to the diffusion and reorientation of adsorbed molecules at the surface as well as transport processes between solution and surface. Since the diffusion of polymeric macromolecules is slow compared to low molecular weight surfactants, the equilibration of the surface tension can require several hours. The different slopes in the curve of the dynamic surface tension indicate several kinetic processes during surface formation.

Figure (4.18 b) presents the concentration dependence of the equilibrium surface ten-

sion of polymer PS1 and PS2. From the intersection of the tangents of the lower plateau and the inflection point of the surface tension isotherm, the critical micellization concentration (cmc) can be determined. The cmc values obtained from the surface tension isotherms increase from 0.01 mmol/L for PS1 to 0.06 mmol/L for PS2. This can be explained by the increased length of the hydrophilic poly(2-methyl-2-oxazoline) block from 35 units for PS1 to 57 units for PS2, which increases the water solubility of the whole polymeric surfactant and therefore the concentration for micellization. The slope of the surface tension isotherm is a measure for the occupied area per molecule at the air-water interface. For PS2 the slope is less steep than for PS1, which indicates a larger area per molecule for PS2 as one would expect from the molecular structure. A calculation of the area was not meaningful as the theories always consider ideal low molecular weight surfactants as model compounds, not assignable to polymers.

The cmc region is relatively broad compared to low molecular weight surfactants, which indicates that the micellization is less associative and that the aggregation number increases slowly with concentration. Noteworthy is also the low surface tension of about 35 mN/m at higher concentrations, which shows that the hydrophobic chains are densely packed at the air-water interface. Although a micro phase separation of hydrocarbon and fluorocarbon rich domains is probable, unfortunately this cannot be experimentally detected.

The specific volumes of the micelles were determined by measuring the density of the micellar solutions at different concentrations and at a temperature of 20 °C. The values are practically equal for all three polymers (about 0.8 cm^3/g), which indicates that with increasing mass of the polymers and thus of the micelles (assuming a similar aggregation number for each polymer) the volume of the micelles increases at the same rate keeping the specific volume constant. This additional volume is due to the longer hydrophilic block, which forms the outer corona of the micelle.

Determination of the intrinsic viscosity, $[\eta]$, which is a measure of the hydrodynamic volume, supports this assumption. The viscosity measurements were done at 25 °C with a capillary viscometer of the Ubbelohde type. Figure (4.19) shows the so-called Huggins plots, where the reduced viscosity, η_{sp}/c, is plotted *versus* the polymer concentration, c. According to equation (3.49), the intrinsic viscosity can be determined for small concentrations by extrapolating the experimental data to zero concentration. With increasing chain length of the middle block from PS1 to PS3, the intrinsic viscosity increases from 5.3

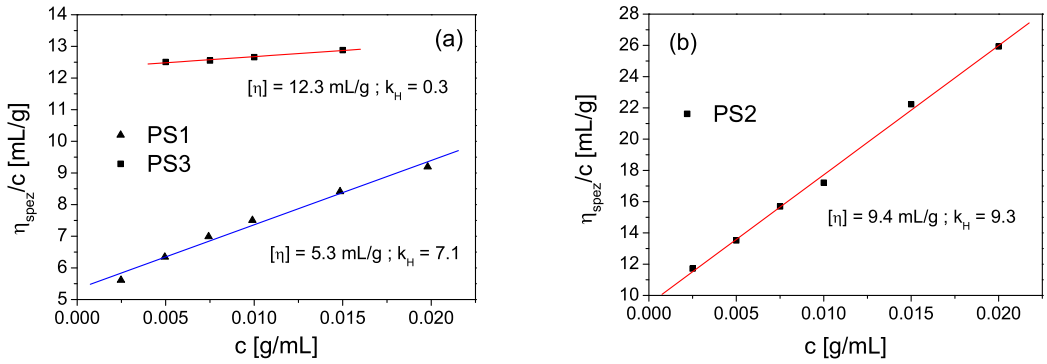

Figure 4.19: a) Huggins plot of PS1 and PS3; b) Huggins plot of PS2.

Table 4.8: Physical characteristics of the investigated micellar solutions

sample-ID	cmc [mmol/L]	$\bar{v}$ [cm^3/g]	$[\eta]$ [mL/g]	k_H
PS1	0.01	0.792 ($\pm 3 \cdot 10^{-3}$)	5.3	7.1
PS2	0.06	0.793 ($\pm 1 \cdot 10^{-3}$)	9.4	9.3
PS3	0.10	0.7999 ($\pm 4 \cdot 10^{-4}$)	12.3	0.3

mL/g for PS1 to 12.3 mL/g for PS3. Table (4.8) summarizes the physical characteristics of the investigated micellar solutions.

The molecular structure of the poly(2-methyl-2-oxazoline) end-capped with a fluorocarbon and a hydrocarbon chain is comparable to an amphiphilic ABA block copolymer with a hydrophilic middle block. In such systems so-called tentacled micelles and, at higher polymer concentrations, micellar networks were observed.[106] The formation of a network is, for example, indicated by a steep non-linear increase in viscosity. For the investigated polymeric surfactant system, the aggregation behavior shows a clear transition from single molecules to micellar aggregates above a critical concentration and no indication of the formation of polymeric networks up to concentrations of 0.01 mol/L.

The demicellization process, which is the reverse process of micelle formation, was followed by isothermal titration calorimetry (ITC). A typical experimental titration curve obtained from dilution of a micellar PS3 solution with initial concentration of 0.29 mmol/L in 1.442 mL water at 25°C is shown in Figure (4.20 a). The enthalpogram shows the heat

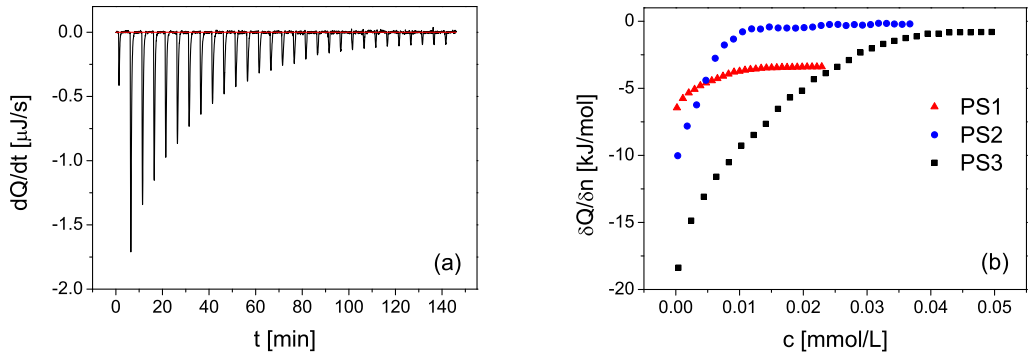

Figure 4.20: a) Experimental titration curve obtained from injecting PS3 (10 μL aliquots) of 0.29 mmol/L into water (1.442 mL) at 25°C with subtracted baseline.; b) Integrated heat per injection, δQ, normalized with respect to the injected number of moles, δn, vs the total concentration in the sample cell.

flow caused by the consecutive injections of 10 μL aliquots of micellar solution into water. For the first injections, the concentrations in the sample cell are below the cmc; hence, the large exothermic effects observed are due to the demicellization process and dilution of the resultant molecularly dissolved polymer chains. The sharp increase in the reaction enthalpy in the curve indicates that the cmc in the sample cell has been reached and the micelles are no longer dissolved; the only heat that is measured is caused by dilution of micelles. Integration of the heat flow peaks yields the heat of each injection shown in Figure (4.20 b) for all three polymers. Due to possible dilution during the equilibration time preceding the measurement, the first injection was ignored in the analysis of the data.

The cmc and the enthalpy of demicellization cannot be determined accurately from the graph as the transition range is very broad and the concentration region where the micelles are completely dissolved could not be reached. Using much lower initial concentrations for the ITC measurement, led to a decrease of the signal to noise ratio, and the demicellization process was not clearly detectable. The concentration range of the transition, which is generally assigned to the cmc, is smaller and significantly shifted to lower concentrations than for the surface tension measurements. Also, as also shown by the surface tension measurements (Fig. (4.18)), micelle formation is a rather slow process, taking about 3 hours to equilibrate, and spreading over a broad concentration range of two orders of magnitude. From this, we conclude that the observed process in the comparatively fast

ITC measurements is most likely not the complete demicellization but rather a change of the micellar structure connected to this process. Therefore, it seems plausible to assume that we do not measure the heat of the complete dissolution of the micelles, which is probably a three or multi-step process. For example, it is possible that the hydrocarbon domains dissolve first in a fast process, producing the observed heat. This may be followed by a second process, the dissolution of the fluorocarbon domains, which is much slower and a lower heat flow making it non-detectable by ITC. Such multi-step dissolution processes can be accompanied by a shape transition, e.g., from cylindrical to spherical micelles, as it has been reported for heptaethylenglycoltetradecylether ($C_{14}EO_7$) by Herrklotz *et.al.*.[107] In particular, ionic surfactants have been found to show a three-step behavior forming spherical micelles at the cmc, which then grow cooperatively to rod-like micelles at the "second cmc" at higher concentrations.[108]

The vertical shift of the curve of PS1 is due to dilution of the solution in the sample cell. This enthalpy of mixing is normally quite small compared to the signal of the demicellization process and can be neglected. In the case of the PS1 solution, the initial concentration was very small in order to reach the cmc region. Therefore, the signals of both processes became comparable, which was not taken into account for the integration of the heat flow.

It has been found that the formation of micelles is connected with a negative change in the Gibbs energy, ΔG.[109] According to the Gibbs-Helmholtz equation the change in Gibbs energy can be separated into a change of enthalpy, ΔH, and entropy, ΔS.

$$\Delta G = \Delta H - T \cdot \Delta S \tag{4.19}$$

For all three polymer solutions, the demicellization is exothermic, consequently the micellization is endothermic, thus resulting in a positive change of the enthalpy, ΔH. Therefore, the negative change in Gibbs energy results from a positive entropy change. The large gain of entropy is thought to have two possible origins. First, the water molecules in hydration shells around a hydrophobic chain are released during micellization, and second, an increased freedom of the hydrophobic chains results when the polymer is transferred from an aqueous to a non-polar environment.[110]

It can be seen that the micelle formation enthalpy at a temperature of 25 °C increases with increasing length of the B block ($\Delta H_{PS1} < \Delta H_{PS2} < \Delta H_{PS3}$). Due to the fact

that no constant heat values at low concentrations are present, no exact value for ΔH can be determined. Nevertheless, the measured heat values are close to the enthalpy of micellization of low molecular weight surfactants such as reported for alkyl sulfates,[111] indicating that the alkyl chains dissolve first and dominate the process.

4.3.3 Influence of the hydrophilic block length on the micellar structure

The latter section was concerned with the general properties of the micellar solution such as cmc and viscosity in dependence of the hydrophilic block length. However, the properties of the micelles like size and shape has not been discussed so far. For this purpose we performed small angle X-ray scattering measurements. Figure (4.21) shows the obtained scattering curves for all three solutions. A slope of q^{-1}, which is characteristic for a cylindrical shape, is indicated in the graph. From this, it is obvious that the micelles have

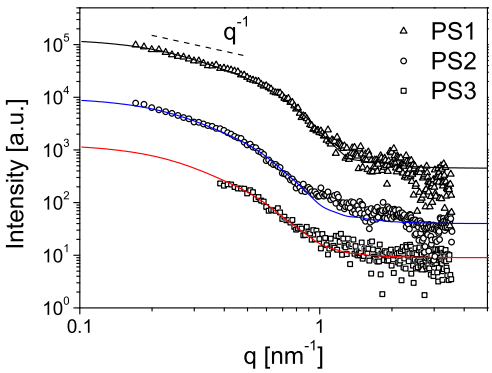

Figure 4.21: Small-angle X-ray scattering curves obtained for a micellar solution of PS1 (50 g/L)), PS2 (43 g/L) and PS3 (85g/L). The solid lines represent the fits to the experimental data using a cylindrical model with a polydisperse radius.

a cylindrical shape. The experimental SAXS data was fitted by a scattering curve for a system of homogeneous cylindrical particles with length, L, and radius, R. The scattered intensity, $I(q)$, is given by equation (4.12) with the form factor of a homogeneous cylinder, which can be factorized for long cylinders

$$P(L,R,q) = F^2(L,R,q) = F_{\parallel}^2(L,q)\left\langle F_{\perp}^2(R,q)\right\rangle \tag{4.20}$$

where $F_{\parallel}(L,q)$ is the orientationally averaged longitudinal contribution of the scattering amplitude and $F_{\perp}(R,q)$ is the cross-sectional part of the scattering amplitude.[112] The square of the longitudinal scattering amplitude is given by

$$F_{\parallel}^2(L,q) = \frac{2}{qL}\int_0^{qL}\frac{\sin(t)}{t}\,dt - \left(\frac{\sin(qL/2)}{qL/2}\right)^2 \tag{4.21}$$

The square of the cross-sectional scattering amplitude of a homogeneous cylinder averaged for a Schulz-Zimm distribution of R (eq.(4.14)) is given by

$$\left\langle F_{\perp}^2(R,q)\right\rangle = {}_3F_2\left[\frac{3}{2},\frac{(z+1)}{2},\frac{(z+2)}{2},2,3;-4q^2R_z^2\right] \tag{4.22}$$

where z is the width of the distribution, $R_z = \bar{R}/(z+1)$ and ${}_3F_2\left[a_1,a_2,a_3,b_1,b_2;x\right]$ is the hypergeometric function, which can be written in terms of series expansions

$${}_3F_2\left[a_1,a_2,a_3,b_1,b_2;x\right] = \sum_{n=0}^{\infty}\frac{(a_1)_n(a_2)_n(a_3)_n\,x^n}{(b_1)_n(b_2)_n\,n!} \tag{4.23}$$

where $(c)_n$ are the Pochhammer factorials given by

$$(c)_n = \frac{\Gamma(c+n)}{\Gamma(c)} = c(c+1)(c+2)\ldots(c+n-1) \tag{4.24}$$

where $\Gamma(x)$ is the Gamma function. The polydispersity was considered only for the radius of the cylinder, as the influence on the scattering curve is more pronounced for the radius than for the length. The solid curves in figure (4.21) show the best fit to the data. The scattering curves are in agreement with the scattering resulting from thin cylinders with a length of 20 nm and radii of 3.0 nm, 3.8 nm and 4.0 nm for PS1, PS2 and PS3, respectively. It must be said that the length of the cylinders are assumed, because the scattering curves were experimentally accessible only down to $q = 0.2$ nm^{-1}, which does not allow the calculation of sizes larger than 30 nm. The parameters for the fits are summarized in Table (4.9).

To confirm the micellar size obtained by small angle X-ray scattering, we performed dynamic light scattering measurements. Figure (4.22) shows the field-correlation functions, $g_1(t)$, for all three micellar solutions measured by DLS. The correlation functions were

Table 4.9: Parameters for the fit of the small angle X-ray scattering curves. The standard deviation is given by $\sigma_R = \bar{R}/(z+1)^{1/2}$. L = assumed length of the cylindrical micelle

sample-ID	R [nm]	σ_R [nm]	L [nm]
PS1	3.0	0.5	20
PS2	3.8	0.8	20
PS3	4.0	1.0	20

analysed by use of a cumulant expansion (eq.(3.15)). The apparent translational diffusion coefficient, D_{app}, was calculated from the first cumulant via equation (3.16), with $q^2 = 6.96 \cdot 10^{-4}$ nm^{-2}, to be $(4.50 \pm 0.04) \cdot 10^{-11}$ m^2/s, $(4.25 \pm 0.06) \cdot 10^{-11}$ m^2/s and $(2.29 \pm 0.06) \cdot 10^{-11}$ m^2/s for PS1, PS2 and PS3 respectively. The diffusion coefficient is termed "apparent" as only one concentration at a fixed scattering angle ($2\theta = 173°$) was measured.

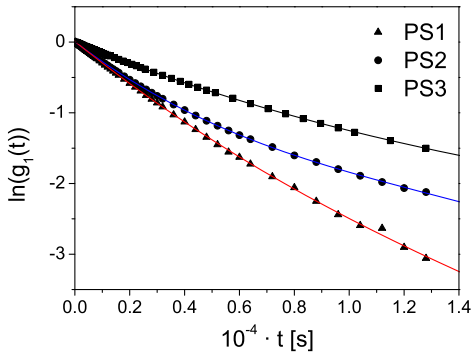

Figure 4.22: Field-correlation functions, $g_1(t)$, for all three micellar solutions measured by DLS. The solid lines represent the cumulant fits to the data.

According to Einstein, the diffusion coefficient, D, and the frictional coefficient, C, are linked by a fundamental relationship, that is

$$D = \frac{k_B T}{C} \tag{4.25}$$

where k_B is Boltzmann's constant and T, the absolute temperature. For rod-like particles, with a length, L, and radius, R, the frictional coefficient, C, is given by[113]

$$C = \frac{3\pi\eta\, L}{\ln(L/2R) + \gamma} \tag{4.26}$$

where γ is a function of L and R, which can be approximated[113] in the range $1 < L/R < 10$ by

$$\gamma(L,R) = 0.312 \;+\; 1.122 \cdot \frac{R}{L} \;+\; 0.4 \cdot \left(\frac{R}{L}\right)^2 \tag{4.27}$$

Thus, by combining equation (4.25) and (4.26), the diffusion coefficient can be applied to calculate the dimensions of the micelles. For the estimation of the length of the micelles, we used the corresponding micellar radius obtained by the SAXS measurements as first approximation with the viscosity of water being $\eta = 0.887$ mPa·s at a temperature of 298 K. This yields a length of 18 nm, 20 nm and 36 nm for PS1, PS2 and PS3, respectively showing that our assumed lengths for the fit of the SAXS measurements are in agreement with these results.

Analytical ultracentrifugation (AUC) measurements were used to determine micellar weights and aggregation numbers of the polymer micelles. Figure (4.23 a) shows exemplarily a part of the raw data of a sedimentation velocity run of a micellar solution of PS3 with a concentration of 6 g/L at a rotor speed of 50000 rounds per minute. Although the velocity of individual micelles cannot be resolved, the rate of movement of the sedimenting boundary can be measured. Plotting the logarithm of the radial position of the sediment-

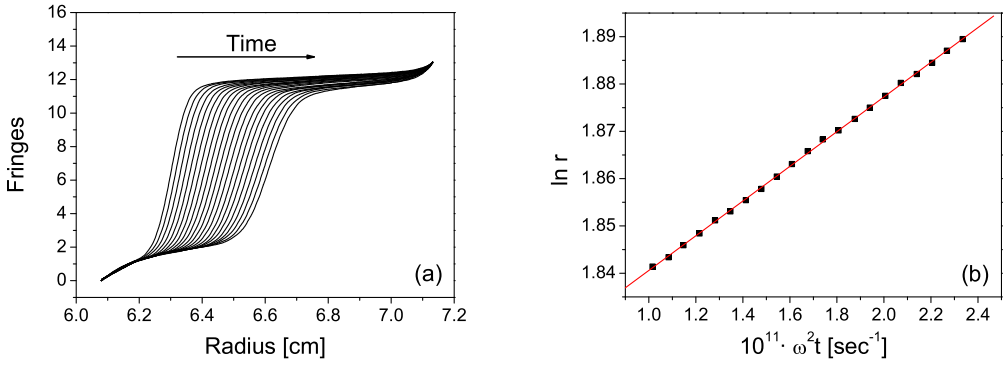

Figure 4.23: a) Experimental curves of the sedimenting boundary for a micellar PS3-solution (6 g/L) at 50 000 rpm.; b) Plot of the logarithm of the radial position of the sedimenting boundary as a function of $\omega^2 t$. The slope yields the mean sedimentation coefficient $s = 3.67 \cdot 10^{-13}$s.

ing boundary as a function of $\omega^2 t$ gives a linear curve and, according to equation (3.34), yields the mean sedimentation coefficient, s, as the slope of the curve (Figure (4.23 b)). This coefficient depends directly on the mass of the micelles and inversely on the frictional coefficient, which is a measure of the effective size. The concentration dependence of the sedimentation coefficient of all three micellar solutions is shown in Figure (4.24). The experimental data was fitted to equation (3.36) where s_0 is the sedimentation coefficient at the cmc. The results are summarized in Table(4.10). As the mass of the micelles does

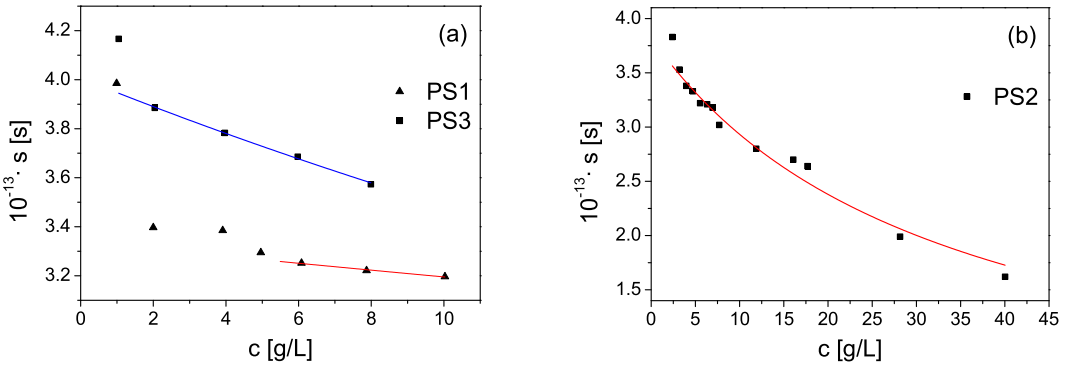

Figure 4.24: Concentration dependence of the sedimentation coefficient for: a) PS1 and PS3; b) PS2.

not decrease with increasing concentration the frictional coefficient must increase with increasing concentration, causing a decrease of the sedimentation coefficient. This change of the frictional coefficient is due to the concentration dependence of the viscosity of the solution. The comparison of the three sedimentation coefficients, s_0, shows an increase with increasing hydrophilic block length, which can be due to an increased mass of the micelles or due to a decreased friction caused by a change of the micellar shape. The concentration

Table 4.10: Extrapolated sedimentation coefficients of the investigated micellar solutions.

sample-ID	s_0 [10^{-13}s]	k_s
PS1	3.3	4.5
PS2	3.8	30.3
PS3	4.0	15.0

dependence of the sedimentation coefficient of the PS2 sample is more pronounced than that of the other two samples, but this can also be explained by the stronger concentration dependence of the viscosity (see Figure (4.19)). Unfortunately, we were not able to determine the geometry of the micelles directly from the AUC measurements through, for example, the Wales/van Holde ratios.[66] This is, in principle, possible, but such calculations are based on a number of assumptions and valid only for selected polymers as proved first by Creeth and Knight.[67]

Noteworthy is also the steep increase of the sedimentation coefficient at low concentrations. The measurement of the molar mass by a sedimentation equilibrium experiment in this concentration range shows that the molar mass increases with concentration. Figure (4.25)) shows exemplarily the concentration dependence of the apparent weight-averaged molar weight of the PS1 micelles. This indicates that (*i*) the micelle formation is an open association process i.e. a step-by-step growth and (*ii*) the frictional coefficient changes dramatically, which implies that the shape most likely changes from spherical to a more elongated rod-like shape as the change in solution viscosity is rather small. This is also in agreement with the surface tension measurement where a broad cmc region is observed.

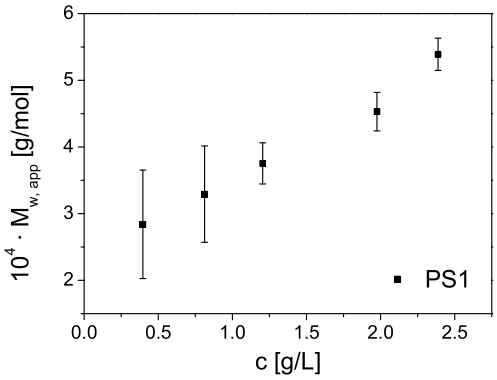

Figure 4.25: Concentration dependence of the apparent weight-averaged molar weight of the micelles of PS1.

From the shape of a sedimenting boundary in a sedimentation velocity experiment, the distribution of the sedimentation coefficient can be calculated by using equation (3.37). However, the boundary is not only spreaded due to polydispersity of the sedimenting species but also due to diffusion. However the effect of diffusion becomes vanishingly small with time since spreading of the boundary due to diffusion is proportional to $t^{1/2}$,

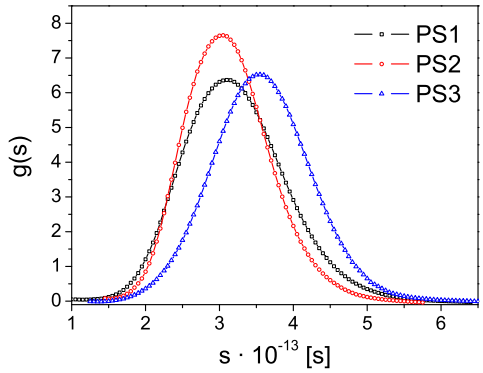

Figure 4.26: Distributions of the sedimentation coefficient of all three micellar solutions. (PS1: 6.1 g/L; PS2: 6.3 g/L; PS3: 6.0 g/L)

whereas the separation of macromolecules or colloids of differing sedimentation coefficients (polydispersity) is proportional to t.[65] Figure (4.26) shows the distributions of the sedimentation coefficients of all three micellar solutions. The distributions were fitted with a Schulz-Zimm distribution and from their width the root mean square deviation from the mean sedimentation coefficient was calculated to be around $0.7 \cdot 10^{-13}$ s for all three samples.

The apparent molecular weight of the micelles was calculated from the sedimentation velocity experiment via the so-called Svedberg equation.

$$M = \frac{s_0 N_A k_B T}{D(1 - \bar{v}\rho_0)} \tag{4.28}$$

The calculated values for the apparent molecular weights are shown in Table (4.11). The aggregation number, Z, of the micelles was calculated by dividing the apparent molecular weight of the micelles by the molecular weight of the single polymer chain. As expected, the weight of the micelles increases with increasing length of the hydrophilic block. Table (4.11) summarizes the results obtained by SAXS, DLS and AUC.

Figure (4.27) shows a simplified sketch of the self-assembly in aqueous media. The polymer chains form cylindrical micelles with a nano-segregated core. The water-soluble middle block, constituting the corona, forms most likely a loop whereas the flexible hydrophilic hydrocarbon chain segment and the comparatively stiff fluorocarbon chain are forming the core.

Table 4.11: Physical characteristics of the investigated micellar solutions obtained by SAXS, DLS and AUC.

sample-ID	R [nm]	L [nm]	D_{app} [10^{-11} m^2/s]	s_0 [10^{-13} s]	M_{app} [g/mol]	Z
PS1	3.0 ± 0.5	∼ 18	4.50 ± 0.04	3.3 ± 0.7	86800	23
PS2	3.8 ± 0.8	∼ 20	4.25 ± 0.06	3.8 ± 0.7	108000	19
PS3	4.0 ± 1.0	∼ 36	2.29 ± 0.06	4.0 ± 0.7	216000	31

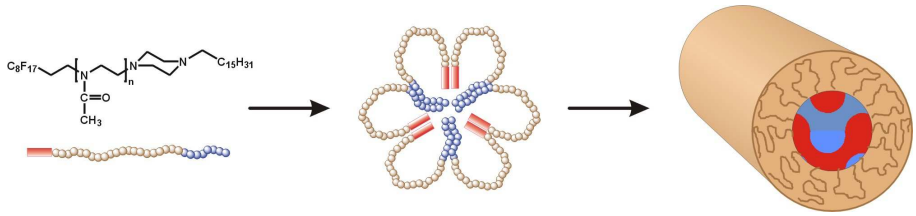

Figure 4.27: Simplified sketch of the self-assembly of polymer chains to cylindrical micelles with a hydrophilic shell (light brown) and a core with fluorocarbon-rich domains (red) and hydrocarbon-rich domains (blue) in aqueous media.

4.3.4 Solubilization of 1,4-Diiodoperfluorobutane

For the solubilization experiment, the polymers PS2 and PS3 were dissolved in a solvent mixture water/acetone (1:1) and an equimolar amount of 1,4-diiodoperfluorobutane dissolved in acetone was added. The solutions were then stirred at 50 °C to evaporate the acetone. An incorporation of this low molecular weight compound into PS1 even at lower mixing ratios was not successful as the micellar structure is probably too compact and can therefore not solubilize 1,4-diiodoperfluorobutane.

In order to investigate the changes of the micellar characteristics in solution due to the solubilization, we performed small angle X-ray scattering (SAXS) measurements. Figure (4.28) presents the SAXS curves of PS2-loaded and PS3-loaded. The scattering of the doped micelles is in agreement with the scattering resulting from cylindrical core-shell micelles.

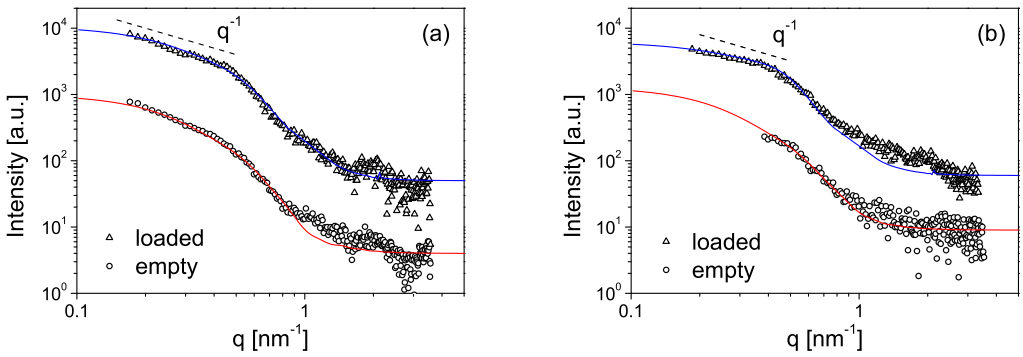

Figure 4.28: Small-angle X-ray scattering curves obtained for a aqueous solution of a) PS2-loaded (75 g/L)) b) PS3-loaded (48 g/L). For comparison, the scattering curves of the unfilled micelles are also shown. The solid lines represent the fits to the experimental data.

The particle form factor, $P(L, R, q)$, is practically similar to the unfilled case except in the cross-sectional scattering amplitude, which is given by[112]

$$F_{\perp}(R_c, R_m, q) = \left[(1-\rho)\,{}_0F_1\left[2; -\frac{q^2R_c^2}{4}\right] + \rho p^{-2}\,{}_0F_1\left[2; -\frac{q^2R_m^2}{4}\right]\right] \cdot [1-\rho(1-p^{-2})]^{-1} \tag{4.29}$$

where R_c, R_m are the core and the micellar radius, respectively, ρ is the electron density ratio between shell and core and $p = R_c/R_m$. Thus, due to the incorporated 1,4-diiodoperfluorobutane the electron density contrast between the core and the shell becomes large enough so that it can be detected by SAXS. For PS2-loaded, the fit of the experimental data yields an effective micellar radius of 5.0 nm, an inner radius of 4.5 nm and a shell/core electron density ratio of $\rho = 0.08$. The scattering of PS3-loaded was fitted by the scattering of a core-shell cylinder with an effective micellar radius of 6.0 nm, an inner radius of 5.0 nm and a shell/core electron density ratio of $\rho = 0.15$. For the fit of the experimental data, the length of the loaded micelles was selected to be identical to the empty case. The reason for this is that a change of the length mainly has an influence on the small q region of the scattering curve where the experimental data is limited. Both micellar solutions display a similar width of their size distribution with $\sigma_R = 1.8$ nm for PS2-loaded and $\sigma_R = 2.1$ nm for PS3-loaded.

To estimate the length of the micelles, we determined the translational diffusion coeffi-

cient by dynamic light scattering measurements. Figure (4.29) shows the field-correlation functions, $g_1(t)$, for the doped micellar solutions. The correlation functions were analysed with respect to the empty micellar solutions. The apparent translational diffusion coefficient, D_{app}, was calculated to be $(1.2 \pm 0.1) \cdot 10^{-11}$ m^2/s for PS2-loaded and $(1.3 \pm 0.1) \cdot 10^{-11}$ m^2/s for PS3-loaded.

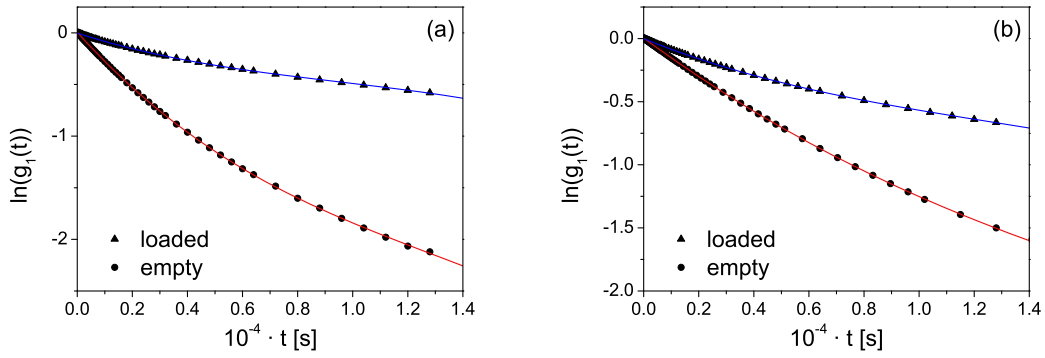

Figure 4.29: Field-correlation functions, $g_1(t)$, for a) PS2-loaded and b) PS3-loaded. For comparison, the curves of the empty micelles are also shown. The solid lines represent the cumulant fits to the experimental data.

In comparison, the diffusion coefficients of the loaded micelles are significantly lower than for the empty case. This was expected as the particle size is increased due to the incorporation of the low molecular weight compound. The length of the cylindrical micelles was calculated from the diffusion coefficient by using equations (4.25) and (4.26), which yields about 43 nm for PS2-loaded and 65 nm for PS3-loaded. A reason for this increased length compared to the unloaded micelles may be a higher stability of the core due to the presence of dopant. Table (4.12) summarizes the micellar characteristics of the doped micelles obtained by SAXS and DLS.

Table 4.12: Micellar characteristics of the doped solutions obtained by SAXS and DLS.

sample-ID	R_c [nm]	R_{eff} [nm]	L [nm]	D_{app} [10^{-11} m^2/s]
PS2-loaded	4.5 ± 1.6	5.0 ± 1.8	~ 43	1.2 ± 0.1
PS3-loaded	5.0 ± 1.8	6.0 ± 2.1	~ 65	1.3 ± 0.1

To determine the apparent molecular weight of the doped micelles we performed sedimentation velocity experiments at a rotation rate of 50000 min^{-1}. The sedimentation constants were calculated from plots of the logarithm of the radial positions of the sedimentation boundary as a function of $\omega^2 t$. Figure (4.30 a) shows the concentration de-

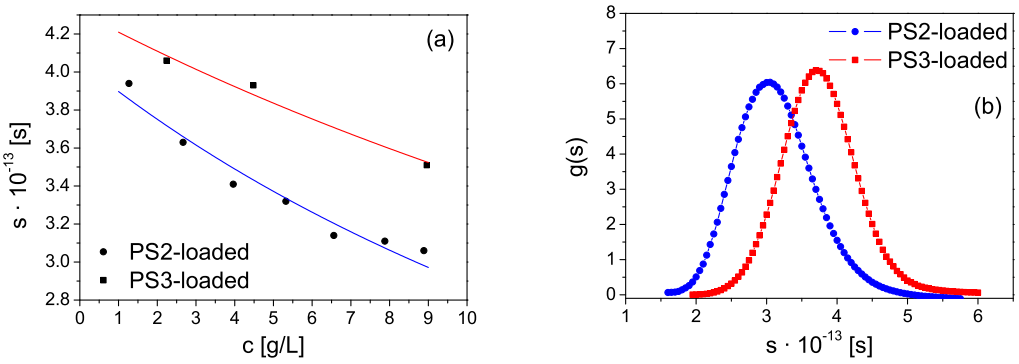

Figure 4.30: a) Concentration dependence and b) distribution of the sedimentation coefficient for PS2-loaded and PS3-loaded.

pendence of the sedimentation coefficient of the solutions. The data was extrapolated to the limit of zero concentration using equation (3.36). The calculated s_0 values are (4.0 $\pm$ 0.6) $\cdot$ 10^{-13} and (4.3 $\pm$ 0.5) $\cdot$ 10^{-13} for PS2-loaded and PS3-loaded, respectively. The standard deviation of the sedimentation coefficient was calculated from the width of the distribution (Figure (4.30 b)) by fitting a Schulz-Zimm distribution to the experimental data. These s_0 values are slightly larger then for the unfilled micelles, which indicates that the mass and frictional coefficient and, thus, the volume increase and compensate each other. This finding was confirmed by a measurement of the specific volume of PS2-loaded, which yields (0.813 $\pm$ 3 $\cdot$ 10^{-3}) cm^3/g, which is close to the value of the unfilled PS2 solution. The apparent molecular weight of the micelles, M_{app}, was estimated by equation (4.28) and assuming a specific volume of PS3-loaded of (0.82 $\pm$ 3 $\cdot$ 10^{-3}) cm^3/g. The calculated M_{app} values are 4.3 $\cdot$ 10^5 g/mol for PS2-loaded and 4.4 $\cdot$ 10^5 g/mol for PS3-loaded. For the incorporation we used an equimolar amount of 1,4-diiodoperfluorobutane with a molecular weight of 454 g/mol. Thus, by dividing the mass of the micelles by the sum of the molecular weight of the single polymer chain and 1,4-diiodoperfluorobutane we can estimate the aggregation number. This yields an aggregation number of 104 for PS2-loaded and 73 for PS3-loaded. These values are significantly larger than for the unfilled case but in agreement with the increased length of the micelles induced by the solubilizate.

In the presence of the solubilizate, the negative free energy contribution arising from a change in the state of dilution of the hydrophobic block accounts for the swelling of the micellar core. This free energy decreases with an increase in the aggregation number and is, thus, favorable to the growth of the aggregates. On the other hand, the changes in the state of deformation of the hydrophobic and hydrophilic blocks and the change in the state of dilution of the hydrophilic block provide positive free energy contributions that increase with increasing aggregation number, limiting the growth of the micelles. In general, it can be said that the micellar dimensions and the aggregation number are larger in the presence than in the absence of a solubilizate.[34] Table (4.13) summarizes the micellar characteristics of the doped micelles obtained by AUC.

Table 4.13: Micellar characteristics of the doped solutions obtained by AUC.

sample-ID	s_0 [10^{-13} s]	M_{app} [g/mol]	Z
PS2-loaded	4.0 ± 0.6	430000	104
PS3-loaded	4.3 ± 0.5	440000	73

4.3.5 Conclusion

The micelles of an ABC triblock polymeric surfactant with varying degrees of polymerization of the hydrophilic middle block, B, and constant length of the hydrophobic blocks, A and C, were investigated by various physicochemical techniques. We have shown that the shape of the micelles formed in aqueous media is cylindrical and that the micelles can be filled with a fluorocarbon dopant when the hydrophilic middle block is long enough. This was interpreted as resulting from the necessity of the presence of a fluorocarbon compartment in the core of the micelle. Furthermore, it was found that the micellization is probably a multi-step association, which is entropy driven.

4.4 Polymer-surfactant complexes in aqueous media

The stoichiometric complexation of polyelectrolytes with oppositely charged low molecular weight surfactants leads to the formation of self-assembled water-insoluble soft-matter, which can show liquid crystalline-like phases. A further addition of surfactants can cause the resolubilization of the precipitates. The excess surfactant molecules associate with the hydrocarbon chains of the complex, with their ionic groups pointing outwards, and transform the complex into a polyelectrolyte whereby the water-solubility is increased.[114] In contrast, nonstoichiometric complexes typically form micellar aggregates as the excess charges stabilize the micelles in the solution.

An example of the different behavior of stoichiometric and non-stoichiometric complexes was given by Thünemann and co-workers.[115, 116] The authors investigated complexes of high molecular weight poly(ethylene imine) (PEI) (M_w = 25000 g/mol) and *n*-alkyl carboxylic acids. For a (1:1) stoichiometry the complexation results in water-insoluble solid-state complexes, which show order-order transitions from smectic C to smectic A at a certain temperature.[115] In comparison a complex with an excess of 50 mol % of the same PEI and dodecanoic acid forms nanoparticles of a core-shell type, which are suitable as carriers of lipophilic drugs such as Q_{10} and triiodothyronine.[116] The use of dihydrophilic block copolymers bearing an ionic block and a noncharged block instead of ionic homopolymers avoids the macroscopic phase separation even for stoichiometric complexes of oppositely charged compounds, as the noncharged hydrophilic block keeps the complexed part in solution. The aggregates of such block polyelectrolyte complexes have a hydrophilic corona and a hydrophobic core formed as a result of the complexation.

4.4.1 Chemical characteristics

The association of oppositely charged block polyelectrolytes and surfactants is also a very flexible and convenient method to introduce incompatible segments into a polymer for the formation of multicompartment micelles. For this purpose, we investigated complexes of an ABA triblock copolymer poly(ethylene oxide)-*b*-poly(diallyl dimethyl ammonium chloride)-*b*-poly(ethylene oxide) (PEO-*b*-PDADMAC-*b*-PEO) with a cationic middle block and low-molecular-weight carboxylic and perfluorocarboxylic acids. Due to the two water-soluble PEO blocks, the micelles are stabilized also at (1:1) stoichiometry. The ABA triblock copolymer was prepared by a two step synthesis. First a macro-azoinitiator, which

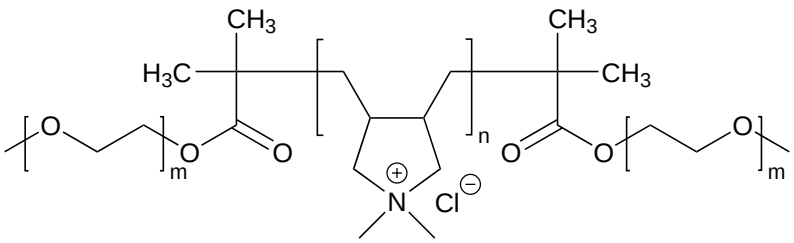

Figure 4.31: Chemical structure of PEO-*b*-PDADMAC-*b*-PEO

contains the two poly(ethylene oxide) blocks was synthesized using azobis(isobutyronitrile) (AIBN) as initiator. In the second step, this macro-azoinitiator was used to synthesize the diallyl dimethyl ammonium chloride block via radical polymerization in water at about 80-85 °C.[117]

Table 4.14: Polymer characteristics of PEO-*b*-PDADMAC-*b*-PEO.

sample-ID	m*	n*	M_n [g/mol]*	M_n [g/mol]**	M_w/M_n**
PEODA	17	56	8770	10000	1.60

* determined by ^{1}H NMR; ** determined by SEC

4.4.2 Complex preparation and micelle formation

For the preparation of the triblock-surfactant complexes, PEO-*b*-PDADMAC-*b*-PEO was dissolved in water and heated to 90°C. The carboxylic and perfluorocarboxylic acids were dispersed in water and also heated to 90°C. The pH was adjusted to 8 by the addition of sodium hydroxide. The surfactant solutions were added slowly to the polymer solutions to form complexes and then cooled to room temperature. Mixed complexes of two surfactants were prepared by adding a mixed solution of both to the polymer solution. The stoichiometry was calculated with respect to the number of ammonium groups of the triblock and surfactant moieties and selected such that the complex does not precipitate. Afterwards, methanol was added to the solutions in a (1:1) ratio, which dissolves the complexes and was then slowly evaporated at 60°C. Finally all complex solutions were clear or slightly opaque. The last step was done to form and equilibrate the micellar structure in water. From the 14 different polymer-surfactant complexes prepared only a few representative are presented (Table (4.15)). In general, it can be said that on increasing the

Table 4.15: Composition of the polymer-surfactant complexes.

sample-ID	surfactant	complex ratio*
C8	C_7H_{15}-COOH	1:1
CF8	C_7F_{15}-COOH	5:1
C6CF6	C_5H_{11}-COOH C_5F_{11}-COOH	5:1:1
C12CF12	$C_{11}H_{23}$-COOH $C_{11}F_{23}$-COOH	10:1:1

* polymer : surfactant1 : surfactant2

hydrophobicity of the surfactant by increasing the chain length or using a perfluorinated surfactant, it was necessary to go to nonstoichiometric complex ratios since stoichiometric amounts resulted in water-insoluble soft-matter materials. The excess charges of the nonstoichiometric complex increase the water solubility of the polymer backbone, which stabilizes the aggregates of the complex.

4.4.3 Aggregation behavior in aqueous media

Static light scattering were used to determine the basic characteristics of the aggregates. The measurements were performed in salt free aqueous solutions at a concentration of about 0.25 g/L. Figure (4.32a) shows the so-called Zimm-plot of the static light scattering data of C8, C6CF6 and C12CF12 where the inverse Rayleigh ratio is plotted as a function of the scattering vector squared. By a linear fit of the Zimm-plot, the radius of gyration, R_g, can be determined according to equation (3.10). Strictly speaking, the Zimm approximation is not valid in this case, as the scattering particles are to large ($qR_g > 1$). Nevertheless for a rough estimation of the radius of gyration, the equation is still applicable. The results are summarized in Table(4.16). From the curve characteristics of the Kratky-plot (Figure (4.32b)) the shape of the particles were estimated to be rod-like in the case of C8 and C12CF12 as the curves are increasing linearly whereas C6CF6 probably consists of coiled aggregates as the curve bends at higher q values (ref. Fig.(3.2 b)). For

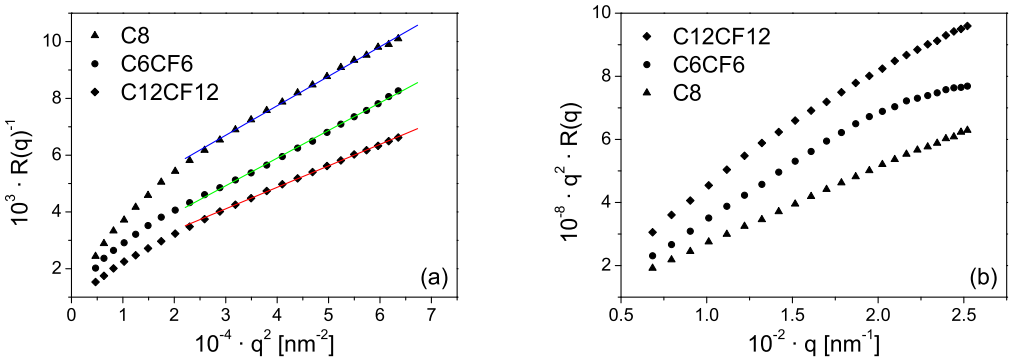

Figure 4.32: a) Zimm-plots and b) Kratky-plots of the complex solutions in salt free aqueous media.

the CF8 sample we used a so-called Berry-plot[118] to linearize the scattering data where the square root of the inverse Rayleigh ratio is plotted as a function of the square of the scattering vector (Figure (4.33)). In this case, the radius of gyration was estimated to be 183.1 nm. The shape of the curve of the Kratky-plot (Fig. (4.32b)) clearly indicates that the CF8 aggregates are spherical. The curve could be fitted by the scattering of a sphere

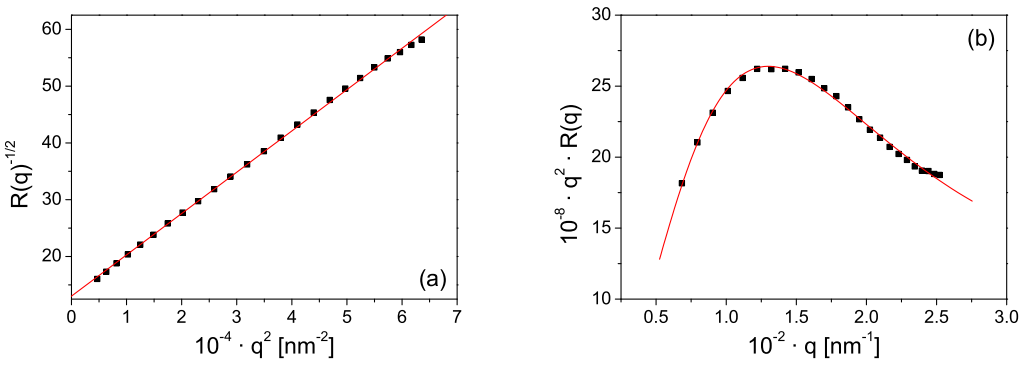

Figure 4.33: a) Berry-plot and b) Kratky-plot of the CF8 complex solutions in salt free aqueous media.

with a Schulz-Zimm radius distribution. According equation (3.25) and (4.13) the radius was calculated to be 226 ± 94 nm, represented in the graph as solid line. Considering the broad distribution of the radius, this is in good agreement with the result from the Berry-plot.

Table 4.16: Characteristics of the aggregates of the polymer-surfactant complexes.

sample-ID	R_g [nm]	shape
C8	93.2	rod-like
CF8	183.1	spherical
C6CF6	120.9	coil
C12CF12	111.1	rod-like

Atomic force microscopy (AFM) was employed to visualize the morphology of the aggregates formed by the polymer-surfactant complexes. The samples for the AFM measurements were prepared by spin coating the complex solutions on a mica substrate. Figure (4.34) shows AFM micrographs of C8. The images reveal rod-like objects with a broad length distribution of 30 - 100 nm and an average width of about 12 nm. The shape of the particles is in agreement with the result from the static light scattering experiments. However, the dimensions of the aggregates are a bit smaller than expected from light scattering. This can be due to breaking of the structure during the sample preparation for AFM. In Figure (4.35), the AFM micrographs of CF8 at two different resolutions are presented. The images show spherical objects with a broad size distribution of 25 - 100 nm in diameter. The spherical shape of the particles is in good agreement with the light scattering results, but the size is significantly smaller than expected from light scattering.

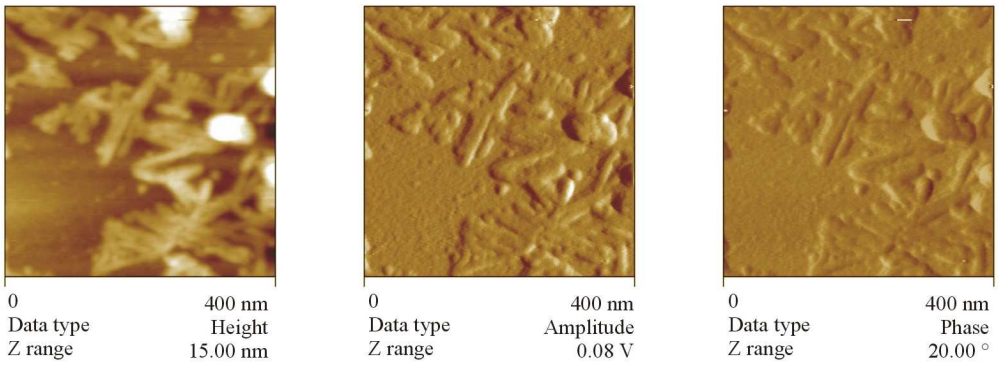

Figure 4.34: AFM micrographs of C8

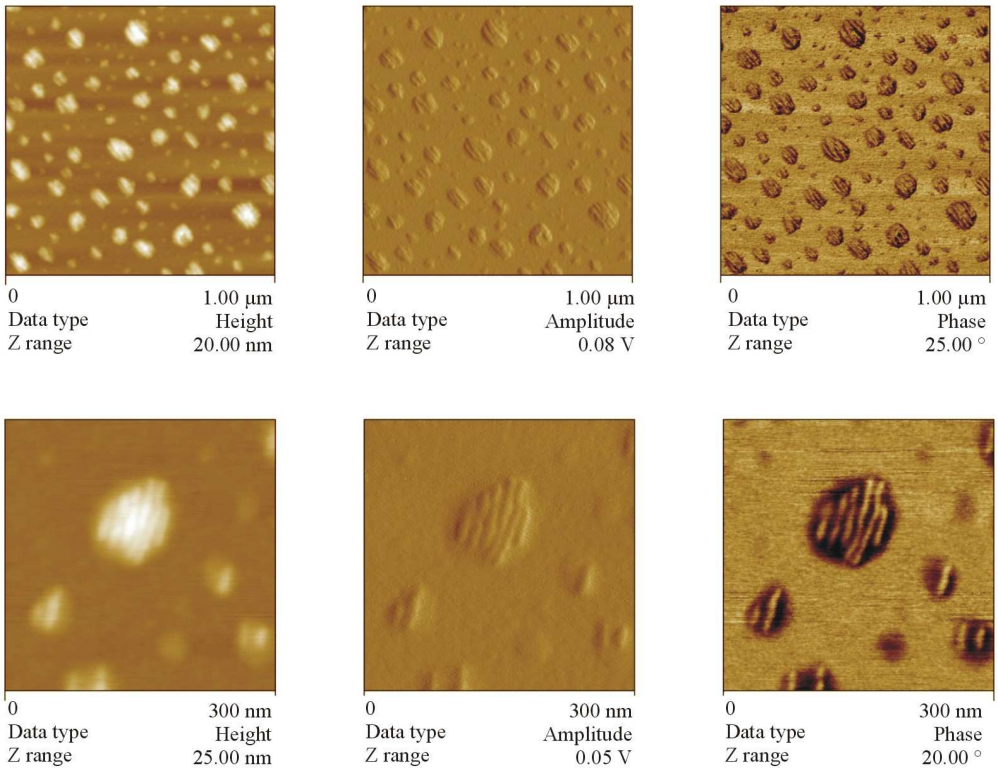

Figure 4.35: AFM micrographs of CF8

A possible reason for this could be, that the aggregates broke apart during the sample preparation and therefore many small objects are visible. Noteworthy is also the lamellar inner structure of the aggregates. In the phase image on the right hand side, one can clearly see bright strips in an uniform distance. From this we conclude that the comparatively stiff fluorine chains form a lamellar phase, surrounded by the softer polymer backbone. The fluorine layer thickness is about 6 nm and the interlayer distance is 4 - 7 nm. For a C_8F_{17} double layer this thickness is much too large, since two fully stretched chains have a thickness of about 2.4 nm. This deviation could be due to the finite size of the AFM tip, which results in an overestimation of the size of the objects. This example shows that by simply changing the complexed chains from hydrocarbon to fluorocarbon of equal length, the resulting aggregates and their microstructures are completely different. This is understandable as the fluorocarbon chains have a much stronger tendency to phase separate from the surrounding hydrocarbons than hydrocarbon chains. Additionally, the hydrophobicity of fluorocarbons is significantly higher than for hydrocarbons with equal length.[119]

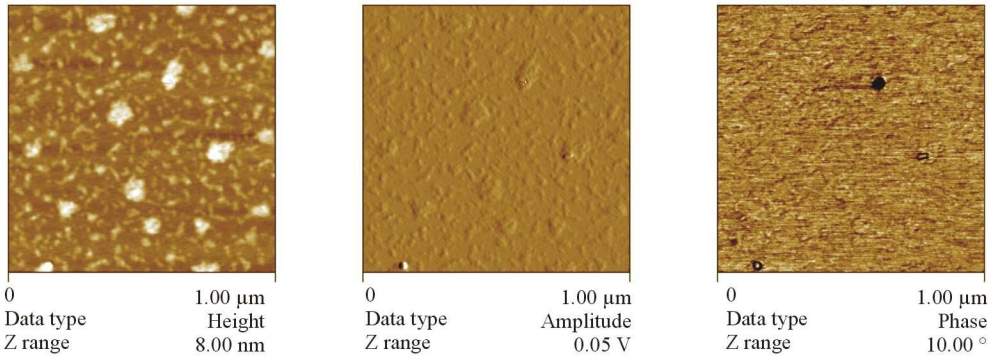

Figure 4.36: AFM micrographs of C6CF6

Figure (4.36) shows AFM micrographs of the C6CF6 mixed complex. The images reveal uniformly dispersed spherical objects with a diameter of 50 - 80 nm. Similarly to the two other investigated samples the shape observed confirms the SLS measurements but the size of the aggregates is smaller than expected from the light scattering results, which can be caused by sample preparation for the AFM measurements. Unfortunately, the AFM image of C6CF6 shows no indication of a fluorocarbon-hydrocarbon phase separation as was expected. One reason for this could be that the chains are not long enough allow for visibly phase separation. Therefore a mixed complex with longer (C_{12}) chains was prepared. However, as the AFM image shows (Fig. (4.37)), also in this case is phase separation not detected. The aggregates shown in the micrograph are rod-like with a length of 80 - 300 nm and a thickness of about 20 nm. In this case the size and shape of the aggregates are in agreement with the results from the static light scattering experiment.

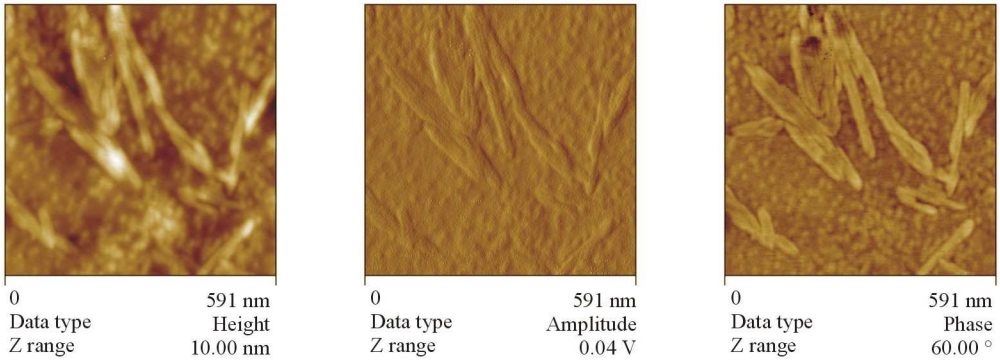

Figure 4.37: AFM micrograph of C12CF12

4.4.4 Conclusion

The above studies demonstrate that the complexation of an ABA triblock copolymer with fluorinated and alkylated surfactants results in the formation of stable aggregates in salt free aqueous solution. Depending on the surfactant and its chain length, the complexes show various morphologies, e.g. spherical or rod-like. Unfortunately we could not prepare truly phase separated two compartment aggregates with this polymer system. Nevertheless, the ionic complexation is potentially a feasible method for the introduction of a multicompartment character into a polymer-surfactant system.

Chapter 5

Summary and Outlook

In the present study four different approaches for the formation of multicompartment micellar systems in aqueous solution were investigated. In the first approach we used an amphiphilic ABC triblock copolymer (poly(4-vinylbenzyl *N*-methylmorpholinium chloride)-*b*-polystyrene-*b*-poly(4-vinylbenzyl pentafluorophenol ether)) with a cationic hydrophilic block and two hydrophobic blocks: a hydrocarbon one and a partially fluorinated one. The self-assembly of the copolymer in aqueous solution and especially the dependence of the morphology on the way of preparation of the micellar solution was studied by employing cryo-transmission electron microscopy (cryo-TEM), static light scattering (SLS) and small angle X-ray scattering (SAXS). The first method of preparation was the step-wise dialysis of a water/dioxane solvent mixture against water. The results of the measurements indicated that the copolymer self-assembles to multicompartment micelles possessing a diameter of about 30 nm. As evidenced by cryo-TEM, the hydrophobic core exhibits a nano-segregated morphology with many small, fluorocarbon rich domains coexisting with a continuous hydrocarbon rich region. However, from the cryo-TEM micrographs it was not possible to determine whether the fluorocarbon domains cover the surface of a central hydrocarbon core (sphere on sphere) or whether they are embedded in the hydrocarbon core (sphere in sphere), as both scenarios look identical in the cryo-TEM micrographs.

By comparing the micellar size from theoretical calculations with the values obtained from the cryo-TEM micrographs, we conclude that the fluorocarbon domains are only composed of the fluorocarbon moieties of the partially fluorinated block. The surrounding hydrocarbon domain contains both the hydrocarbon moieties of the partially fluorinated block and the hydrocarbon middle block. The second preparation method involved evaporation of tetrahydrofuran (THF) from a water/THF mixture. In this case the cryo-TEM

micrographs revealed singly dispersed spherical fluorocarbon domains. From this finding we conclude that, in contrast to the dialysis technique, the evaporation of THF leads to the formation of multicompartment micelles with a layered core-shell-corona morphology. Furthermore we assume that the fluorocarbon moieties of the partially fluorinated block form the core, which is surrounded by a hydrocarbon shell containing the hydrocarbon moieties of the partially fluorinated block and the hydrocarbon middle block. In spite of the different core morphologies in both micellar systems, the hydrophilic block forms the water-soluble corona and the overall diameters of the micelles, estimated by theoretical calculations, were found to be comparable. Hence, our study has shown, that the micellar morphology of the used copolymer depends censoriously on the preparation method and the utilized solvents. This may give the possibility of optimizing the preparation technique to achieve a certain micellar morphology and confirms that, for polymeric systems, the influence of the way of micelle preparation has to be considered.

In the second approach to obtain a multicompartment system, a novel ABCBA pentablock copolymer was synthesized and its aggregation behavior in aqueous media investigated. The synthesis of the copolymer was done by a carboxyl-amine coupling reaction, where an α,ω-functionalized perfluoropolyether was combined with an amino chain-end functionalized diblock copolymer poly(ethylene oxide)-*b*-poly(γ-benzyl-L-glutamate). As evidenced by cryo-TEM, in aqueous solution the pentablock copolymer forms a coexisting mixture of spherical and worm-like micelles with probably a core-shell-corona morphology. We assume that the core is formed by the perfluoropolyether surrounded by a shell of poly(γ-benzyl-L-glutamate) whereas the corona is formed by the water-soluble poly(ethylene oxide) block. The diameter of the fluorinated core is similar for both micellar structures. From dynamic light scattering the hydrodynamic radii of the spherical and the worm-like micelles were determined and were found to be in good agreement with the results obtained from cryo-TEM. Moreover, the CD-spectrum indicated that the poly(γ-benzyl-L-glutamate) block has a β-sheet conformation, which is typical for short chain glutamates. Due to the secondary structure, the peptide block may possess a stimuli responsive character, which can be interesting for future investigations. For example, the influence of the pH-dependant order-disorder transition of the peptide block on the aggregate morphology, may give the possibility for a triggered released of an incorporated drug.

The third approach was the investigation of micelles of an ABC triblock polymeric surfactant, 1H, 1H, 2H, 2H perfluorodecane -*b*- poly(2-methyl-2-oxazoline) -*b*- *N*-hexadecylpiperazine, with varying degrees of polymerization of the hydrophilic middle block, B, and constant length of the hydrophobic blocks, A and C. By applying various characterization techniques we have shown that the shape of the micelles formed in aqueous solution is cylindrical with radii of 3-4 nm, depending on the length of the hydrophilic block. The lengths of the cylindrical micelles also vary with the hydrophilic block length and are about 20-30 nm. Furthermore, it was found that the micellization probably represents an entropy driven multi-step association process. An interesting find was that the micelles can solubilize a low molecular weight fluorocarbon dopant, which can be treated as a model substance for fluorocarbon rich drugs. However, the solubilization was successful only when the hydrophilic middle block was relatively long. We assume that the doped micelles form distinct fluorocarbon domains, which are able to selectively incorporate the fluorocarbon dopant. Due to the presence of the dopant, the micelles form a clear core-shell-corona structure with the radius and length being significantly increased compared to the unfilled micelles. Unfortunately, a real proof for a selective solubilization either in the hydrocarbon rich or in the fluorocarbon rich compartment has not yet been achieved.

The idea of the fourth approach was to look for an alternative way for the preparation of multicompartment aggregates by using ionic interactions instead of covalent bonds. For this purpose, an ABA triblock copolymer poly(ethylene oxide)-*b*-poly(diallyl dimethyl ammonium chloride)-*b*-poly(ethylene oxide), with a cationic middle block was complexed with low molecular weight carboxylic and perfluorocarboxylic acids of different chain lengths. Our studies showed that, independent of the length of the surfactant, the complexation results in the formation of stable aggregates in salt free aqueous solution. Nevertheless the size and structure of the formed aggregates strongly depend on the type of surfactant and its chain length. For example, by using a perfluorinated surfactant instead of a hydrocarbon one with equal chain length, the complexation ratio had to be changed to obtain stable aggregates. Additionally, the structure of the aggregates changed from rod-like to spherical. Unfortunately, the preparation of truly nano-phase separated two compartment aggregates with this polymer system has not yet been achieved. Therefore, further investigations are necessary especially since ionic complexation is a potentially feasible method for introduction of a multicompartment character into a polymer-surfactant system.

The novel structured nano-objects presented in this study show a multicompartment character. There is no doubt that these copolymeric systems have great potential to be utilized in diverse areas of chemistry, biochemistry and medicine. For example, they may serve as models as well as mimics for biological structures such as globular proteins, and might be the base for novel advanced drug-delivery systems.

Appendix A

Experimental part

A.1 Experimental techniques

Static light scattering (SLS). The static light scattering measurements were performed on a Sofica instrument equipped with a He-Ne laser ($\lambda = 632.8$ nm). The scattered light intensity was recorded at scattering angles from 30° to 145° at 5° intervals. Toluene was used for calibration to determine the scattering volume corrected Rayleigh ratio. All measurements were performed at (25 ± 0.1) °C. 10 mL of micellar solution was placed into a cylindrical quartz cuvette with a diameter of 2 cm. Prior to measurement, the sample was filtered with a 0.2 μm or 0.45 μm millipore syringe filter in order to free it from dust particles. The cuvettes were extensively cleaned in an ultrasound bath using a surfactant solution (Hellmanex, Hellma) and subsequently washed several times with distilled water to completely remove any remaining surfactants. Finally, they were washed for 20 min with boiling acetone in a special dust-free chamber and stored in a desiccator.

Dynamic light scattering (DLS). The dynamic light scattering measurements were performed using a Malvern Instruments particle sizer (HPPS-ET 5002) (Malvern Instruments, UK) equipped with a He-Ne laser ($\lambda = 632.8$ nm). The scattering data was recorded at (25 ± 0.1) °C in backscattering modus at a scattering angle of $2\theta = 173°$. 1.5 mL of the aqueous sample solution was placed into a square 10×10 mm disposable polystyrene cuvette. For samples in organic solvents we used a square 10×10 mm quartz cuvette instead. Prior to measurement the sample was filtered with a 0.45 μm millipore syringe filter in order to free it from dust particles.

Small angle X-ray scattering (SAXS). For the small-angle X-ray scattering measurement, the solution was placed into a 2 mm capillary made of borosilicate with a wall thickness of about 0.01 mm. The SAXS curves were recorded at room temperature with a Bruker Nanostar (1.5 KW, Cu Kα) with pinhole collimation and a xenon filled Siemens HI-STAR area detector (512x512 pixel, $\Delta\theta \sim 0.02°$). The distance between sample and detector was 610 mm, covering a range of the scattering vector $q = (4\pi/\lambda)\sin(\theta) = 0.2 - 3.5$ nm^{-1} (2θ: scattering angle, $\lambda = 0.15418$ nm). 2D scattering patterns were transformed into a 1D radial average of the scattering intensity.

Analytical ultracentrifugation (AUC). Analytical ultracentrifugation was carried out using a Beckman-Coulter Optima XL-I ultracentrifuge (Beckman Coulter, Palo Alto, CA) at (20 ± 0.1) °C and 50000 rpm for sedimentation velocity experiments and 15000 rpm for sedimentation equilibrium experiments. The sample solutions were placed into a 12 mm double sector cell of carbon filled Epon for sedimentation velocity experiments and into a 12 mm 6-channel cell of carbon filled Epon for sedimentation equilibrium experiments. Detection of the sedimenting boundary was carried out using a Rayleigh interference optic equipped with a He-Ne laser ($\lambda = 632.8$ nm).

Atomic force microscopy (AFM). AFM measurements were performed on a Nano-Scope IIIa Microscope (Digital Instruments, USA) using a 10×10 μm cantilever (Model TESP; resonant frequency: 300 kHz; force constant: 42 N/m). All measurements were carried out with tapping mode at room temperature. Dilute sample solutions were spin coated on mica surface to be visualized by AFM.

Cryo transmission electron microscopy (cryo-TEM). The samples for cryo-TEM were prepared at room temperature by placing a droplet (10 μL) of the solution on a hydrophilized perforated carbon filmed grid (60 s Plasma treatment at 8 W using a BALTEC MED 020 device). The excess fluid was blotted off to create an ultrathin layer (typical thickness of 100 nm) of the solution spanning the holes of the carbon film. The grids were immediately frozen in liquid ethane at its freezing point (-184 °C) using a standard plunging device. Ultra-fast cooling is necessary for an artifact-free thermal fixation (vitrification) of the aqueous solution avoiding crystallization of the solvent or rearrangement of the assemblies. The vitrified samples were transferred under liquid nitrogen into a Philips CM12 transmission electron microscope using the Gatan cryoholder and cryostage (Model

626). Microscopy was carried out at -175 °C (sample temperature) using the microscopes low dose protocol at a primary magnification of 58300×. The defocus was chosen to be 2.0 μm.

Isothermal titration calorimetry (ITC). The isothermal calorimetry measurements were carried out with a VP-ITC micro calorimeter from MicroCal (Northhampton, MA). Two identical spherical cells, a reference cell and a sample cell, both with a volume of 1.442 mL, were enclosed in an adiabatic jacked. The working cell was filled with the sample solution, and the reference cell was filled with the solvent used to prepare the sample solution. The sample was injected stepwise into the working cell with a syringe of a total volume of 288 μL. The sample cell was constantly stirred at a stirring rate of 310 rpm. The measurements were performed at a constant temperature of (25 ± 0.01) °C. Small aliquots of the sample (typically 10 μL) were successively injected into the solution of the working cell. The first injection was usually set to a volume of 2 μL. Because of possible dilution during the equilibration time preceding the measurement, the first injection was ignored in the analysis of the data. Each injection produced a characteristic peak in the heat flow due to released or absorbed heat. In the analysis, a base line was subsequently subtracted from the data, which corresponds to the signal between consecutive injections when no change in the heat flow was detected. Integrating each of the peaks provides the heat per injection. The data analysis was performed using the Origin software provided by MicroCal.

Density. The density measurements were performed with a density meter (DMA 60/602, Paar, Austria). It is based on a vibrating mass whose resonance frequency is influenced by the density of the polymer solution (oscillating U-tube principle). The correctness as given for the density of water was ± 0.5 · 10^{-6} g/cm^3 and the temperature was held constant at (20 ± 0.01) °C.

Viscometry. Viscosity measurements were performed at (20 ± 0.1) °C using an Ubbelohde capillary viscometer with automatic dilution.

Surface tension. The surface tension was determined using the pendant drop method. A profile analysis tensiometer PAT1 from SINTECH was operated at room temperature. The shape of the drop is given by the Gauß-Laplace equation, which represents a relation-

ship between the curvature of a liquid meniscus and the surface tension, γ. The surface tension was measured as a function of time to monitor the equilibration process. The accuracy in surface tension is $\pm$ 0.1 mN/m.

Infra-red spectroscopy. IR spectra were recorded on a BioRad 6000 FT-IR. All samples were measured in the solid state using a single reflection diamond ATR.

Circular dichroism The circular dichroism (CD) spectrum was measured at room temperature on a Jasco J715 spectropolarimeter. The sample solution with a concentration of about 0.26 g/L was placed into a square quartz cuvette with a path length of 1 mm. The CD spectrum of water was subsequently subtracted.

A.2 Synthesis

Incorporation of 1,4-diiodoperfluorobutane into micelles of 1H,1H,2H,2H-perfluorodecyl-poly(2-methyl-2-oxazoline)-1-hexadecyl-piperazine (*PS2, PS3*). The polymer **PS2** (68.1 mg, $1.21 \cdot 10^{-5}$ mol) was dissolved in 10 mL of water. Then 10 mL acetone was added and the solution was treated with ultra sound for 5 min in an ultra sound bath. A stock solution of 1,4-diiodoperfluorobutane was prepared by dissolving 1 mL ($1.13 \cdot 10^{-4}$ mol) in 10 mL acetone. An amount of 1mL of the stock solution, containing $1.13 \cdot 10^{-5}$ mol 1,4-diiodoperfluorobutane, was added to the solution of **PS2**. This mixture was stirred gently and heated to 50 °C for 12 hours to evaporate the acetone. During this process the micelles formed and were loaded simultaneously with 1,4-diiodoperfluorobutane. Evaporated water was replaced and a clear micellar solution was obtained. The same procedure was carried out with **PS3** where 60.6 mg ($8.8 \cdot 10^{-6}$ mol) were mixed with $8.82 \cdot 10^{-6}$ mol 1,4-diiodoperfluorobutane soluted in 0.663 mL stock solution. Here we also observed a clear micellar solution.

Coupling of poly(ethylene oxide)-*b*-poly(γ-benzyl-L-glutamate) with perfluoropolyether Perfluorpolyether functionalized with two carboxylic acid endgroups in the α and ω positions (34.1 mg, $0.9 \cdot 10^{-6}$ mol) was dissolved in 5 mL dimethylformamide (DMF). Then, 100.2 mg ($1.86 \cdot 10^{-5}$ mol) poly(ethylene oxide)-*b*-poly(γ-benzyl-L-glutamate) (PEO-*b*-P(BLG)) with an amine endgroup functionality, 9.5 mg ($8.3 \cdot 10^{-5}$ mol) *N*-hydroxysuccinimide (NHS) and 83.4 mg ($4.01 \cdot 10^{-4}$ mol) *N,N'*-dicyclohexylcarbo-

diimide (DCC) were added successively to the solution. The mixture was treated with ultra sound for 5 min in an ultrasonic bath and subsequently stirred for 18 hours. During the reaction an urea derivative of the carbodiimide is formed, which precipitates and is filtered out afterwards. Finally we obtained a clear solution.

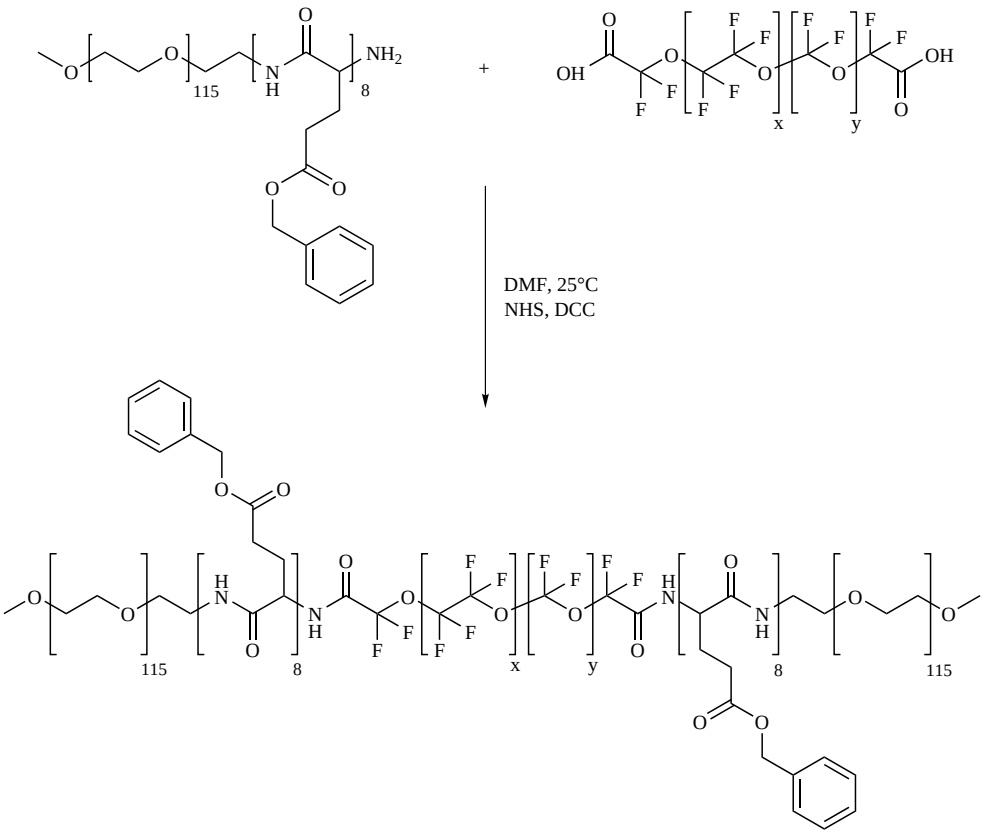

Figure A.1: Reaction scheme for the preparation of the pentablock PEO-*b*-P(BLG)-*b*-PFPE-*b*-P(BLG)-*b*-PEO.(x ≫ y)

Appendix B

Abbreviations

AFM	Atomic force microscopy
ATRP	Atom transfer radical polymerization
AUC	Analytical ultracentrifugation
$(c)_n$	Pochhammer factorials
D_{app}	Apparent translational diffusion coefficient
D_c	Diameter of the micellar core
D_m	Diameter of the micelle
DLS	Dynamic light scattering
DMF	*N,N*-Dimethylformamide
DP	Degree of polymerization
$\mathscr{F}$	Fourier transform
${}_iF_j$	Hypergeometric function
$F(q)$	Scattering amplitude
$\Gamma(x)$	Gamma function
$I(q)$	Scattering intensity
IR	Infra-red
ITC	Isothermal titration calorimetry
M_{app}	Apparent molecular weight
M_n	Number-averaged molecular weight
M_w	Weight-averaged molecular weight
ODT	Order-disorder transition
$P(q)$	Form factor
P(BLG)	Poly(γ-benzyl-L-glutamate)

PDADMAC	Poly(diallyl dimethyl ammonium chloride)
PEO	Poly(ethylene oxide)
PFPE	Perfluoropolyether
PS	Polystyrene
PVBFP	Poly(4-vinylbenzyl pentafluorophenol ether)
PVBM	Poly(4-vinylbenzyl *N*-methylmorpholinium chloride)
R_g	Radius of gyration
R_h	Hydrodynamic radius
RAFT	Reversible addition-fragmentation chain-transfer polymerization
rpm	Rounds per minute
σ	Root mean square deviation
s	Sedimentation coefficient
SAXS	Small angle X-ray scattering
SEC	Size exclusion chromatography
SLS	Static light scattering
TEM	Transmission electron microscopy
THF	Tetrahydrofuran
UV	Ultra-violet
V_c	Volume of the micellar core
V_m	Volume of the micelle
χ	Flory-Huggins interaction parameter
Z	Aggregation number

Appendix C

Acknowledgments

Finally, I would like to thank all the people whose contribution in this work was valuable:

Prof. Dr. Helmuth Möhwald, for the opportunity to work on this interesting project and all the fruitful discussions.

My supervisor, PD Dr. habil. Andreas F. Thünemann (BAM Berlin), for his continuous help and all the discussions with him, which helped to find answers in many questions concerning this work.

Prof. Dr. André Laschewsky (FhG-IAP) and Dr. Jean-François Lutz (FhG-IAP) for their support, the numerous discussions and helpful suggestions.

Dr. Ralf Weberskirch (Tech. University Munich), Dr. Jean-François Baussard (FhG-IAP) and Dr. Christoph Kozlowski (FhG-IAP) for kindly providing the polymers for this work.

Dr. Eckhard Görnitz (FhG-IAP), Dr. habil. Helmut Cölfen and Antje Völkel for introducing me to the ultracentrifugation technique and all the helpful discussions concerning the interpretation of the data.

Dr. Rumiana Dimova and Dr. Cornelia G. Sinn for nicely introducing me to the ITC technique and all the discussions.

Dr. Hans von Berlepsch (Free University Berlin) for his kindness to provide the TEM and cryo-TEM micrographs.

Dr. Reinhard Miller and Sabine Siegmund for the surface tension measurements and the discussions concerning the results.

Dr. Andreas Erbe and Dr. Reinhard Sigel for all the fruitful discussions about light scattering.

Anne Heilig and Roy Knocke for numerous AFM measurements.

The members of my group "Nanotechnology for Life Science" at the Fraunhofer IAP: Sabrina Franke, Verena Jentzen, Dagmar Schütt and Nathalie Sieverling as well as all the members of the Fraunhofer IAP group "Water-born Polymer Systems" for the nice support and the good atmosphere in the lab.

A "Thank you" goes also to all the people who supported my work by varios contributions: Ingeborg Bartsch, Marlies Gräwert, Dr. Magdalena Losik, Olaf Niemeyer, Rona Pitschke, Dr. Rainer Rihm (FhG-IAP), Dr. Helmut Schlaad, Dr. Bernd Smarsly, Dr. Hendrik Wetzel (FhG-IAP) and Ingrid Zenke.

A big "Thank you" also to Danielle Franke for all the corrections she did on this thesis.

A very special "Thank you" goes to Justyna for all her love and every day support as well as for all the discussions about our work.

And last but not least, I would like to thank my parents and also my family for all the moral support throughout these years.

Bibliography

[1] Kragh-Hansen, U., *Dan. Med. Bull.,* **1990,** *37,* 57-84.

[2] He, X.M.; Carter, D.C., *Nature,* **1992,** *358,* 209-215.

[3] Bates, F.S.; Fredrickson, G.H., *Physics Today,* **1999,** *February,* 32-38.

[4] Förster, S.; Plantenberg, T., *Angew. Chem. Int. Ed.,* **2002,** *41,* 688-714.

[5] Riess, G.; Hurtrez, G.; Bahadur, P. , Block copolymers. , In *Encyclopedia of Polymer Sciences and Engineering*, Vol. 2, 2nd ed.; John Wiley & Sons: New York, 1985.

[6] Noshay, A.; McGrath, J.E., *Block copolymers: Overview and Critical Survey;* Academic Press: New York, 1977.

[7] Goodman, I., *Developments in Block Copolymers;* Vol. 1 ; Applied Science Publishers: London and New York, 1982.

[8] Faust, R.; Schlaad, H. , In *Applied Polymer Science: 21st Century*; Elsevier: Amsterdam, 2000.

[9] Hadjichristidis, N.; Pispas, S.; Floudas, G.A., *Block copolymers;* Wiley-Interscience: Hoboken, NJ, 2002.

[10] K.A. Davis, K. Matyjaszewski, *Advances in polymer science;* Vol. 159 ; Springer: Berlin, 2002.

[11] Hamley, I.W., *The Physics of Block Copolymers;* Oxford university press: Oxford, New York, Tokyo, 2003.

[12] Matsen, M.W.; Schick, M., *Phys. Rev. Lett.,* **1994,** *72,* 2660.

[13] Matsen, M.W.; Schick, M., *Macromolecules,* **1994,** *27,* 6761-6767; 7157-7163.

[14] Matsen, M.W.; Bates, F.S., *Macromolecules,* **1996,** *29,* 1091-1098; 7641-7644.

[15] Khandpur, A.K.; Förster, S.; Bates, F.S.; Hamley, I.W.; Ryan, A.J.; Brass, W.; Almdal, K.; Mortensen, K., *Macromolecules,* **1995,** *28,* 8796-8806.

[16] Nyrkova, I.A.; Khokhlov, A.R.; Doi, M., *Macromolecules,* **1993,** *26,* 3601-3610.

[17] Merrett, F.M., *J. Polym. Sci.,* **1957,** *24,* 467-477.

[18] Gallot, Y.; Franta, E.; Rempp, P.; Benoit, H., *J. Polym. Sci., Ser. C,* **1964,** *4,* 473-489.

[19] Price, C.; Woods, D., *Polymer,* **1974,** *15,* 389-392.

[20] Tuzar, Z.; Kratochvíl, P., *Makromol. Chem.,* **1972,** *160,* 301-311.

[21] Noolandi, J.; Hong, K.M., *Macromolecules,* **1983,** *16,* 1443-1448.

[22] Leibler, L.; Orland, H.; Wheeler, J.C., *J. Chem. Phys.,* **1983,** *79,* 3550-3557.

[23] Nagarajan, R.; Ganesh, K., *J. Chem. Phys.,* **1989,** *90,* 5843-5856.

[24] Hurter, P.N.; Scheutjens, J.M.H.M.; Hatton, T.A., *Macromolecules,* **1993,** *26,* 5592-5601.

[25] de Gennes, P.G., *Scaling Concepts in Polymer Physics;* Cornell University Press: Ithaca, 1979.

[26] Zhulina, E.B.; Birshtein, T.M., *Vysokomol Soedin, Ser A,* **1986,** *22,* 2403-2412.

[27] Förster, S.; Zisenis, M.; Wenz, E.; Antonietti, M., *J. Chem. Phys.,* **1996,** *104,* 9956.

[28] Schillen, K.; Brown, W.; Johnsen, R.M., *Macromolecules,* **1994,** *27,* 4825-4832.

[29] Förster, S.; Berton, B.; Hentze, H.-P.; Krämer, E.; Antonietti, M.; Lindner, P., *Macromolecules,* **2001,** *34,* 4610.

[30] Moffitt, M.; Zhang, L.; Khougaz, K.; Eisenberg, A. , In *Solvents and Self-Organization of Polymers*, Vol. 327, NATO ASI Series ed.; Eds.; Webber, S.E.; Munk, P.; Tuzar, Z.; Kluwer Academic Publishers: Dordrecht, 1996.

[31] Nakagawa, T. , In *Nonionic Surfactants*, Vol. 1; Ed.; Schick, M.J.; M. Dekker Inc.: New York, 1967.

[32] Attwood, D.; Florence, A.T., *Surfactant Systems. Their Chemistry, Pharmacy and Biology;* Chapman and Hall: London, 1983.

[33] Nagarajan, R.; Barry, M.; Ruckenstein, E., *Langmuir,* **1986,** *2,* 210-215.

[34] Nagarajan, R.; Ganesh, K., *Macromolecules,* **1989,** *22,* 4312-4325.

[35] Molau, G.E.; Wittbrodt, W.M., *Macromolecules,* **1968,** *1,* 260-264.

[36] Ikada, Y.; Horii, F.; Sakurada, I., *J. Polym. Sci., Polym. Chem. Ed.,* **1973,** *11,* 27-40.

[37] Tuzar, Z.; Kratochvíl, P., *Makromol. Chem.,* **1973,** *170,* 177-183.

[38] Lavasanifar, A.; Samuel, J.; Kwon, G.S., *Advanced Drug Delivery Reviews,* **2002,** *54,* 169-190.

[39] Abetz, V.; Goldacker, T., *Macromol. Rapid Commun.,* **2000,** *21,* 16-34.

[40] Bailey, T.S.; Pham, H.D.; Bates, F.S., *Macromolecules,* **2001,** *34,* 6994-7008.

[41] Triftaridou, A.I.; Vamvakaki, M.; Patrickios, C.S., *Macromol. Symp.,* **2002,** *183,* 133-138.

[42] Gohy, J.-F.; Willet, N.; Varshney, S.; Zhang, J.-X.; Jérôme, R., *Angew. Chem. Int. Ed.,* **2001,** *40,* 3214-3216.

[43] Kříž, J.; Masař, B.; Pleštil, J.; Tuzar, Z.; Pospíšil, H.; Doskočilová, D., *Macromolecules,* **1998,** *31,* 41-51.

[44] Lutz, J.-F.; Laschewsky, A., *Macromol. Chem. Phys.,* **2005,** *206,* 813-817.

[45] Laschewsky, A., *Curr. Op. Coll. Int. Sci,* **2003,** *8,* 274-281.

[46] Li, Z.; Kesselman, E.; Talmon, Y.; Hillmyer, M.A.; Lodge, T.P., *Science,* **2004,** *306,* 98-101.

[47] Munk, P. , In *Solvents and Self-Organization of Polymers*, Vol. 327, NATO ASI Series ed.; Eds.; Webber, S.E.; P.Munk; Tuzar, Z.; Kluwer Academic Publishers: Dordrecht, 1996.

[48] Tyndall, J., *Phil. Mag.,* **1869,** *37,* 384.

[49] Rayleigh, Lord J.W., *Phil. Mag.,* **1871,** *41,* 107, 274, 447.

[50] Debye, P., *J. Appl. Phys.,* **1944,** *15,* 338.

[51] Debye, P., *J. Phys. Colloid. Chem.,* **1947,** *51,* 32.

[52] Mie, G., *Ann. Physik,* **1908,** *25,* 377.

[53] Zimm, B.H., *J. Chem. Phys.,* **1948,** *16,* 1093.

[54] Kratky, O.; Porod, G., *Rec. Trav. Chim. Pays-Bas,* **1949,** *68,* 1106-1122.

[55] Siegert, A.J.F., *MIT Rad. Lab.,* **1943,** 465.

[56] Wiener, N., *Acta Math.,* **1930,** *55,* 118.

[57] Khintchine, A.J., *Math. Ann.,* **1934,** *109,* 604.

[58] Schmidt, M. , In *Dynamic Light Scattering*; Ed.; Brown, Wyn; Oxford Science Publications: Oxford, 1993.

[59] Kotlarchyk, M.; Chen, S.-H., *J. Chem. Phys.,* **1983,** *79,* 2461-2469.

[60] Rayleigh, Lord J.W., *Proceedings of the Royal Society (London),* **1911,** *84A,* 25-46.

[61] Rayleigh, Lord J.W., *Proceedings of the Royal Society (London),* **1914,** *90A,* 219.

[62] van Zanten, J.H. , In *Vesicles*; Ed.; Rosoff, Morton; Marcel Dekker Inc.: New York, 1996.

[63] Porod, G., *Kolloid Z.,* **1951,** *124,* 83.

[64] Svedberg, T.; Nichols, J.B., *J. Am. Chem. Soc.,* **1923,** *45,* 2910.

[65] Schachman, H.K., *Ultracentrifugation in Biochemistry;* Academic Press: New York, 1959.

[66] Wales, M.; van Holde, K.E., *J. Polymer Sci.,* **1954,** *14,* 81-86.

[67] Creeth, J.M.; Knight, C.G., *Biochim. Biophys. Acta,* **1965,** *102,* 549-558.

[68] Signer, R.; Gross, H., *Helv. Chim. Acta,* **1934,** *17,* 726.

[69] Creeth, J.M.; Pain, R.H., *Prog. Biophys. Mol. Biol.,* **1967,** *17,* 217-287.

[70] Binning, G.; Quate, C.; Gerber, C., *Phys. Rev. Lett.,* **1986,** *56,* 930.

[71] de Broglie, L.V. *Recherches sur la théorie des quanta (Researches on the quantum theory),* Thesis, Paris, 1924.

[72] Davisson, C.J.; Germer, L.H., *Phys. Rev.,* **1927,** *30,* 705.

[73] Thomson, G.P., *Proceedings of the Royal Society (London),* **1928,** *117A,* 600.

[74] Ubbelohde, L., *Ind. Eng. Chem., Anal. Ed.,* **1937,** *9,* 85.

[75] Schulz, G.W.; Blaschke, F., *J. prakt. Chem.,* **1941,** *158,* 130.

[76] Huggins, M.L., *J. Am. Chem. Soc.,* **1942,** *64,* 2716-2718.

[77] Andreas, J.M.; Hauser, E.A.; Tucker, W.B., *J. Phys. Chem.,* **1938,** *42,* 1001-1019.

[78] Neumann, A.W.; Spelt, J.K., *Applied Surface Thermodynamics;* Marcel Dekker: New York, 1996.

[79] Weberskirch, R.; Preuschen, J.; Spiess, H.W.; Nuyken, O., *Macromol. Chem. Phys.,* **2000,** *201,* 995-1007.

[80] Li, Z.; Hillmyer, M.A.; Lodge, T.P., *Macromolecules,* **2004,** *37,* 8933-8940.

[81] Boschet, F.; Branger, C.; Margaillan, A.; Hogen-Esch, T.E., *Polymer International,* **2005,** *54,* 90-95.

[82] Bates, F.S., *Science,* **1991,** *251,* 898.

[83] Riess, G., *Prog. Polym. Sci.,* **2003,** *28,* 1107-1170.

[84] Won, Y.Y.; Davis, H.T.; Bates, F.S., *Science,* **1999,** *283,* 960-963.

[85] Discher, D.E.; Eisenberg, A., *Science,* **2002,** *297,* 967-973.

[86] Patrickios, C.S.; Lowe, A.B.; Armes, S.P.; Billingham, N.C., *J. Polym. Sci., Part A: Polym. Chem.,* **1998,** *36,* 617-631.

[87] Cai, Y.; Armes, S.P., *Macromolecules,* **2004,** *37,* 7116-7122.

[88] Sfika, V.; Tsitsilianis, C.; Kiriy, A.; Gorodyska, G.; Stamm, M., *Macromolecules,* **2004,** *37,* 9551-9560.

[89] Yu, G.-E.; Eisenberg, A., *Macromolecules,* **1998,** *31,* 5546-5549.

[90] Brannan, A.K.; Bates, F.S., *Macromolecules,* **2004,** *37,* 8816-8819.

[91] Baussard, J.-F.; Habib-Jiwan, J.-L.; Laschewsky, A., *Langmuir,* **2003,** *19,* 7963.

[92] Breiner, U.; Krappe, U.; Jakob, T.; Abetz, V.; Stadler, R., *Polymer Bulletin,* **1998,** *40,* 219-226.

[93] Ritzenthaler, S.; Court, F.; David, L.; Girard-Reydet, E.; Leibler, L.; Pascault, J. P., *Macromolecules,* **2002,** *35,* 6245.

[94] Ritzenthaler, S.; Court, F.; Girard-Reydet, E.; Leibler, L.; Pascault, J. P., *Macromolecules,* **2003,** *36,* 118.

[95] van Krevelen, D.W., *Properties of polymers;* Elsevier: Amsterdam, London, New York, Tokyo, 3rd ed.; 1990.

[96] Guinier, A., *Ann. Phys. (Paris),* **1939,** *12,* 161.

[97] Dimitrov, I.; Schlaad, H., *Chem. Commun.,* **2003,** *23,* 2944-2945.

[98] Lutz, J.-F.; Schütt, D.; Kubowicz, S., *Macromol. Rapid Commun.,* **2005,** *26,* 23-28.

[99] Mitchell, J.C.; Woodward, A.E.; Doty, P., *J. Am. Chem. Soc.,* **1957,** *79,* 3955.

[100] Kay, C.; Lorthioir, O.E.; Congreve, P.N.J.M.; McKeown, S.C.; Scicinski, J.J.; Ley, S.V., *Biotechnol. Bioeng.,* **2001,** *71,* 110.

[101] Chittofrati, A.; Boselli, V.; Visca, M.; Friberg, S.E., *J. Disp. Sci. Tech.,* **1994,** *15,* 711-726.

[102] Štěpánek, Petr , In *Dynamic Light Scattering*; Ed.; Brown, Wyn; Oxford Science Publications: Oxford, 1993.

[103] Rinaudo, M.; Domard, A., *J. Am. Chem. Soc.,* **1976,** *98,* 6360-6364.

[104] Kricheldorf, H.R., *Alpha- Aminoacid- N- Carboxy- Anhydrides and Related Heterocycles;* Springer: Heidelberg, 1987.

[105] Singh, B.R. , In *Basic Aspects of the Technique and Application of Infrared Spectroscopy of Peptides and Proteins*; American Chemical Society: Washington, DC, 2000.

[106] Tuzar, Z. , In *Solvents and Self-Organization of Polymers*, Vol. 327, NATO ASI Series ed.; Eds.; Webber, S.E.; P.Munk; Tuzar, Z.; Kluwer Academic Publishers: Dordrecht, 1996.

[107] Heerklotz, H.; Tsamaloukas, A.; Kita-Tokarczyk, K.; Strunz, P.; Gutberlet, T., *J. Am. Chem. Soc.,* **2004,** *126,* 16544-16552.

[108] May, S.; Ben-Shaul, A., *J. Phys. Chem. B,* **2001,** *105,* 630-640.

[109] Paula, S.; Süs, W.; Tuchtenhagen, J.; Blume, A., *J. Phys. Chem.,* **1995,** *99,* 11742-11751.

[110] Clint, J.H.; Walker, T., *J. Chem. Soc., Faraday Trans. 1,* **1975,** *76,* 946-954.

[111] Ropers, M.H.; Czichocki, G.; Brezesinski, G., *J. Phys. Chem. B,* **2003,** *107,* 5281-5288.

[112] Förster, S.; Timmann, A.; Konrad, M.; Schellbach, C.; Meyer, A.; Funari, S.S.; Mulvaney, P.; Knott, R., *J. Phys. Chem. B,* **2005,** *109,* 1347-1360.

[113] García de la Torre, J. , In *Analytical Ultracentrifugation in Biochemistry and Polymer Science*; Eds.; Harding, S.E.; Rowe, A.J.; Horton, J.C.; The Royal Society of Chemistry: Cambridge, 1992.

[114] Eds.; Goddard, E.D.; Ananthapadmanabhan, K.P.;, *Interactions of Surfactants with Polymers and Proteins;* CRC Press: Boca Raton, 1993.

[115] Thünemann, A.F.; General, S., *Langmuir,* **2000,** *16,* 9634-9638.

[116] Thünemann, A.F.; General, S., *J. Controlled Release,* **2000,** *75,* 237-247.

[117] Kozlowski, C. *Synthese und Charakterisierung von neuartigen Blockcopolymeren auf Basis von Poly(alkylenoxiden),* Thesis, TU Berlin, 2003.

[118] Berry, G.C., *J. Chem. Phys.,* **1966,** *44,* 4550.

[119] Mukerjee, P., *Colloids and Surfaces A,* **1994,** *84,* 1-10.